



# **NAVAL POSTGRADUATE SCHOOL**

**MONTEREY, CALIFORNIA**

## **THESIS**

**SURFACE WIND FIELD ANALYSES OF TROPICAL  
CYCLONES DURING TCS-08: RELATIVE IMPACTS OF  
AIRCRAFT AND REMOTELY-SENSED OBSERVATIONS**

by

Patrick J. Havel

September 2009

Thesis Advisor:

Patrick A. Harr

Second Reader:

Russell L. Elsberry

**Approved for public release; distribution is unlimited**

<b>REPORT DOCUMENTATION PAGE</b>			<i>Form Approved OMB No. 0704-0188</i>	
Public reporting burden for this collection of information is estimated to average 1 hour per response, including the time for reviewing instruction, searching existing data sources, gathering and maintaining the data needed, and completing and reviewing the collection of information. Send comments regarding this burden estimate or any other aspect of this collection of information, including suggestions for reducing this burden, to Washington headquarters Services, Directorate for Information Operations and Reports, 1215 Jefferson Davis Highway, Suite 1204, Arlington, VA 22202-4302, and to the Office of Management and Budget, Paperwork Reduction Project (0704-0188) Washington DC 20503.				
<b>1. AGENCY USE ONLY (Leave blank)</b>		<b>2. REPORT DATE</b> September 2009	<b>3. REPORT TYPE AND DATES COVERED</b> Master's Thesis	
<b>4. TITLE AND SUBTITLE</b> Surface Wind Field Analyses of Tropical Cyclones During Tcs-08: Relative Impacts of Aircraft and Remotely-sensed Observations			<b>5. FUNDING NUMBERS</b>	
<b>6. AUTHOR(S)</b> Patrick J. Havel				
<b>7. PERFORMING ORGANIZATION NAME(S) AND ADDRESS(ES)</b> Naval Postgraduate School Monterey, CA 93943-5000			<b>8. PERFORMING ORGANIZATION REPORT NUMBER</b>	
<b>9. SPONSORING /MONITORING AGENCY NAME(S) AND ADDRESS(ES)</b> N/A			<b>10. SPONSORING/MONITORING AGENCY REPORT NUMBER</b>	
<b>11. SUPPLEMENTARY NOTES</b> The views expressed in this thesis are those of the author and do not reflect the official policy or position of the Department of Defense or the U.S. Government.				
<b>12a. DISTRIBUTION / AVAILABILITY STATEMENT</b> Approved for public release, distribution is unlimited			<b>12b. DISTRIBUTION CODE</b>	
<b>13. ABSTRACT (maximum 200 words)</b> The objective of this research is to investigate tropical cyclone wind field structure and development utilizing comprehensive observation sets collected during the Tropical Cyclone Structure 2008 (TCS-08) and The Observing System Research and Predictability Experiment (THORPEX) Pacific Asian Regional Campaign (T-PARC). Rare aircraft measurements in the western North Pacific are utilized to define surface wind distributions of TY Nuri, TY Sinlaku, and STY Jangmi. Stepped Frequency Microwave Radiometer (SFMR) surface winds are compared to Global Positioning System (GPS) dropwindsondes to determine eyewall slope and flight-level reduction factors. The combined SFMR and dropwindsonde wind speed observations are highly correlated ( $r = 0.88$ ) with a RMSE of 2.58 m s <sup>-1</sup> . The three mature storm systems had a combined mean slant reduction factor and relative slope similar to that observed in Atlantic hurricanes. Analysis accuracy was defined by the RMSE between H*Wind analyses and 0-150 m-average dropwindsonde wind speeds. Satellite observations had the largest speed RMSE and the SFMR observations had the smallest speed RMSE. The ECMWF analyses had the largest intensity differences from the JTWC best-track intensity and SFMR-based analyses had the smallest intensity differences from the JTWC best-track intensity.				
<b>14. SUBJECT TERMS</b> Tropical Cyclone, Joint Typhoon Warning Center, Surface Wind Field, THORPEX Asian Regional Campaign, Tropical Cyclone Structure 2008, Western North Pacific Typhoons, H*Wind Analyses			<b>15. NUMBER OF PAGES</b> 99	
			<b>16. PRICE CODE</b>	
<b>17. SECURITY CLASSIFICATION OF REPORT</b> Unclassified	<b>18. SECURITY CLASSIFICATION OF THIS PAGE</b> Unclassified	<b>19. SECURITY CLASSIFICATION OF ABSTRACT</b> Unclassified	<b>20. LIMITATION OF ABSTRACT</b> UU	

THIS PAGE INTENTIONALLY LEFT BLANK

**Approved for public release; distribution is unlimited**

**SURFACE WIND FIELD ANALYSES OF TROPICAL CYCLONES DURING  
TCS-08: RELATIVE IMPACTS OF AIRCRAFT AND REMOTELY-SENSED  
OBSERVATIONS**

Patrick J. Havel  
Lieutenant, United States Navy  
B.S., Virginia Tech, 2000

Submitted in partial fulfillment of the  
requirements for the degree of

**MASTER OF SCIENCE IN METEOROLOGY AND PHYSICAL  
OCEANOGRAPHY**

from the

**NAVAL POSTGRADUATE SCHOOL  
September 2009**

Author: Patrick J. Havel

Approved by: Patrick A. Harr  
Thesis Advisor

Russell L. Elsberry  
Second Reader

Philip A. Durkee  
Chairman, Department of Meteorology

THIS PAGE INTENTIONALLY LEFT BLANK

## ABSTRACT

The objective of this research is to investigate tropical cyclone wind field structure and development utilizing comprehensive observation sets collected during the Tropical Cyclone Structure 2008 (TCS-08) and The Observing System Research and Predictability Experiment (THORPEX) Pacific Asian Regional Campaign (T-PARC). Rare aircraft measurements in the western North Pacific are utilized to define surface wind distributions of TY Nuri, TY Sinlaku, and STY Jangmi. Stepped Frequency Microwave Radiometer (SFMR) surface winds are compared to Global Positioning System (GPS) dropwindsondes to determine eyewall slope and flight-level reduction factors. The combined SFMR and dropwindsonde wind speed observations are highly correlated ( $r = 0.88$ ) with a RMSE of  $2.58 \text{ m s}^{-1}$ . The three mature storm systems had a combined mean slant reduction factor and relative slope similar to that observed in Atlantic hurricanes. Analysis accuracy was defined by the RMSE between H\*Wind analyses and 0-150 m-average dropwindsonde wind speeds. Satellite observations had the largest speed RMSE and the SFMR observations had the smallest speed RMSE. The ECMWF analyses had the largest intensity differences from the JTWC best-track intensity and SFMR-based analyses had the smallest intensity differences from the JTWC best-track intensity.

THIS PAGE INTENTIONALLY LEFT BLANK

## TABLE OF CONTENTS

<b>I.</b>	<b>INTRODUCTION .....</b>	<b>1</b>
<b>A.</b>	<b>MOTIVATION .....</b>	<b>1</b>
<b>B.</b>	<b>WESTERN NORTH PACIFIC TROPICAL CYCLONES.....</b>	<b>3</b>
<b>C.</b>	<b>TCS08/T-PARC .....</b>	<b>4</b>
<b>D.</b>	<b>SYNOPTIC DISCUSSION .....</b>	<b>6</b>
1.	Typhoon Nuri (TCS-15, TY 13W).....	6
2.	Typhoon Sinlaku (TCS-33, TY 15W) .....	9
3.	Super Typhoon Jangmi (TCS-47, STY 19W).....	13
<b>II.</b>	<b>METHODOLOGY .....</b>	<b>17</b>
<b>A.</b>	<b>OBSERVATION SYSTEMS .....</b>	<b>17</b>
1.	In Situ Observations .....	18
2.	Remotely-sensed Observations .....	19
3.	ECMWF Global Model.....	20
<b>B.</b>	<b>H*WIND ANALYSIS SYSTEM.....</b>	<b>20</b>
<b>C.</b>	<b>DATA SUMMARY .....</b>	<b>24</b>
1.	TY Nuri.....	24
2.	TY Sinlaku .....	25
3.	STY Jangmi .....	26
<b>III.</b>	<b>ANALYSIS.....</b>	<b>29</b>
<b>A.</b>	<b>EYEWALL SLOPE .....</b>	<b>29</b>
1.	TY Nuri.....	31
2.	TY Sinlaku .....	34
3.	STY Jangmi .....	44
4.	Summary .....	52
<b>B.</b>	<b>SURFACE WIND FIELD .....</b>	<b>55</b>
1.	Data Distribution and Weighting .....	56
2.	ECMWF and Aircraft .....	62
3.	Aircraft and Satellite .....	65
4.	Summary .....	68
<b>IV.</b>	<b>CONCLUSIONS .....</b>	<b>71</b>
<b>A.</b>	<b>SUMMARY .....</b>	<b>71</b>
<b>B.</b>	<b>RECOMMENDATIONS.....</b>	<b>74</b>
	<b>LIST OF REFERENCES.....</b>	<b>75</b>
	<b>INITIAL DISTRIBUTION LIST .....</b>	<b>77</b>



THIS PAGE INTENTIONALLY LEFT BLANK

## LIST OF FIGURES

Figure 1.	(a) Super Typhoon Jangmi eyewall “Stadium Effect.” Photograph was taken by Beth Sanabia (NPS) onboard WC-130J during second eyewall penetration (0751 UTC 27 Sep 2008). (b) MODIS 1 km visible image of Jangmi on 27 Sep 2008. Courtesy of NASA Earth Observatory Web site.....	1
Figure 2.	Average monthly TCs by intensity. There are significantly more TY strength TCs than any other intensity in the WNP. (From: JTWC 2009a).....	4
Figure 3.	Typhoon Nuri (TY 13W) best-track showing west-northwestward progression and intensification. The JTWC designated Nuri TD 13W on 0000 UTC 16 Aug, upgraded to TS on 1200 UTC 17 Aug, and finally TY on 1200 UTC 18 Aug. (From: JTWC 2009a).....	6
Figure 4.	Infrared satellite imagery of TY Nuri through sequential stages of development. (a) TCS-15 at 0000 UTC 16 Aug, (b) TD 13W at 0000 UTC 17 Aug, (c) TS Nuri at 0000 UTC 18 Aug, and (d) TY Nuri at 0000 UTC 19 Aug. (NRL 2009b).....	7
Figure 5.	The ECMWF surface wind field analyses of TY Nuri through sequential stages of development. (a) TCS-15 at 0000 UTC 16 Aug, (b) TD 13W at 0000 UTC 17 Aug, (c) TS Nuri at 0000 UTC 18 Aug, and (d) TY Nuri at 0000 UTC 19 Aug. ....	8
Figure 6.	Typhoon Sinlaku (TY 15W) best-track showing northward progression, intensification, and northeastward recurvature. The JTWC designated Sinlaku TD 15W on 1200 UTC 7 Sep, upgraded to TS on 1200 UTC 8 Sep, and finally TY on 0600 UTC 9 Sep. (From: JTWC 2009a).....	10
Figure 7.	Infrared satellite imagery of TY Sinlaku through sequential stages of development. (a) TCS-33 at 0000 UTC 7 Sep, (b) TD 15W at 0000 UTC 8 Sep, (c) TS Sinlaku at 0000 UTC 9 Sep, and (d) TY Sinlaku at 0000 UTC 10 Sep. (NRL 2009b).....	11
Figure 8.	The ECMWF surface wind field analyses of TY Sinlaku through sequential stages of development. (a) TCS-33 at 0000 UTC 7 Sep, (b) TD 15W at 0000 UTC 8 Sep, (c) TS Sinlaku at 0000 UTC 9 Sep, and (d) TY Sinlaku at 0000 UTC 10 Sep. ....	12
Figure 9.	Super Typhoon Jangmi (STY 19W) Best-track showing northwestward progression, intensification, and northeastward recurvature. The JTWC designated Jangmi TD 19W at 1200 UTC 23 Sept, upgraded to TS at 0000 UTC 24 Sep, TY at 0600 UTC 25 Sep, and finally STY at 0000 UTC 27 Sep. (From: JTWC 2009a).....	13
Figure 10.	Infrared satellite imagery of STY Jangmi through sequential stages of development. (a) TD 19W at 0000 UTC 23 Sep, (b) TS Jangmi at 0000 UTC 24 Sep, (c) TY Jangmi at 0000 UTC 26 Sep, and (d) STY Jangmi at 0000 UTC 27 Sep. (NRL 2009b). ....	14
Figure 11.	The ECMWF surface wind field analyses of STY Jangmi through sequential stages of development. (a) TD 19W at 0000 UTC 23 Sep, (b)	

	TS Jangmi at 0000 UTC 24 Sep, (c) TY Jangmi at 0000 UTC 26 Sep, and (d) STY Jangmi at 0000 UTC 27 Sep. ....	15
Figure 12.	Typhoon Nuri observation distribution in the H*Wind database from 10 August to 23 August. Time period centers along the top (dd/hh UTC) represent observations of $\pm 12$ -hours. Observations types along the side. Color shading (red to green) represents relative data density. Numerical values indicate the number of observations within the analysis grid.....	21
Figure 13.	Example of an H*Wind analysis for TY Nuri at 1800 UTC 18 Aug. Graphical analysis product on the left. Graphical observation distribution on the right. Example contains observations from ASCAT, Dropwindsonde, METAR, QuickSCAT, SFMR, and ships with a total of 3636 observations. ....	23
Figure 14.	Final observation distribution for Typhoon Nuri in the H*Wind database following the addition of the TCS08/T-PARC SFMR and dropwindsonde data. Time period centers along the top (dd/hh UTC) represent observations of $\pm 12$ -hours. Observations types along the side. Color shading (red to green) represents relative data density. Numerical values indicate the number of observations within the analysis grid. Flight dates and times (dd/hh) for the WC-130J and the NRL P-3 are indicated along the bottom. ....	25
Figure 15.	As in Figure 14, except final observation distribution of Typhoon Sinlaku in the H*Wind database following the addition of TCS08/T-PARC SFMR and dropwindsonde data for all flight times. ....	26
Figure 16.	As in Figure 14, except final observation distribution of STY Jangmi contained within the H*Wind database following the addition of TCS08/T-PARC SFMR and dropwindsonde data for all flight times. ....	27
Figure 17.	TY Nuri WC-130J 0813W flight track (blue), best track (yellow), and 2330 UTC 18 Aug visible imagery (imagery from NRL 2009b). Center penetrations occurred at 2125 UTC 18 Aug for leg 4-1 (SE to NW) and 2319 UTC 18 Aug for leg 4-2 (SW to NE).....	31
Figure 18.	TY Nuri radial plots of winds and rainrates for WC-130J flight 0813W. Center penetrations occurred at 2125 UTC 18 Aug for leg 4-1 (SE to NW) and 2319 UTC 18 Aug for leg 4-2 (SW to NE). Observed SFMR surface winds (red O), flight-level winds (blue X), and rainrate (green triangle) are displayed along the 200 n mi transect. The small amount of missing data is due to aircraft maneuvering. ....	32
Figure 19.	(a) SFMR wind speed ( $\text{m s}^{-1}$ ) versus GPS dropwindsonde wind speed ( $\text{m s}^{-1}$ ) for TY Nuri. The black line indicates SFMR-dropwindsonde best fit ( $\text{SFMR}=2.49+0.89(\text{Drop})$ , $\text{RMSE}=2.26 \text{ m s}^{-1}$ ), and the red-dotted line indicates the neutral fit. (b) Azimuthal distribution of SFMR-drop wind speed differences by storm quadrant relative to the storm heading. Wind speed ( $\text{m s}^{-1}$ ) differences are on the vertical axis, azimuthal variation (deg.) is on the horizontal axis, and the red dots indicate averages over $30^\circ$ azimuthal slices.....	33

Figure 20.	As in Figure 17, except for TY Sinlaku WC-130J 0133W flight track and 0456 UTC 9 Sep enhanced MW imagery. Center penetrations occurred at 0504 UTC 9 Sep for leg 1-1 (S to N) and 0638 UTC 9 Sep for leg 1-2 (W to E). ....	35
Figure 21.	As in Figure 18, except for TY Sinlaku during WC-130J flight 0133W. Center penetrations occurred at 0504 UTC 9 Sep for leg 1-1 (S to N) and 0638 UTC 9 Sep for leg 1-2 (W to E). ....	36
Figure 22.	As in Figure 17, except for TY Sinlaku WC-130J 0233W flight track and 0430 UTC visible imagery. Center penetrations occurred at 0606 UTC 10 Sep for leg 2-1 (SE to NW) and 0753 UTC 10 Sep for leg 2-2 (SW to NE)...	37
Figure 23.	As in Figure 18, except for TY Sinlaku during WC-130J flight 0233W. Center penetrations occurred at 0606 UTC 10 Sep for leg 2-1 (SE to NW) and 0753 UTC 10 Sep for leg 2-2 (SW to NE). ....	38
Figure 24.	As in Figure 17, except for TY Sinlaku WC-130J 0433W flight track and 1134 UTC enhanced MW imagery. Center penetrations occurred at 1207 UTC 11 Sep for leg 3-1 (SE to NW) and 1331 UTC 11 Sep for leg 3-2 (SW to NE). ....	39
Figure 25.	As in Figure 18, except for TY Sinlaku during WC-130J flight 0433W. Center penetrations occurred at 1207 UTC 11 Sep for leg 3-1 (SE to NW) and 1331 UTC 11 Sep for leg 3-2 (SW to NE). ....	40
Figure 26.	As in Figure 17, except for TY Sinlaku WC-130J 0533W flight track and 1737 UTC enhanced MW imagery. Center penetrations occurred at 1646 UTC 12 Sep for leg 4-1 (SE to NW) and 1813 UTC 12 Sep for leg 4-2 (SW to NE). ....	41
Figure 27.	As in Figure 18, except for TY Sinlaku during WC-130J flight 0533W. Center penetrations occurred at 1646 UTC 12 Sep for leg 4-1 (SE to NW) and 1813 UTC 12 Sep for leg 4-2 (SW to NE). ....	42
Figure 28.	As in Figure 19, except for TY Sinlaku SFMR-dropwindsonde wind speed comparisons. The SFMR-dropwindsonde winds best fit curve ( $SFMR=4.89+0.88(Drop)$ with a $RMSE=2.33\text{ m s}^{-1}$ ). ....	43
Figure 29.	As in Figure 17, except for STY Jangmi WC-130J 0247W flight track and 2031 UTC enhanced MW imagery. Center penetrations occurred at 1946 UTC 24 Sep for leg 1-1 (E to W), 2146 UTC 24 Sep for leg 1-2 (SW to NE), and 2353 UTC 24 Sep for leg 1-3 (NW to SE). ....	44
Figure 30.	As in Figure 18, except for STY Jangmi during WC-130J flight 0247W. Center penetrations occurred at 1946 UTC 24 Sep for leg 1-1 (E to W), 2146 UTC 24 Sep for leg 1-2 (SW to NE), and 2353 UTC 24 Sep for leg 1-3 (NW to SE). ....	45
Figure 31.	As in Figure 17, except for STY Jangmi WC-130J 0447W flight track and 2252 UTC enhanced MW imagery. Center penetrations occurred at 2345 UTC 25 Sep for leg 2-1 (SE to NW) and 0113 UTC 26 Sep for leg 2-2 (SW to NE). ....	46
Figure 32.	As in Figure 18, except for STY Jangmi during WC-130J flight 0447W. Center penetrations occurred at 2345 UTC 25 Sep for leg 2-1 (SE to NW) and 0113 UTC 26 Sep for leg 2-2 (SW to NE). ....	47

Figure 33.	As in Figure 17, except for STY Jangmi WC-130J 0747W flight track and 0940 UTC enhanced MW imagery. Center penetrations occurred at 0621 UTC 27 Sep for leg 3-1 (NE to SW), 0755 UTC 27 Sep for leg 3-2 (SE to NW), 0924 UTC 27 Sep for leg 3-3a (SW to NE), and 0944 UTC 27 Sep for leg 3-3b (SW to NE).....	48
Figure 34.	As in Figure 18, except for STY Jangmi during WC-130J flight 0747W. Center penetrations occurred at 0621 UTC 27 Sep for leg 3-1 (NE to SW) and 0755 UTC 27 Sep for leg 3-2 (SE to NW). .....	49
Figure 35.	As in Figure 18, except for STY Jangmi during WC-130J flight 0747W. Center penetrations occurred at 0924 UTC 27 Sep for leg 3-3a (SW to NE), and 0944 UTC 27 Sep for leg 3-3b (SW to NE). .....	50
Figure 36.	As in Figure 19, except for STY Jangmi SFMR-dropwindsonde wind speed comparisons. The SFMR-dropwindsonde best fit curve is (SFMR=0.07+1.08(Drop), RMSE=2.48 m s <sup>-1</sup> ). .....	51
Figure 37.	(a) SFMR-dropwindsonde comparison with the best fit (SFMR=2.58+0.96(Drop), RMSE=2.58 m s <sup>-1</sup> ) defined by the black line. (b) Azimuthal distribution of SFMR-dropwindsonde wind speed differences. (c) Bin-averaged histogram of SFMR-dropwindsonde wind speed differences (mean of 1.7 m s <sup>-1</sup> and standard deviation of 5.9 m s <sup>-1</sup> ).....	53
Figure 38.	(a) Bin-averaged slant reduction factor (Frmx) by storm (STY Jangmi in green, TY Sinlaku in red, TY Nuri in blue). (b) As in (a), except for bin-averaged relative slope of the radius of maximum winds (Rrmx) by storm. (c) Comparison of Frm <sub>x</sub> to Rmx <sub>f</sub> with least-squares fit lines (inbound track in blue, outbound track in red, black represents significant outlier from TS Jangmi leg 1-1). (d) As in (c) except for comparison of Frm <sub>x</sub> to Rrm <sub>x</sub> . .....	54
Figure 39.	(a) H*Wind 8 deg. lat. by 8 deg. lon. wind speed (kt) analysis of SAT (as defined in Table 16 for TY Sinlaku flight three. (b) As in (a) except for TY Sinlaku flight four. (c) H*Wind observation distribution of SAT including QH (magenta), AS (tan), and WS (blue). (d) As in (c), except for flight four for comparison. ....	57
Figure 40.	H*Wind analyzed wind speed (kt) RMSE (blue), direction (deg.) RMSE (green), and wind speed (kt) RMSE to dropwindsondes (red). Observation system categories are located along the x-axis for Sinlaku flight 3, Sinlaku flight 4, and the average of both flights. (a) Satellite weighting chart for SAT, SAT1, ACSAT, and ACSAT1. (b) ECMWF weighting chart for ALLE5, ALLE2, and ALLE1. ....	59
Figure 41.	(a) H*Wind 8 deg. lat. by 8 deg. lon. wind speed (kt) analysis graphical display of the SAT (as defined in Table 16). (b) As in (a) except with central observations removed. (c) As in (a) except with a 150 n mi box removed. (d) H*Wind observation distribution of SAT including QH (magenta), AS (tan), and WS (blue). (e) As in (c) except with central observations flagged (all observation types) for comparison. (f) As in (c) except with a 150 n mi box flagged (all observation types) for comparison...	61

Figure 42.	Wind speed ( $\text{m s}^{-1}$ ) difference field from subtracting the SAT analysis without the center box region (Figure 41 c) from the SAT analysis (Figure 41 a).....	62
Figure 43.	(a) H*Wind 8 deg. lat. by 8 deg. lon. wind speed (kt) analysis display of ECMWF data. (b) As in (a), except AC (as defined in Table 16).....	63
Figure 44.	(a) H*Wind 8 deg. lat. by 8 deg. lon. wind speed (kt) analysis display of ACE1 (as defined in Table 16). (b) As in (a), except with a box surrounding the aircraft observations flagged for comparison. (c) H*Wind observation distribution of ACE1 including EC1 (blue), SF (green), and GP (purple). (d) As in (c), except with a box surrounding the aircraft observations flagged (EC1 data only) for comparison.....	64
Figure 45.	Wind speed ( $\text{m s}^{-1}$ ) difference field from subtracting the ACE1 analyses without the center region (Figure 44 b) from the ACE1 analysis (Figure 44 a). .....	65
Figure 46.	Aircraft and satellite comparison charts for the H*Wind analyses in the AC RMSE (blue), SAT RMSE (red), and ACSAT RMSE (green). Observation system categories are located along the x-axis for Sinlaku flight 3, Sinlaku flight 4, Jangmi flight 2, Jangmi flight 3, and the average of all four flights. (a) Wind speed (kt) RMSE, (b) Wind direction (deg.) RMSE, (c) Wind speed (kt) RMSE to dropwindsondes, and (d) Intensity difference from JTWC best track. ....	66
Figure 47.	Wind speed ( $\text{m s}^{-1}$ ) difference field from subtracting the SAT analysis (Figure 46 a) from the AC analysis (Figure 46 b).....	68
Figure 48.	Summary comparisons of H*Wind analyses of the AC RMSE (blue), SAT RMSE (red), ACSAT RMSE (green), EC RMSE (purple), ALL RMSE (cyan), and ALLE2 RMSE (orange). Observation system categories (defined in Table 16) are displayed along the x-axis for Sinlaku flight 3, Sinlaku flight 4, Jangmi flight 2, Jangmi flight 3, and the average of all four flights. (a) Wind speed (kt) RMSE relative to all of the observations. (b) Wind direction (deg.) RMSE relative to all of the observations. ....	69
Figure 49.	As in Figure 48, except for (a) Wind speed (kt) RMSE relative to the dropwindsondes and (b) Intensity differences from the JTWC best track.....	70

THIS PAGE INTENTIONALLY LEFT BLANK

## LIST OF TABLES

Table 1.	Tropical storm systems selected for this study. Maximum intensity and minimum sea-level pressure (MSLP) estimated by JTWC (JTWC 2009a). TCS dates denote the dates (mm/dd) that T-PARC scientists monitored the system. SFMR coverage denotes the date range (mm/dd) that the T-PARC WC-130J flew for each system. ....	6
Table 2.	Description of observation system parameters. Based on specifications collected from multiple sources (see text). ....	18
Table 3.	Weighting for each observation type. The ECMWF is nominally weighted at 0.25, but is also tested with values of 0.05 and 1.0 for comparison. The ASCAT, QuickSCAT, and Windsat are nominally weighted at 0.25, but are also tested with a value of 1.0 for comparison. ....	22
Table 4.	TY Nuri WC-130J flights. ....	24
Table 5.	TY Sinlaku WC-130J flights. ....	25
Table 6.	STY Jangmi WC-130J flights. ....	27
Table 7.	Eyewall slope terminology used in this study. ....	30
Table 8.	TY Nuri observed and calculated parameters as defined in Table 7 for WC-130J flight 0813W. ....	32
Table 9.	TY Sinlaku observed and calculated parameters as defined in Table 7 for WC-130J flight 0133W. ....	36
Table 10.	TY Sinlaku observed and calculated parameters as defined in Table 7 for WC-130J flight 0233W. ....	38
Table 11.	TY Sinlaku observed and calculated parameters as defined in Table 7 for WC-130J flight 0433W. ....	40
Table 12.	TY Sinlaku observed and calculated parameters as defined in Table 7 for WC-130J flight 0533W. ....	42
Table 13.	STY Jangmi observed and calculated parameters as defined in Table 7 for WC-130J flight 0247W. ....	45
Table 14.	STY Jangmi observed and calculated parameters as defined in Table 7 for WC-130J flight 0447W. ....	47
Table 15.	STY Jangmi observed and calculated parameters as defined in Table 7 for WC-130J flight 0747W. ....	50
Table 16.	Observation system combinations examined in this study. ....	55



THIS PAGE INTENTIONALLY LEFT BLANK

## **LIST OF ACRONYMS AND ABBREVIATIONS**

AOR:	Area of Responsibility
ASCAT:	Advanced Scatterometer
ASOS:	Automated Surface Observing System
CPHC:	Central Pacific Hurricane Center
DoD:	Department of Defense
ECMWF:	European Centre for Medium-range Weather Forecasts
ELDORA:	Electra Doppler Radar
GPS:	Global Positioning System
GTS:	Global Telecommunication System
HRD:	Hurricane Research Division
IR:	Infrared
JTWC:	Joint Typhoon Warning Center
LLCC:	Low-level Circulation Center
MCS:	Mesoscale Convective System
METAR:	Aviation Routine Weather Report
MSLP:	Minimum Sea-Level Pressure
MW:	Microwave Satellite Imagery
NASA:	National Aeronautics and Space Administration
NCAR:	National Center for Atmospheric Research
NHC:	National Hurricane Center
NMFC:	Naval Maritime Forecast Center
NOAA:	National Oceanic and Atmospheric Administration
NRL:	Naval Research Laboratory
NWS:	National Weather Service
QuickSCAT:	Quick Scatterometer
RMSE:	Root Mean Square Error
SFMR:	Stepped Frequency Microwave Radiometer
SST:	Sea Surface Temperature
STY:	Super Typhoon
T-PARC:	THORPEX Pacific Asian Regional Campaigns

TC:	Tropical Cyclone
TCS:	Tropical Circulation System as defined during TCS08/T-PARC
TCS08:	Tropical Cyclone Structure-08
TD:	Tropical Depression
THORPEX:	The Observing System Research and Predictability Experiment
TS:	Tropical Storm
TUTT:	Tropical Upper Tropospheric Trough
TY:	Typhoon
WMO:	World Meteorological Organization
WNP:	Western North Pacific
YOTC:	Year of Tropical Convection

## **ACKNOWLEDGMENTS**

To my wife, BreAnna, thank you for your support and encouragement throughout this endeavor. You performed beautifully (as always) and ensured our family life stayed on track. To my two beautiful daughters, Lorelei and Arwyn, I give thanks and praise for lifting my spirits when times were tough. To my parents, Rich and Judy, I greatly appreciate all the skill-sets you instilled and the loving support throughout my life.

I would like to thank my thesis advisor Professor Patrick Harr for his guidance, wisdom, and technical expertise, Professor Russell Elsberry for his help in editing, and all my other professors here at NPS who not only provided instruction and background material, but also encouraged the best from me.

Finally, to my classmates and friends, I thank you for your support in all aspects of school and social life. Careful balance is truly the key to success.

THIS PAGE INTENTIONALLY LEFT BLANK

# I. INTRODUCTION

## A. MOTIVATION

Tropical cyclones (TC) are immense weather phenomena that impact the global environment, and therefore are of intense scientific interest to operators, forecasters, modelers, and researchers. Military operations occur worldwide, often in remote and harsh environments. Operators and planners require high-tech, reliable, and timely meteorology and oceanography forecasts to ensure mission success. Through strong energy fluxes, momentum transfer and tropospheric mixing, TCs represent one of Mother Nature's preeminent abilities to redistribute mass and energy throughout both the atmospheric and oceanic environment.

The TC environment often represents impressive depth (see Figure 1a) and horizontal scale (Figure 1b). From the human perspective, this means heavy rainfall, intense winds, large sediment transport, flooding, tornado spawns, massive storm surge, and high seas throughout much of the tropical and mid-latitude coastal regions of the world. Increasing understanding and the ability to forecast TC formation, intensification and structure change will enhance tropical risk management (mitigate disastrous consequences) across the globe. Therefore, understanding and properly forecasting TCs is of great interest to the global society.

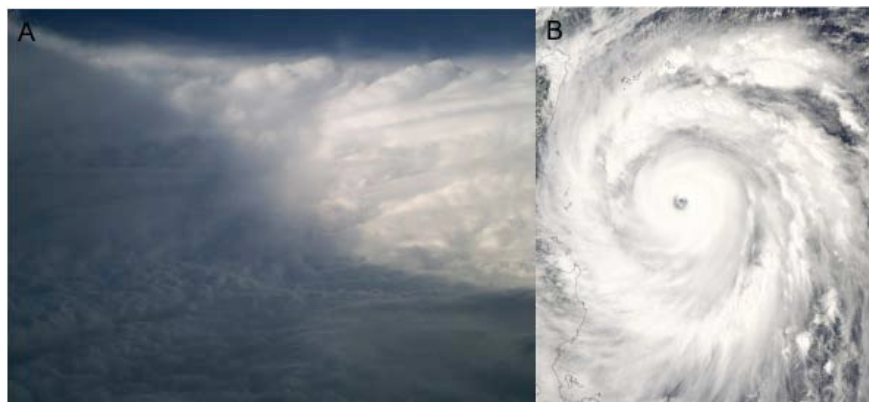


Figure 1. (a) Super Typhoon Jangmi eyewall “Stadium Effect.” Photograph was taken by Beth Sanabia (NPS) onboard WC-130J during second eyewall penetration (0751 UTC 27 Sep 2008). (b) MODIS 1 km visible image of Jangmi on 27 Sep 2008. Courtesy of NASA Earth Observatory Web site.

The National Hurricane Center (NHC) and the Central Pacific Hurricane Center (CPHC) operate within the National Oceanic and Atmospheric Administration (NOAA) to issue TC warnings, advisories, and watches to U.S. assets. The Hurricane Research Division (HRD) supports NHC operations through annual field programs. The mission of the NHC is “to save lives, mitigate property loss, and improve economic efficiency by issuing the best watches, warnings, forecasts, and analyses of hazardous tropical weather, and by increasing the understanding of these hazards” (Brennan et al. 2009). The NHC area of responsibility (AOR) for TC warnings includes the North Atlantic, Gulf of Mexico, and the Caribbean Sea. The CPHC AOR includes the eastern North Pacific (east of 140° W). The Joint Typhoon Warning Center (JTWC) (operating under the command of the Naval Maritime Forecast Center [NMFC]) has a similar mission as NHC. However, JTWC is primarily concerned with DoD assets throughout the Pacific and Indian oceans. Unlike the NHC, there is no operational field program to gather in situ measurements of TCs within the JTWC AOR.

Through this research, a better understanding of the dynamics and processes that define the surface wind fields of a TC will provide improvement in forecast ability. Understanding the value provided to the forecaster by a variety of data sources is the primary objective of this thesis. Through an enhanced understanding of how the surface wind fields develop, strengthen, and mature, forecast model accuracy can be improved in conjunction with providing leadership with more complete risk management criteria. This requires an in-depth understanding of the data-sparse environment throughout TC development from tropical circulation to typhoon.

The focus of this study uses aircraft observations co-located with remotely sensed observations in the western North Pacific (WNP) during the Tropical Cyclone Structure-08 (TCS08) and The Observing System Research and Predictability Experiment (THORPEX) Pacific Asian Regional Campaign (T-PARC) field experiments (late July through early October 2008). The primary analysis method used in this study is the NOAA HRD H\*Wind surface wind analysis system (Powell et al. 1998). The H\*Wind system is used with observations collected during T-PARC/TCS08, JTWC best-track

storm, and satellite data. This is the first time in almost two decades that such a densely collocated observation data set (including satellite, aircraft, and driftsondes) was available for the WNP.

The H\*Wind system is described in Chapter II. The different observation platforms employed with H\*Wind to define the distribution of surface winds in each TC are also described in Chapter II. Results of the incorporation of each data source into the surface wind analysis are presented in Chapter III. In addition, comparisons are made between data types as key representations of the low-level wind field. Acronyms and abbreviations are listed in Appendix A.

## **B. WESTERN NORTH PACIFIC TROPICAL CYCLONES**

Tropical cyclones develop best in areas of low vertical wind shear, low-level cyclonic vorticity, conditional instability, mid-tropospheric moisture, and high sea-surface temperature ( $SST > 26^{\circ}C$ ) (Gray 1979). High oceanic heat content (thermal depth), monsoon depressions, Tropical Upper Tropospheric Trough (TUTT) cells, easterly waves, mesoscale convective systems (MCS), and large oceanic fetch areas in the WNP provide an excellent synoptic environment for TC growth and intensification. Over the WNP, TCs occur during all months (Figure 2). On average, 31 TCs occur per year. The year 2008 was slightly below normal with 27 TCs. The JTWC (per DoD guidance) uses the following nomenclature for intensity in the WNP: Tropical Depression (TD), winds 25-33 kt; Tropical Storm (TS), winds 34-63 kt; Typhoon (TY), winds 64-129 kt; Super Typhoon, (STY) winds  $>130$  kt. On average, the WNP has more TCs of typhoon strength than any other intensity and they most frequently occur during July through September (JTWC 2009a).



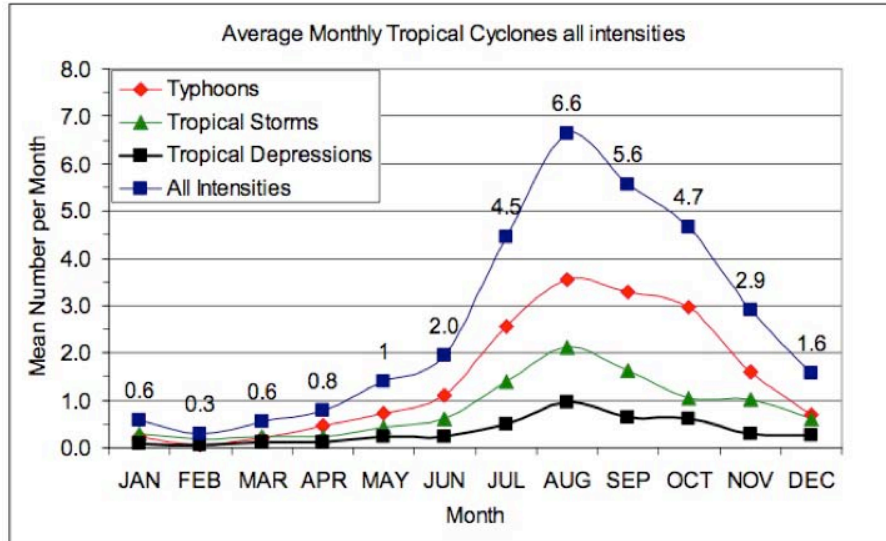


Figure 2. Average monthly TCs by intensity. There are significantly more TY strength TCs than any other intensity in the WNP. (From: JTWC 2009a).

Forecasters rely heavily on numerical models (global and regional), rare in situ observations (ship, buoys, rawindsondes, aircraft), and remotely sensed observations (weather satellites and radar). Due to the relatively data sparse coverage over the remote oceanic regions, weather satellites remain the most effective tropical observation tool for this area. For about two months during 2008, JTWC (and the scientific community) benefited from additional observational coverage (high-resolution satellite assets, aircraft observations, gondola-launched driftsondes, and buoy networks) from the TCS08/T-PARC experiment.

### C. TCS08/T-PARC

THORPEX is a long-term research program under the World Weather Research Program of the World Meteorological Organization (WMO). The THORPEX-Pacific Asian Regional Campaign (T-PARC) and the Tropical Cyclone Structure-08 (TCS08) were joint multi-national field campaigns conducted to improve accuracy of short-range to medium-range tropical cyclone forecasts. The objective of TCS08 and T-PARC were primarily to validate satellite-derived wind measurements, tropical cyclone formation and intensification, and extratropical transition. Participants included scientists from the United States, Australia, England, Japan, Korea, Taiwan, France, Canada, South Korea,

China, and Germany. Aircraft assets included the U.S. Air Force 53<sup>rd</sup> Weather Reconnaissance Squadron WC-130J, Naval Research Laboratory (NRL) P-3, Taiwan DOTSTAR, and the German Aerospace Research Establishment (DLR) Falcon. These aircraft carried a variety of weather instrument packages that included the Stepped Frequency Microwave Radiometer (SFMR) on the WC-130J, Electra Doppler Radar (ELDORA) on the NRL P-3, and Global Positioning System (GPS) dropwindsondes from both aircraft. In addition, large zero-pressure gondolas (Driftsondes) launched from Hawaii drifted downstream and released dropwindsondes at periodic intervals across tropical system generation zones and active storm systems (Elsberry and Harr 2008).

The T-PARC and TCS08 programs were conducted from late July through early October 2008 and provided an extremely rich data set of multiple platform observation/recording systems. From T-PARC and TCS08, eight observation systems were selected for this study: Advanced Scatterometer (ASCAT), Automated Surface Observing System (ASOS), GPS dropwindsonde, Aviation Routine Weather Report (METAR), ship observation, SFMR, QuickSCAT, and WindSat. The HRD H\*Wind surface wind field analysis system was utilized to systematically analyze the observation sets. Comparison of the European Centre for Medium-range Weather Forecasts (ECMWF) global model analyses with the H\*Wind analyses documents the ECMWF's ability to analyze the TCSs and the recorded observation data. The aircraft GPS dropwindsondes, flight-level winds, and WC-130J SFMR surface wind comparisons analyze the three TCs eyewall slope characteristics. Further details on the observation and analysis systems are provided in Chapter II.

During the late summer 2008 typhoon season, T-PARC scientists monitored and tracked multiple tropical circulation systems (TCS) throughout the WNP. Three storms selected for this study are Nuri (TCS-15, TY 13W), Sinlaku (TCS-33, TY 15W), and Jangmi (TCS-47, STY 19W) (Table 1).

Table 1. Tropical storm systems selected for this study. Maximum intensity and minimum sea-level pressure (MSLP) estimated by JTWC (JTWC 2009a). TCS dates denote the dates (mm/dd) that T-PARC scientists monitored the system. SFMR coverage denotes the date range (mm/dd) that the T-PARC WC-130J flew for each system.

<u>System</u>	<u>Name</u>	<u>##</u>	<u>Size</u>	<u>Max Intensity</u>	<u>MSLP</u>	<u>TCS Dates</u>	<u>SFMR Coverage</u>
TCS-15	NURI	13W	TY	100 kt	948 hPa	08/10-08/23	08/15-08/19
TCS-33	SINLAKU	15W	TY	125 kt	929 hPa	09/01-09/22	09/09-09/20
TCS-47	JANGMI	19W	STY	145 kt	914 hPa	09/16-10/02	09/24-09/27

## D. SYNOPTIC DISCUSSION

### 1. Typhoon Nuri (TCS-15, TY 13W)

Typhoon Nuri (TCS-15, TY 13W) was the eighth typhoon in the WNP in 2008 and the first to occur during TCS08. The JTWC designated Nuri TD 13W on 0000 UTC 16 August, upgraded to TS on 1200 UTC 17 August, and finally TY on 1200 UTC 18 August. Nuri made a brief landfall in the northern Philippine Islands at TY strength on 20 August and then made landfall near Hong Kong, China at TS strength on 22 August (final warning by the JTWC) (Figure 3). Nuri had an estimated maximum intensity of 100 kt and minimum sea-level pressure (MSLP) of 948 hPa (Table 1).

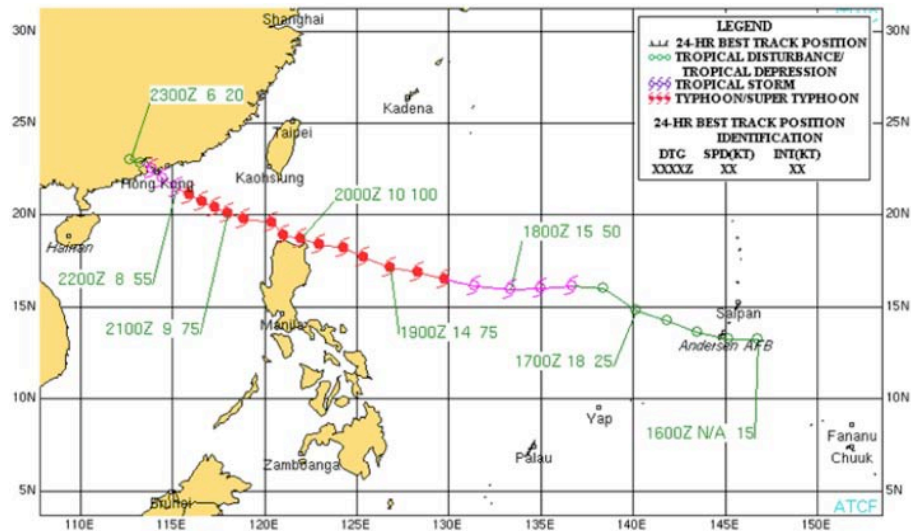


Figure 3. Typhoon Nuri (TY 13W) best-track showing west-northwestward progression and intensification. The JTWC designated Nuri TD 13W on 0000 UTC 16 Aug, upgraded to TS on 1200 UTC 17 Aug, and finally TY on 1200 UTC 18 Aug. (From: JTWC 2009a).

During the period 1700 UTC 15 August through 0325 UTC 18 August Nuri was flown four times by the WC-130J SFMR, the NRL P-3 three times, and a total of 83 dropwindsondes were released. Multiple high-resolution satellite imagery, ship observations, buoy observations, and ASOS observations also were collected during this period. The T-PARC aircraft observation reports and JTWC TC warnings (JTWC 2009b), coupled with the observation datasets, will be used to diagnose the evolution of Nuri. As depicted in the following MTSAT infrared (IR) satellite imagery (Figure 4) and ECMWF (Figure 5) surface wind analyses throughout this observation period, Nuri organized from a broad-scale tropical circulation into a centralized TC and finally intensified into a TY by 1200 UTC 18 August.

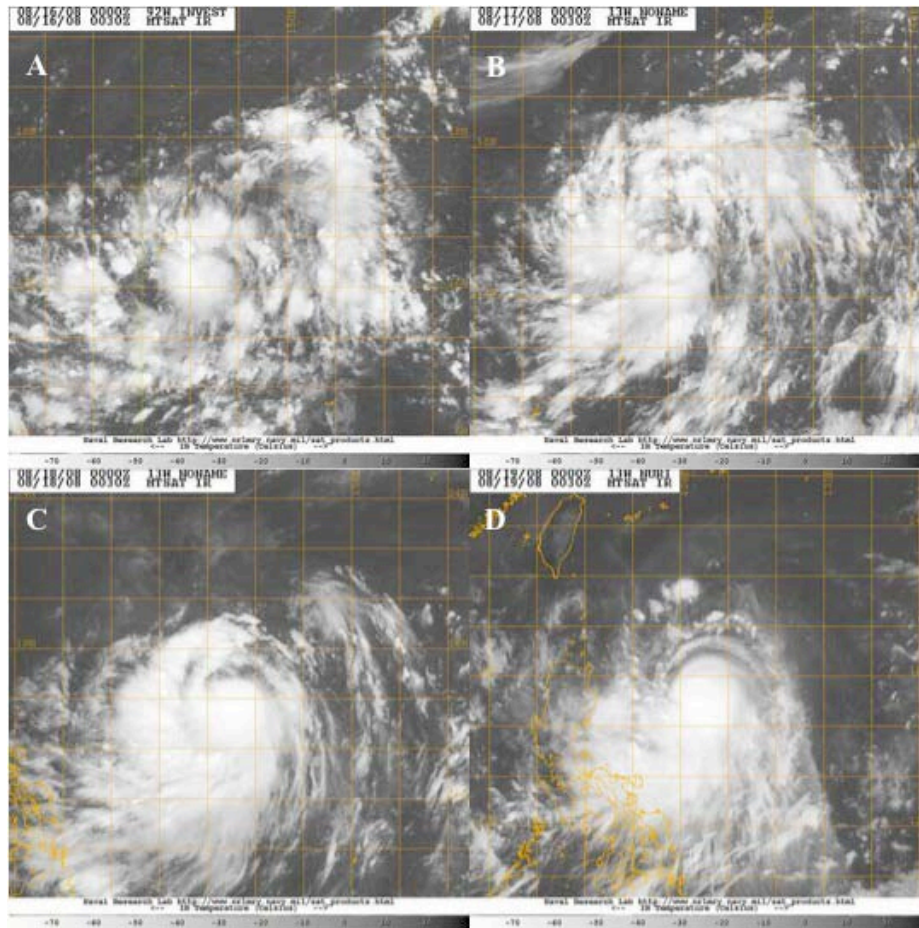


Figure 4. Infrared satellite imagery of TY Nuri through sequential stages of development. (a) TCS-15 at 0000 UTC 16 Aug, (b) TD 13W at 0000 UTC 17 Aug, (c) TS Nuri at 0000 UTC 18 Aug, and (d) TY Nuri at 0000 UTC 19 Aug. (NRL 2009b).



After passing over Guam, TCS-15 evolved from several low-level circulation centers (LLCC) into one broad-scale LLCC and intensified to TD strength by 0000 UTC 16 August. Persistent deep convection that developed into central bands that wrapped around/into the system center are evident in the IR imagery (Figure 4). Low vertical wind shear, moist low and mid levels, and high SST aided development. Under the influence of the semi-permanent WNP high-pressure steering ridge located to the north (Figure 5 a, b), 13W tracked west-northwestward at 15 kt.

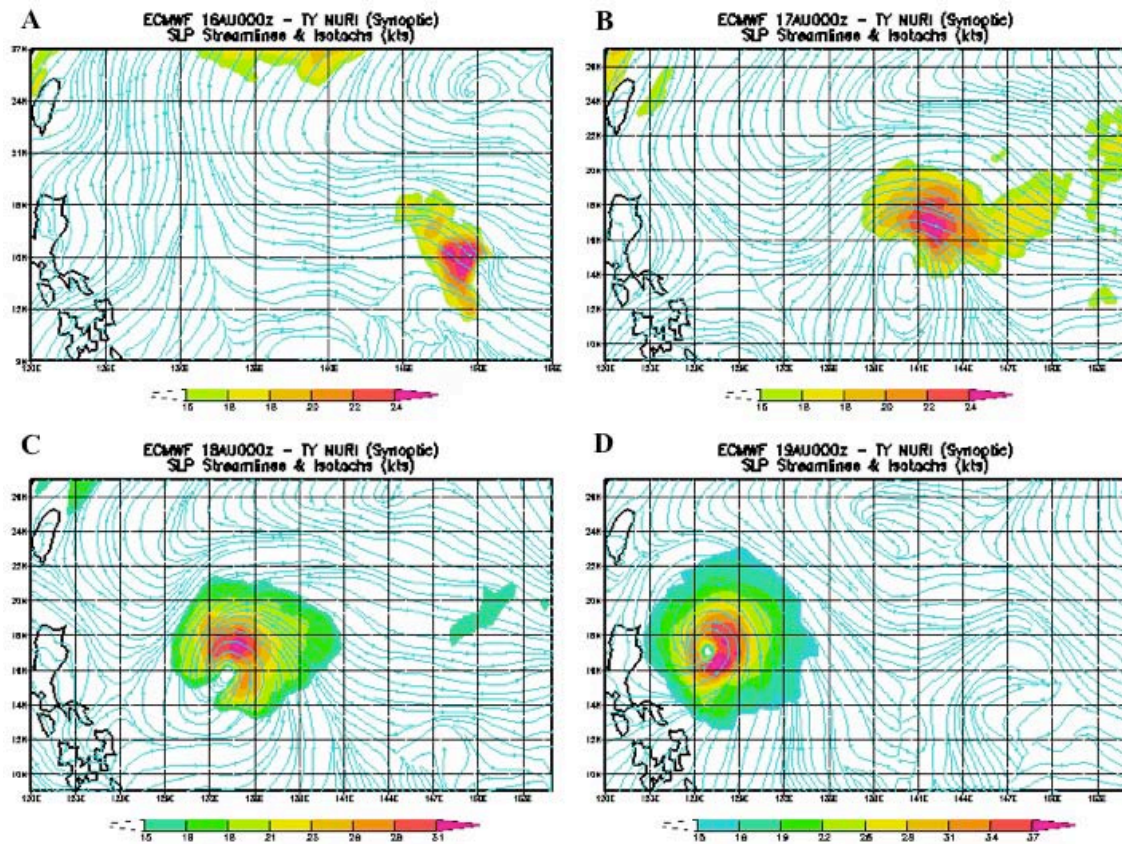


Figure 5. The ECMWF surface wind field analyses of TY Nuri through sequential stages of development. (a) TCS-15 at 0000 UTC 16 Aug, (b) TD 13W at 0000 UTC 17 Aug, (c) TS Nuri at 0000 UTC 18 Aug, and (d) TY Nuri at 0000 UTC 19 Aug.

A strong upper-level anticyclone provided for strong equatorward and weak poleward outflow from TD 13W. The outflow, coupled with relatively low vertical wind shear, enabled the storm to quickly intensify to TS strength by 1200 UTC 17 August and

then rapidly intensify to TY strength 24 hours later by 1200 UTC 18 August. The LLCC organization is clearly identified in IR imagery (Figure 4b) as the convective banding increases. As the strong low-level winds on the northeast side of the storm intensified to 25 kt, the entire system developed winds greater than 15 kt (Figure 5b). The inner core developed maximum surface winds greater than 50 kt based on a WC-130J dropwindsonde observation at 2208 UTC 17 August. The strong surface winds and broad cyclonic extent of the wind field are evident in the ECMWF analysis (Figure 5 c, d). TY Nuri finally developed a visible eye by 0000 UTC 19 August (Figure 4d).

## **2. Typhoon Sinlaku (TCS-33, TY 15W)**

Typhoon Sinlaku (TCS-33, TY 15W) was the ninth typhoon in the WNP during 2008 and the second to occur during TCS08. The JTWC designated Sinlaku TD 15W on 1200 UTC 7 September, upgraded to TS on 1200 UTC 8 September, and finally TY on 0600 UTC 9 September (Figure 6). Sinlaku made brief landfall near Taipei, Taiwan at TY strength on 14 September and then recurved to the northeast. Sinlaku was downgraded to TS on 0000 UTC 15 September and then underwent a re-intensification period while passing over the Kuroshio current and was briefly upgraded to TY on 0000 UTC 19 September, and then downgraded to TS on 1200 UTC 19 September. The final warning was issued by JTWC on 0600 UTC 21 September as Sinlaku transitioned to an extratropical system (Figure 6). Sinlaku had an estimated maximum intensity of 125 kt and MSLP of 929 hPa (Table 1).

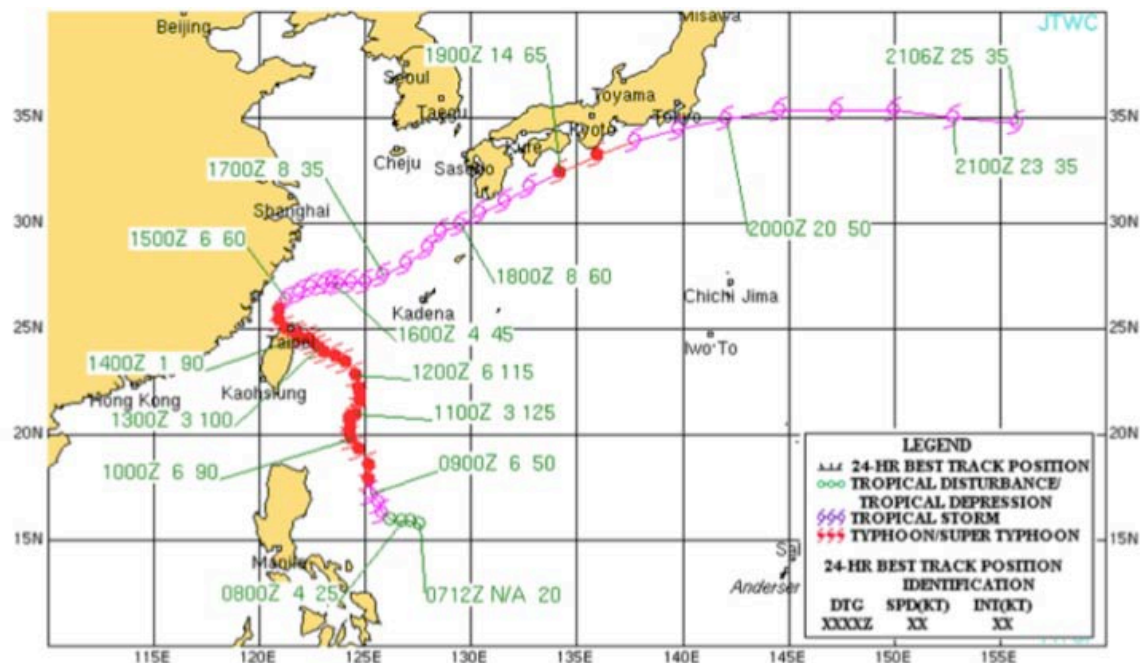


Figure 6. Typhoon Sinlaku (TY 15W) best-track showing northward progression, intensification, and northeastward recurvature. The JTWC designated Sinlaku TD 15W on 1200 UTC 7 Sep, upgraded to TS on 1200 UTC 8 Sep, and finally TY on 0600 UTC 9 Sep. (From: JTWC 2009a).

During the period 0030 UTC 9 September through 1206 UTC 20 September Sinlaku was flown eight times by the WC-130J utilizing SFMR, the NRL P-3 flew five times, and a total of 175 dropwindsondes were released. Multiple high-resolution satellite imagery, ship observations, buoy observations, and ASOS observations were collected during this period. The T-PARC aircraft observation reports and JTWC TC warnings (JTWC 2009b), coupled with the observation datasets, will be used to diagnose the evolution of Sinlaku. As depicted in the following MTSAT IR satellite imagery (Figure 7) and ECMWF (Figure 8) surface wind analyses throughout this observation period, Sinlaku organized from a broad-scale tropical circulation into a centralized TC and finally intensified into a TY by 0600 UTC 9 September (Figure 7c).



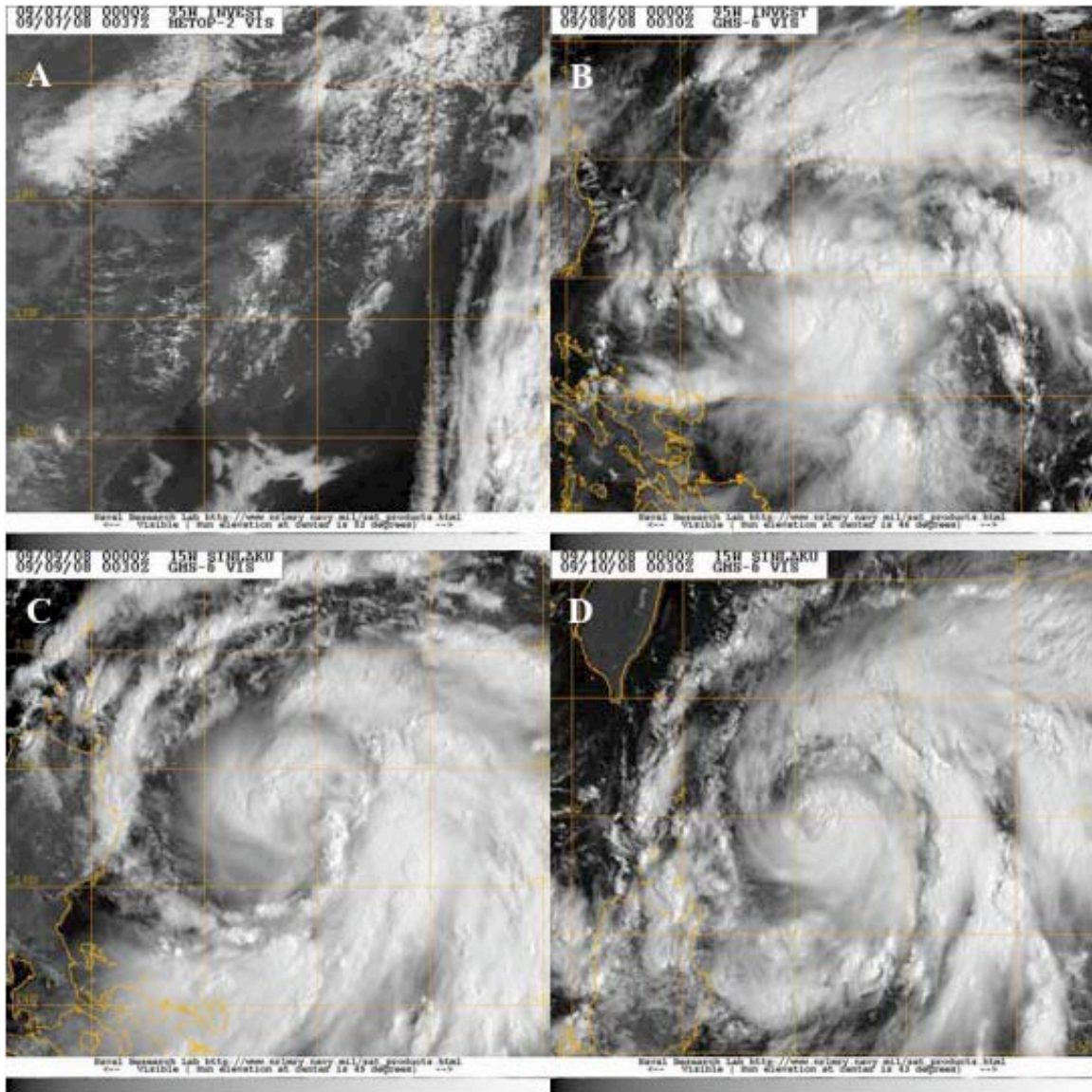


Figure 7. Infrared satellite imagery of TY Sinlaku through sequential stages of development. (a) TCS-33 at 0000 UTC 7 Sep, (b) TD 15W at 0000 UTC 8 Sep, (c) TS Sinlaku at 0000 UTC 9 Sep, and (d) TY Sinlaku at 0000 UTC 10 Sep. (NRL 2009b).



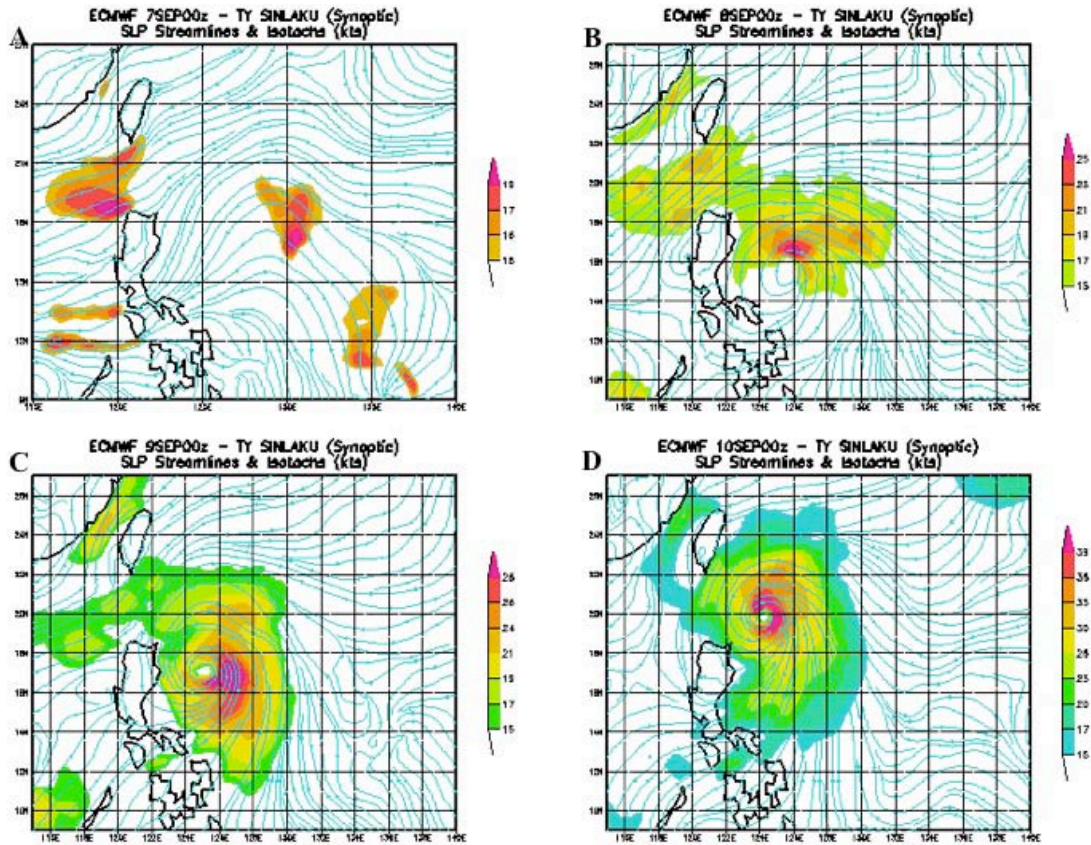


Figure 8. The ECMWF surface wind field analyses of TY Sinlaku through sequential stages of development. (a) TCS-33 at 0000 UTC 7 Sep, (b) TD 15W at 0000 UTC 8 Sep, (c) TS Sinlaku at 0000 UTC 9 Sep, and (d) TY Sinlaku at 0000 UTC 10 Sep.

Typhoon Sinlaku is particularly noteworthy due to two separate rapid intensification events that occurred during its lifecycle. Sinlaku rapidly intensified to TY strength over a two-day period (from 35 kt on 1200 UTC 8 September to 120 kt 1200 UTC 10 September). This rapid intensification occurred over an area of high oceanic heat content and low vertical wind shear. The second intensification from 50 kt on 1200 UTC 18 September to 70 kt on 0600 UTC 19 September occurred as TY 15W produced enhanced upper-level outflow from interaction with a mid-latitude jet. The JTWC noted that the Dvorak satellite interpretations underestimated the intensity of Sinlaku, particularly during the second event and that the WC-130J aircraft reconnaissance was instrumental in determining the intensity of Sinlaku during these events (JTWC 2009a).

### 3. Super Typhoon Jangmi (TCS-47, STY 19W)

Super Typhoon Jangmi (TCS-47, STY 19W) was the second STY in the WNP during 2008 and the first to occur during TCS08. The JTWC designated Jangmi TD 19W on 1200 UTC 23 September, upgraded to TS on 0000 UTC 24 September, TY on 0600 UTC 25 September, and finally STY on 0000 UTC 27 September (Figure 9). Jangmi made brief landfall near Suao, Taiwan as TY strength on 28 September. The final warning issued by JTWC was on 0000 UTC 01 October as Jangmi transitioned to an extratropical system (Figure 9). Jangmi had an estimated maximum intensity of 145 kt and MSLP of 914 hPa (Table 1).

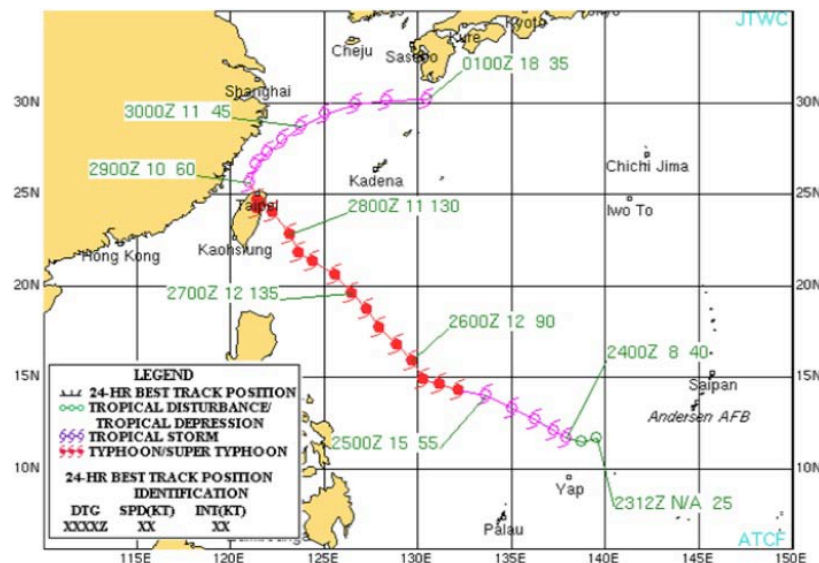


Figure 9. Super Typhoon Jangmi (STY 19W) Best-track showing northwestward progression, intensification, and northeastward recurvature. The JTWC designated Jangmi TD 19W at 1200 UTC 23 Sept, upgraded to TS at 0000 UTC 24 Sep, TY at 0600 UTC 25 Sep, and finally STY at 0000 UTC 27 Sep. (From: JTWC 2009a).

During the period 1713 UTC 24 September through 1417 UTC 27 September Jangmi was flown three times by the WC-130J utilizing SFMR, flown by the NRL P-3 three times, and a total of 89 dropwindsondes were released from both aircraft. Multiple high-resolution satellite imagery, ship observations, buoy observations, and ASOS observations were collected during this period. The T-PARC aircraft observation reports and JTWC TC warnings (JTWC 2009b), coupled with the observation datasets, will be

used to diagnose the evolution of Jangmi. As depicted in the following MTSAT IR satellite imagery (Figure 10) and ECMWF (Figure 11) surface wind analysis throughout this observation period, Jangmi organized from a broad-scale tropical circulation into a centralized TC and finally intensified into a STY by 0000 UTC 27 September (Figure 10d).

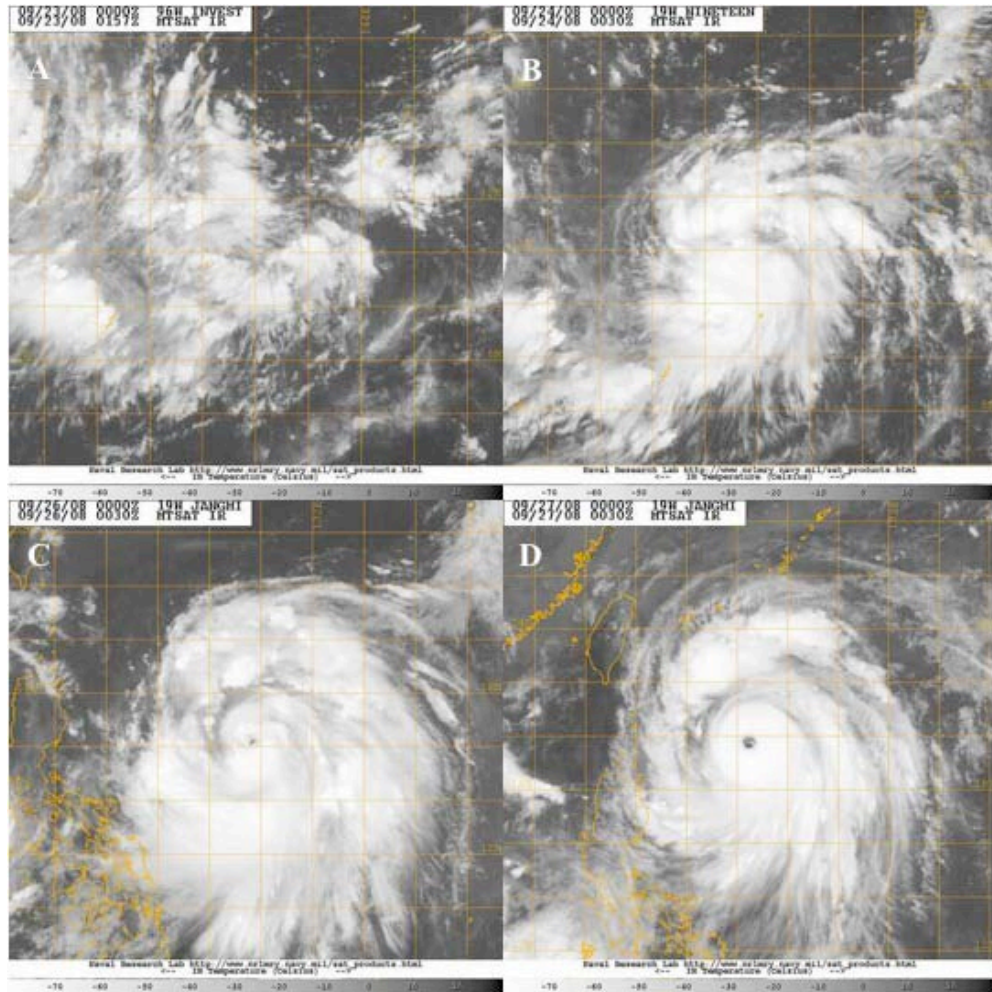


Figure 10. Infrared satellite imagery of STY Jangmi through sequential stages of development. (a) TD 19W at 0000 UTC 23 Sep, (b) TS Jangmi at 0000 UTC 24 Sep, (c) TY Jangmi at 0000 UTC 26 Sep, and (d) STY Jangmi at 0000 UTC 27 Sep. (NRL 2009b).



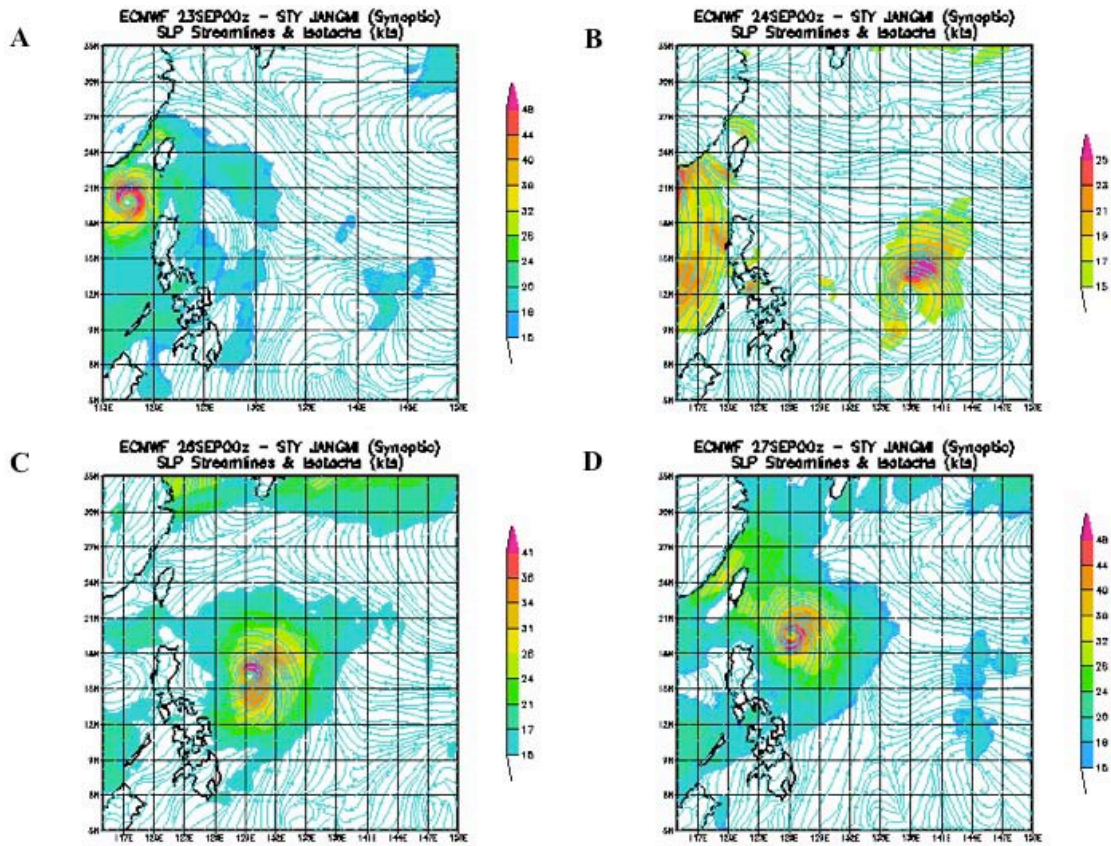


Figure 11. The ECMWF surface wind field analyses of STY Jangmi through sequential stages of development. (a) TD 19W at 0000 UTC 23 Sep, (b) TS Jangmi at 0000 UTC 24 Sep, (c) TY Jangmi at 0000 UTC 26 Sep, and (d) STY Jangmi at 0000 UTC 27 Sep.

THIS PAGE INTENTIONALLY LEFT BLANK

## **II. METHODOLOGY**

### **A. OBSERVATION SYSTEMS**

Understanding the value provided to the forecaster by a variety of data sources is the primary objective of this thesis. Forecasters rely heavily on numerical models, rare insitu observations, and remotely sensed observations. Due to the relatively data sparse coverage over the remote oceanic regions, weather satellites remain the most effective observational tool for this area. The focus of this study is on aircraft observations co-located with remotely sensed observations in the western WNP during the TCS08/T-PARC field experiments. This is the first time in almost two decades that such a densely co-located observation data set was available for the WNP.

During the late summer 2008 typhoon season, T-PARC scientists monitored and tracked multiple TCSs throughout the WNP. Three storms selected for this study are Nuri, Sinlaku, and Jangmi (Table 1). Eight TCS08/T-PARC observation systems are selected for this study: ASCAT, ASOS, GPS dropwindsonde (onboard WC-130J and NRL P-3), METAR, ship observation, SFMR (onboard WC-130J), QuickSCAT, and WindSat (Table 2). The H\*Wind surface wind field analysis system is utilized to analyze the observation sets. Analyzed data fields from ECMWF are also utilized in the study of this surface wind field analysis.

Table 2. Description of observation system parameters. Based on specifications collected from multiple sources (see text).

<b><u>Sensor System</u></b>	<b><u>Platform</u></b>	<b><u>Resolution</u></b>	<b><u>Coverage</u></b>	<b><u>Accuracy</u></b>
ASCAT	MetOp Satellite	50 km	Two parallel 550 km swaths	Reliable <30 kt
ASOS	Land based	Single Point	Single Point	$\pm 2$ kt, $\pm 5$ deg.
Dropwindsonde	WC-130J & NRL P-3	5 m	30,000 ft to Surface	$\pm 4$ kt
METAR	Land based	Single Point	Single Point	N/A
Ship Observation	Shipboard	Single Point	Single Point	N/A
SFMR	WC-130J	Linear Points	AC Flight Path	$\sim 2\%$ at 58 kt
QuickSCAT	Seawinds onboard QuickSCAT	12.5 km	1800 km	Reliable < 90 kt
WindSat	NRL Satellite	25 km	1000 km & 400 km swaths	$\pm 2$ kt & 20 deg. (reliable <25 kt)

## 1. In Situ Observations

Observations collected in situ include the National Weather Service (NWS) ASOS (NWS 2009), National Center for Atmospheric Research (NCAR) Global GPS dropwindsonde (onboard WC-130J and NRL P-3), METAR, NOAA HRD SFMR, and ship observations. ASOS, METAR, and ship observations were placed within the HRD H\*Wind database (HRD 2009a). Dropwindsonde and SFMR data were collected onboard the T-PARC aircraft and transmitted in real-time via the Global Telecommunication System (GTS). The aircraft data used in this study underwent post-processing following the conclusion of the field program and were then re-formatted for ingestion into the H\*Wind program.

The WC-130J and NRL P-3 flew a total of 26 flights in Nuri, Sinlaku, and Jangmi and released approximately 350 dropwindsondes. The WC-130J typically flew at altitudes of 30,000 ft for pre-tropical cyclone systems and 10,000 ft during operations in mature TCs. The P-3 typically flew at 12,000 ft to optimize ELDORA coverage, but also flew at 24,000 ft to enhance dropwindsonde vertical profiles when needed. The dropwindsondes averaged 100 km horizontal spacing (except for several rapid succession

deployments near the tropical circulation centers). The NCAR GPS dropwindsonde has wind accuracies of  $0.5 - 2.0 \text{ m s}^{-1}$  and vertical resolution of  $\sim 5 \text{ m}$  (Hock and Franklin 1999).

The SFMR onboard the WC-130J collects surface wind measurements along the flight paths. The SFMR has regularly measured the surface wind fields of Atlantic TCs since Hurricane Allen (1980). Regular aircraft reconnaissance in the WNP has not been conducted since 1987. During TCS08/T-PARC, the WC-130J flew radial paths through the center of multiple tropical circulations to measure the radial distribution of maximum surface winds throughout the TC intensification cycle. The SFMR reliably measures the surface wind field along the radial paths to an accuracy of  $\pm 2\%$  at 53 kt, (Uhlhorn et al. 2007; HRD 2009b). A total of 15 WC-130J flights occurred during Nuri, Sinlaku, and Jangmi to study structure change. The first two flights of Nuri were at 30,000 ft. Although SFMR data were collected for 30,000 ft altitudes, they were not used in the H\*Wind analysis because of the uncertainty in ascertaining a wind direction from an altitude of 30,000 ft.

## **2. Remotely-sensed Observations**

Remotely sensed observations include the European Space Agency ASCAT, U.S. National Aeronautics and Space Administration (NASA) QuickSCAT, and the U.S. Navy WindSat. The ASCAT, QuickSCAT, and WindSat data are routinely collected in the HRD H\*Wind database (HRD 2009a).

The primary satellite-based tool for identifying the surface wind distribution for tropical systems is QuickSCAT (Brennan et al. 2009). Although ASCAT and WindSAT are available, they do not have the resolution, swath width, or intensity range of QuickSCAT. The resolution of ASCAT used in this study is 50 km within two parallel swath widths of 550 km, and these winds are considered to be reliable to 25 kt (ESA 2009). The resolution of WindSat is 25 km within two swath widths of 1000 km and 400 km, and considered to be reliable to 30 kt (NRL 2009a). The resolution of QuickSCAT used in this study is 12.5 km with a single swath width of 1800 km, and considered to be reliable to 90 kt (Brennan et al. 2009). Thus, both ASCAT and WindSat are unreliable



forecasting tools for tropical systems of at least TS strength ( $>34$  kt), and all three have limitations due to rain and cloud liquid water (Brennan et al. 2009). However, due to the relatively data sparse coverage over the remote oceanic regions, weather satellites remain the most effective observation tool for this area.

### **3. ECMWF Global Model**

Global surface wind analyses from the ECMWF are used in surface wind field comparisons. Over 12-hour periods, the ECMWF assimilates a global set of wind, temperature, surface pressure, humidity, and ozone observations using a four-dimensional multivariate variational assimilation (ECMWF 2009). The observations assimilated include in-situ observations and satellite data. The ECMWF surface wind analysis is archived on a  $\frac{1}{4}$  degree latitude/longitude resolution grid. Six-hourly (0000, 0600, 1200, 1800 UTC) analyses utilize a background field from a triangular truncation (T799) numerical model that has a semi-Lagrangian, two-time-level, semi-implicit formulation (ECMWF 2009). These fields were made available from the ECMWF via the Year of Tropical Convection (YOTC) archive and then re-formatted for ingestion into the H\*Wind program. These ECMWF analyses are used primarily as a base-line for analysis comparisons in the H\*Wind. However, the analysis fields are also used as background fields for analyses containing aircraft and satellite data sources.

### **B. H\*WIND ANALYSIS SYSTEM**

The primary analysis method used in this study is the NOAA HRD H\*Wind surface wind analysis system (Powell et al. 1998). The HRD has developed various versions of the H\*Wind system since 1996. The H\*Wind program is a user interface-based analysis program that blends multiple observation sets and gridded fields together through a user-defined time period along the best-track of a TC. An analysis is then computed by H\*Wind to provide graphical and gridded analysis products for both operational and research uses. The H\*Wind program is particularly useful for understanding the size and strength distribution of the surface wind field to assesses TC intensity (Powell et al. 1998).

The H\*Wind program is used to systematically analyze observations collected during T-PARC/TCS08, JTWC best-track storm, and satellite data (Table 2). The ASCAT, ASOS, METAR, ship observations, QuickSCAT, and WindSat data were retrieved from the HRD H\*Wind database (HRD 2009a). After an example of the H\*Wind database observation distribution throughout the lifecycle of TY Nuri (Figure 12), this database was augmented by the GPS dropwindsonde and SFMR data collected during TCS08/T-PARC, NRL high-resolution ASCAT, and the ECMWF fields. All data are collected, quality controlled, and processed to conform to a 10 m height field, exposure (marine or land influenced), and averaging period (1 minute sustained) (Powell et al. 1998).

AUG:	10/00	11/00	12/00	13/00	14/00	15/00	16/00	17/00	18/00	19/00	20/00	21/00	22/00	23/00	Total
AFRC	0	0	0	0	0	0	0	0	19	0	0	0	0	0	19
ASCAT	0	0	0	0	0	0	33	1060	1054	1065	1273	530	1250	196	6461
ASOS	0	0	0	0	0	0	24	31	0	0	0	0	0	0	55
DRIFTING_BUOY	0	10	1	385	244	220	3	1	85	50	31	34	0	33	1097
METAR	0	53	0	0	0	0	48	68	0	9	88	220	93	0	579
MOORED_BUOY	0	0	0	0	0	0	47	47	0	0	0	0	0	0	94
QSCAT	0	0	0	0	0	0	282	1221	3372	640	2839	811	1012	445	10622
QSCAT_HIRES	0	0	0	0	0	0	1155	5569	13584	3260	11563	3700	5396	2012	46239
QSCAT_RAIN	0	0	0	0	0	0	28	444	1678	636	1432	212	1394	330	6154
QSCAT_RAIN_HIRES	0	0	0	0	0	0	102	1077	5072	1890	3833	384	3673	872	16903
SFMR_AFRC	0	0	0	0	0	0	0	0	20	0	0	0	0	0	20
SHIP	0	3	1	5	5	3	1	2	10	22	18	37	41	16	164
WINDSAT	0	0	0	0	0	0	631	2426	0	0	1271	2819	3769	0	10916
WINDSAT_RAIN	0	0	0	0	0	0	165	1162	0	0	947	2033	1184	0	5491
Total	0	66	2	390	249	223	2519	13108	24894	7572	23295	10780	17812	3904	104814

Figure 12. Typhoon Nuri observation distribution in the H\*Wind database from 10 August to 23 August. Time period centers along the top (dd/hh UTC) represent observations of  $\pm 12$ -hours. Observations types along the side. Color shading (red to green) represents relative data density. Numerical values indicate the number of observations within the analysis grid.

The H\*Wind program weights each observation type (Table 3) based on prior research studies (HRD 2009a). Imported gridded fields are normally weighted at 0.05 in H\*Wind. However, since the ECMWF is an advanced analysis, it was specified in this study to have a weighting of 0.25 to coincide with QuickSCAT, ASCAT, and WindSat weight values. In the selected test analyses of specific time periods, ECMWF fields are weighted with values of 0.05, 0.25, and 1.0 to examine the sensitivity of the H\*Wind analysis to the background field. In the selected test analyses of specific time periods,

ASCAT, QuickSCAT, and Windsat fields are weighted with values of 0.25 and 1.0 to examine the sensitivity of the H\*Wind analysis of satellite-derived observations to the aircraft in situ observations.

Table 3. Weighting for each observation type. The ECMWF is nominally weighted at 0.25, but is also tested with values of 0.05 and 1.0 for comparison. The ASCAT, QuickSCAT, and Windsat are nominally weighted at 0.25, but are also tested with a value of 1.0 for comparison.

<u>System</u>	<u>H*Wind Weight</u>	<u>System</u>	<u>H*Wind Weight</u>
ASCAT	0.25, 1.00	SFMR_AFRC	1.00
ASOS	0.80	SHIP	0.40
GPSSONDE_WL150	1.00	WINDSAT	0.25, 1.00
METAR	0.70	ECMWF	0.05, 0.25, 1.00
QSCAT_HIRES	0.25, 1.00		

The primary analysis output is a graphic representation (Figure 13) of the surface isotachs and wind barbs within an 8° grid centered on the TC best-track position. This graphical product contains information about the analyzed observation sets, observed maximum surface wind (speed (kt) and location from center), and analyzed maximum surface wind (speed (kt) and location from center). Furthermore, the mean speed error (kt), mean direction error (deg.), root mean square (RMS) speed error (kt), and RMS direction error (deg.) are calculated from differences between analyzed values and all observations. In addition, the H\*Wind analysis is provided in gridded form for ingestion into grid display tools for statistical comparison.

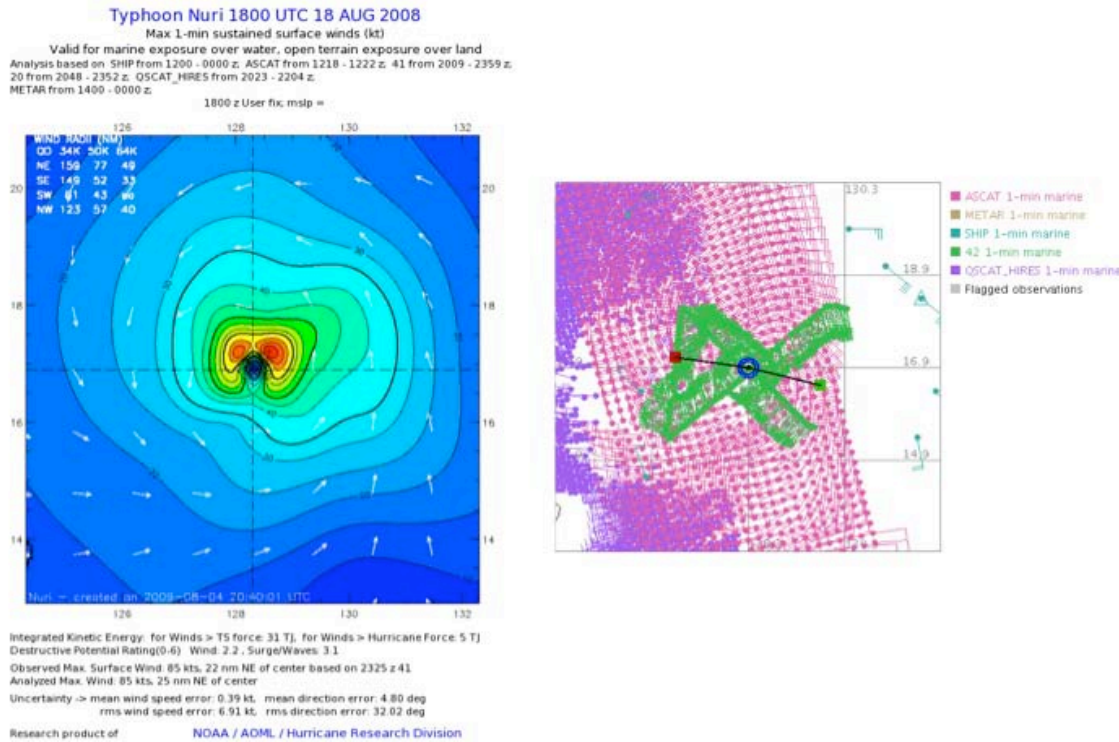


Figure 13. Example of an H\*Wind analysis for TY Nuri at 1800 UTC 18 Aug. Graphical analysis product on the left. Graphical observation distribution on the right. Example contains observations from ASCAT, Dropwindsonde, METAR, QuickSCAT, SFMR, and ships with a total of 3636 observations.

For each of the three storm systems selected, a storm-relative H\*Wind analysis was systematically computed, utilizing data available within  $\pm 6$ -hour window (time and space centered on the TC best-track position) for each WC-130J flight. This ensured maximum data variety and coverage for all flight legs. All defaults within H\*Wind were utilized for comparison purposes. Each analysis time-period utilized the observation sets with and without the inclusion of the ECMWF analysis. Based on interesting periods during each storm system, several specific time-periods were selected for more detailed analysis. These specified time-periods utilized analysis of individual observation data sets with and without ECMWF analyses and systematically varying weighting functions. Statistical results and the gridded fields provided by the H\*Wind analyses were collected and are analyzed and compared with ECMWF analyses in Chapter III.

## C. DATA SUMMARY

### 1. TY Nuri

During the period 1700 UTC 15 August through 0325 UTC 18 August the WC-130J flew four times (Table 4) into Nuri. During the first two flights, the WC-130J flew at 30,000 ft and therefore SFMR data are not used. The NRL P-3 flew into Nuri three times, and a total of 83 dropwindsondes were released from both aircraft.

Table 4. TY Nuri WC-130J flights.

<u>Flight</u>	<u>Mission Start</u>	<u>Mission End</u>	<u>Radial Legs</u>	<u>Dropwindsondes</u>	<u>Pattern</u>
0313W	08/15 1700	08/15 2100	0	20	Square Spiral
0413W	08/16 1945	08/17 0415	1	30	Spiral/Alpha
0613W	08/17 1647	08/17 2321	3	9	Butterfly (<25% complete)
0813W	08/18 1804	08/19 0325	2	24	Alpha/Butterfly

A “square/spiral” pattern (flight 0313W) was flown on 15 August to map the formation period of TCS-15 (pre-Nuri). As the LLCC developed, a “spiral/alpha” pattern (flight 0413W) was then flown on 16-17. When Nuri became a TC, a “butterfly” pattern (flight 0613W) was flown on 17 August to map the structure features of TD 13W. The WC-130J mission was shortened due to aircraft mechanical problems, so only partial coverage is available from this mission. An “alpha/butterfly” pattern (flight 0813W) was flown on 18-19 August to map the structural features and to coincide with satellite (IR and microwave) overpasses of TY 13W. Multiple high-resolution satellite imagery, ship observations, METAR, and ASOS observations occurred during this period (Figure 14).

	AUG:	15/18	16/00	16/06	16/12	16/18	17/00	17/06	17/12	17/18	18/00	18/06	18/12	18/18	19/00	Total
ASCAT		218	0	33	33	1052	808	0	841	841	875	875	430	430	741	7177
ASOS		18	12	12	17	19	14	0	0	0	0	0	0	0	0	92
GPS SONDE WL150		5	20	5	0	15	35	21	0	12	22	10	0	21	22	188
METAR		40	33	29	21	22	37	0	0	0	0	0	0	13	13	208
QSCAT HIRES		1283	399	1781	2562	2480	3809	2319	3971	7915	7163	5806	4758	2053	2332	48631
SFMR AFRC		0	0	0	0	0	0	0	0	386	443	0	0	438	500	1767
SHIP		4	0	1	1	1	0	2	1	3	8	12	11	13	14	71
WINDSAT		1990	631	0	0	3700	2426	0	0	0	0	0	0	0	0	8747
Total		3558	1095	1861	2634	7289	7129	2342	4813	9157	8511	6703	5199	2968	3622	66881
WC-130J		15/18-15/21				16/19-17/04			17/16-17/23					18/18-19/03		
NRL P3		15/22-16/04				16/22-17/03			17/21-18/05							

Figure 14. Final observation distribution for Typhoon Nuri in the H\*Wind database following the addition of the TCS08/T-PARC SFMR and dropwindsonde data. Time period centers along the top (dd/hh UTC) represent observations of  $\pm 12$ -hours. Observations types along the side. Color shading (red to green) represents relative data density. Numerical values indicate the number of observations within the analysis grid. Flight dates and times (dd/hh) for the WC-130J and the NRL P-3 are indicated along the bottom.

## 2. TY Sinlaku

During the period 0030 UTC 9 September through 1206 UTC 20 September, the WC-130J flew Sinlaku eight times (Table 5). The NRL P-3 flew into Sinlaku five times, and both aircraft released a total of 175 dropwindsondes.

Table 5. TY Sinlaku WC-130J flights.

<u>Flight</u>	<u>Mission Start</u>	<u>Mission End</u>	<u>Radial Legs</u>	<u>Dropwindsondes</u>	<u>Pattern</u>
0133W	09/09 0030	09/09 1045	2	20	Alpha
0233W	09/10 0140	09/10 1225	2	24	Alpha
0433W	09/11 0728	09/11 1828	2	25	Alpha
0533W	09/12 1138	09/12 2318	2	21	Alpha
0833W	09/16 2044	09/17 0426	0	7	Synoptic
1033W	09/17 2224	09/18 0713	3	32	Butterfly
1233W	09/19 0053	09/10 0711	0	18	Synoptic
1333W	09/20 0156	09/20 1206	2	28	Synoptic

The WC-130J “alpha” pattern flights on 9 and 10 September were designed to map the structural features of the developing TS 15W. During flight 0233W, the center was flown through twice in two hours. Based on two dropwindsondes, the MSLP dropped 8 hPa in two hours (0605 UTC value of 954 hPa and 0753 UTC value of 946



hPa). An “alpha” pattern (flight 0433W) was then flown again on 11 September. During this flight, aircraft radar data showed concentric eyewalls at a radius of 8 n mi and 45 n mi. An “alpha” pattern (flight 0533W) was flown on 12 September to map the eyewall structure features of TY 15W after the eyewall replacement cycle of the previous day. A “synoptic” pattern (flight 0833W) was flown on 16/17 September to map the extratropical transition features of TS 15W and the oceanic and atmospheric synoptic pattern ahead of the storm. A “butterfly” pattern (flight 1033W) was flown on 17/18 September to map the extratropical transition and structure features of TS 15W (aircraft reconnaissance data collected on this flight resulted in the JTWC upgrading Sinlaku to a TY). A “synoptic” pattern (flight 1233W) was flown on 19 September to map the extratropical transition features of TY 15W. A “synoptic” pattern (flight 1333W) was flown on 20 September to map the extratropical transition features of TS 15W. Multiple high-resolution satellite imagery, ship observations, METAR, and ASOS observations were collected during this period (Figure 15).

SEP:	09/00	09/06	09/12	09/18	10/00	10/06	10/12	10/18	11/00	11/06	11/12	11/18	12/00	12/06	12/12	12/18	Total
ASCAT	503	521	0	0	716	716	48	48	339	339	773	773	782	777	240	240	6815
ASOS	0	0	0	0	0	0	0	0	0	0	0	0	0	0	0	0	0
GPSSONDE_WL150	10	17	7	0	4	21	17	0	10	12	15	11	0	0	10	14	148
METAR	62	67	53	55	115	132	98	61	144	178	0	118	165	233	190	173	1844
QSCAT_HIRES	4014	3777	3887	2201	2199	1861	1833	0	2283	1843	1929	5201	5287	4359	4396	4210	49280
SFMR_AIRC	331	555	227	0	164	539	378	0	0	204	535	330	0	0	299	465	4027
SHIP	20	22	23	22	24	19	15	8	9	11	12	15	17	18	16	14	265
WINDSAT	0	3137	3189	0	0	1656	1670	0	2117	489	510	0	0	0	0	1355	14123
Total	4940	8096	7386	2278	3222	4944	4059	117	4902	3076	3774	6448	6251	5387	5151	6471	76502
WC-130J	09/00-09/10			10/01-10/12				11/07-11/18					12/11-12/23				
NRL P3								10/20-11/06									

Figure 15. As in Figure 14, except final observation distribution of Typhoon Sinlaku in the H\*Wind database following the addition of TCS08/T-PARC SFMR and dropwindsonde data for all flight times.

### 3. STY Jangmi

During the period 1713 UTC 24 September through 1417 UTC 27 September, the WC-130J flew into Jangmi three times (Table 6). The NRL P-3 flew three times into Jangmi, and a total of 89 dropwindsondes were released from both aircraft.

Table 6. STY Jangmi WC-130J flights.

<u>Flight</u>	<u>Mission Start</u>	<u>Mission End</u>	<u>Radial Legs</u>	<u>Dropwindsondes</u>	<u>Pattern</u>
0247W	09/24 1713	09/25 0320	3	26	Alpha/Butterfly
0447W	09/25 2003	09/26 0650	2	24	Figure 4 Alpha
0747W	09/27 0208	09/27 1417	3	39	Alpha/Butterfly

An “alpha/butterfly” pattern (flight 0247W) was flown on 24-25 September to map the structure and intensity change features of TS 19W as it intensified to TY strength. A “figure 4 alpha” pattern (flight 0447W) was flown on 25-26 September to map the structure and intensity change features of TY 19W undergoing further typhoon development. An “alpha/butterfly” pattern (flight 0747W) was flown on 27 September to map the structure and intensity change features of STY 19W. During this flight, the aircraft mission scientist noted a 25 n mi radius eye with multiple mesovortices rotating around the eye (see Figure 1b). This flight was the first aircraft reconnaissance penetration of a STY (WNP) in nearly 30 years. Multiple high-resolution satellite imagery, ship observations, METAR, and ASOS observations were collected during this period (Figure 16).

	SEP: 24/18	2500	2506	25/12	25/18	2600	2606	26/12	26/18	27/00	27/06	27/12	Total
<b>ASCAT</b>	766	94	94	590	555	76	49	847	819	832	767	383	<b>5872</b>
<b>ASOS</b>	0	0	0	0	0	0	0	0	0	0	0	0	<b>0</b>
<b>GPSSONDE_WL150</b>	27	38	11	0	11	21	10	0	5	21	45	30	<b>219</b>
<b>METAR</b>	11	10	0	0	0	0	11	7	0	31	114	167	<b>351</b>
<b>QSCAT_HIRES</b>	4422	4478	5054	5262	1625	1399	1805	1638	2043	2132	2210	2622	<b>34690</b>
<b>SFMR_AFRC</b>	643	840	201	0	234	513	276	0	0	145	656	507	<b>4015</b>
<b>SHIP</b>	17	20	24	26	25	20	13	9	5	5	13	16	<b>193</b>
<b>WINDSAT</b>	1415	878	693	1095	842	1245	3769	4099	3861	3998	2454	2057	<b>26406</b>
<b>Total</b>	<b>7301</b>	<b>6358</b>	<b>6077</b>	<b>6973</b>	<b>3292</b>	<b>3274</b>	<b>5933</b>	<b>6600</b>	<b>6733</b>	<b>7164</b>	<b>6259</b>	<b>5782</b>	<b>71746</b>
<b>WC-130J</b>	24/17-25/03			25/20-26/06			27/02-27/14						
<b>NRL P3</b>	24/20-25/03						26/20-27/05						

Figure 16. As in Figure 14, except final observation distribution of STY Jangmi contained within the H\*Wind database following the addition of TCS08/T-PARC SFMR and dropwindsonde data for all flight times.



THIS PAGE INTENTIONALLY LEFT BLANK

### III. ANALYSIS

Through an enhanced understanding of how the surface wind fields develop, strengthen, and mature, forecast model accuracy can be improved in conjunction with providing leadership with more complete risk management criteria. This requires an in-depth understanding of the data-sparse environment throughout TC development from tropical circulation to typhoon.

The focus of this study uses aircraft observations co-located with remotely sensed observations in the WNP during the TCS08/T-PARC field experiments. From T-PARC and TCS08, eight observation systems were selected for this study: ASCAT, ASOS, GPS dropwindsonde, METAR, ship observation, SFMR, QuickSCAT, and WindSat. During TCS08/T-PARC, the WC-130J flew radial paths through the center of multiple tropical circulations to measure the radial distribution of maximum surface and flight-level winds throughout the TC intensification cycle. A total of 15 WC-130J flights occurred during Nuri, Sinlaku, and Jangmi to study structure change. In this study, eight WC-130J flights (comprising 18 radial legs, 19 center penetrations, and 221 GPS dropwindsondes) were selected, and analyses range from tropical systems of TS through STY intensity.

The HRD H\*Wind surface wind field analysis system was utilized to systematically analyze the observation sets. Comparison of the ECMWF global model analyses with the H\*Wind analyses documents the relative contributions of a gridded analysis to the details of the surface wind distribution. The aircraft GPS dropwindsondes, flight-level winds, and WC-130J SFMR surface wind comparisons allow an analysis of the three TCs eyewall slope characteristics. This study uses knots when H\*Wind analyses are compared, and for plotting radial wind distributions from aircraft data. However, this study uses  $\text{m s}^{-1}$  for all statistical calculations.

#### A. EYEWALL SLOPE

A characteristic feature of the mature TC structure is the outward slope with height of the radius of maximum winds. This slope is primarily due to two physical mechanisms. The baroclinic warm-core structure requires that the cyclone vortex

decreases with height. Also, the radius of maximum winds in the boundary layer is displaced inward due to surface friction (Kepert 2001). Increased understanding of WNP storm system eyewall slope characteristics will enable forecasters, scientists, and modelers to better estimate the surface intensity from upper-level observations.

The slope in the radius of maximum winds may be estimated by comparing the location of the flight-level wind maximum and the surface wind maximum (Powell et al. 2009). Powell et al. (2009) calculate the eyewall slope as the differences in the positions of maxima in the flight-level winds and the surface winds in a vertical plane as done in Franklin et al. (2003), and compare the maximum flight-level wind along a radial leg to the maximum surface wind along the same leg. Typical values of the ratio of maximum flight-level to surface winds based on Atlantic hurricane data vary from 0.9 to 0.83 (Franklin et al. 2003, Powell et al. 2009). In this study, data gathered during TY Nuri, TY Sinlaku, and STY Jangmi are used to define the ratio of the maximum flight-level wind speed to the maximum surface wind speed. This ratio is used to identify the slant reduction factor of surface winds in the WNP for comparison with the Atlantic ratio.

Radial plots were visually inspected to analyze the SFMR surface winds, rainrate, and flight-level winds to identify the maximum surface winds ( $V_{mxs}$ ), maximum flight-level winds ( $V_{mxf}$ ), corresponding radius of maximum surface winds ( $R_{mxs}$ ), and radius of maximum flight-level winds ( $R_{mxf}$ ). These values were identified visually to ensure that the maximum winds were associated with the typhoon core rather than a localized external rain band. The slant reduction factor  $F_{rmx}$  is defined as  $V_{mxs}/V_{mxf}$  and the relative slope of maximum wind  $R_{rmx}$  is defined as  $R_{mxs}/R_{mxf}$ . A summary of the eyewall slope terminology used in this study is included in Table 7.

Table 7. Eyewall slope terminology used in this study.

<b><u>Quantity</u></b>	<b><u>Description</u></b>
$V_{mxf}$	Maximum flight-level wind speed (kt)
$R_{mxf}$	Radius (n mi) of maximum flight-level wind speed
$V_{mxs}$	Maximum surface wind speed (kt)
$R_{mxs}$	Radius (n mi) of maximum surface wind speed
$F_{rmx}$	Slant reduction factor ( $V_{mxs}/V_{mxf}$ )
$R_{rmx}$	Relative slope of the radius of maximum wind ( $R_{mxs}/R_{mxf}$ )

In addition, comparisons are made between SFMR wind speed observations and GPS dropwindsonde wind speed observations. The GPS dropwindsonde surface wind speed is estimated from the average of the lowest 150 m wind measurements (WL150; Franklin et al. 2003). Each 200 n mi storm flight leg in the three typhoons is systematically diagnosed below, with a summary of findings at the end of this section.

## 1. TY Nuri

This study includes one TY Nuri flight that contains two radial legs. In addition to the SFMR surface winds and flight-level winds, 24 GPS dropwindsonde (0-150 m layer-averaged) observations were obtained during the flight.

An “alpha/butterfly” pattern (flight 0813W) was flown on 18-19 August to map the structural features and to coincide with satellite overpasses of TY 13W (Figure 17). The radial distribution of observed SFMR surface winds and flight-level winds (Figure 18) is used to calculate the storm parameters (Table 8).

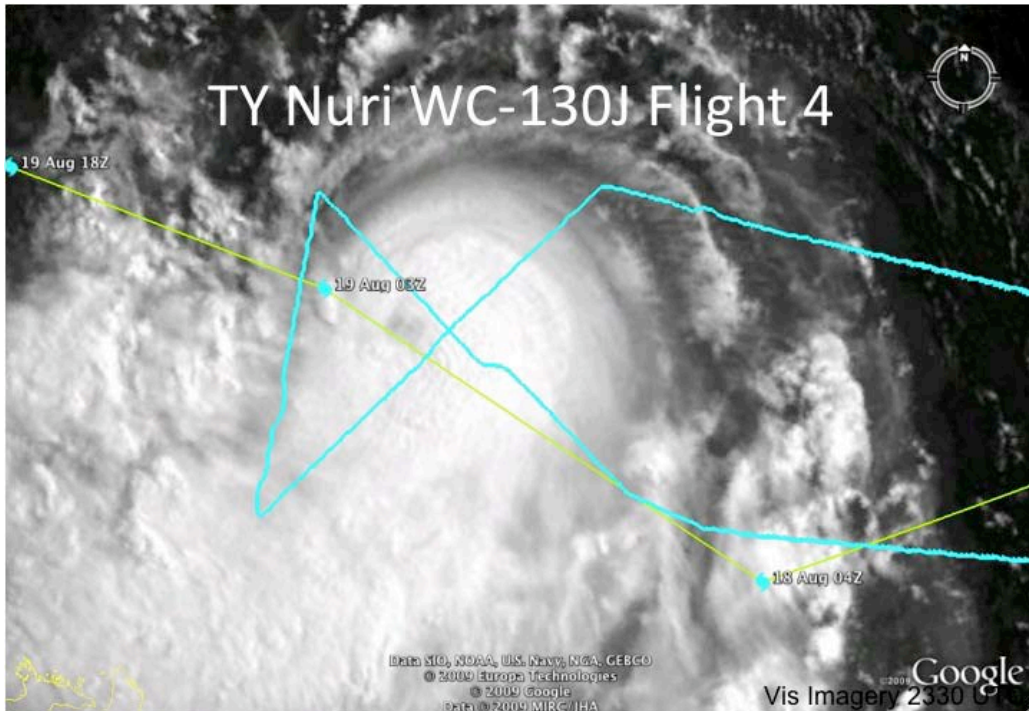


Figure 17. TY Nuri WC-130J 0813W flight track (blue), best track (yellow), and 2330 UTC 18 Aug visible imagery (imagery from NRL 2009b). Center penetrations occurred at 2125 UTC 18 Aug for leg 4-1 (SE to NW) and 2319 UTC 18 Aug for leg 4-2 (SW to NE).

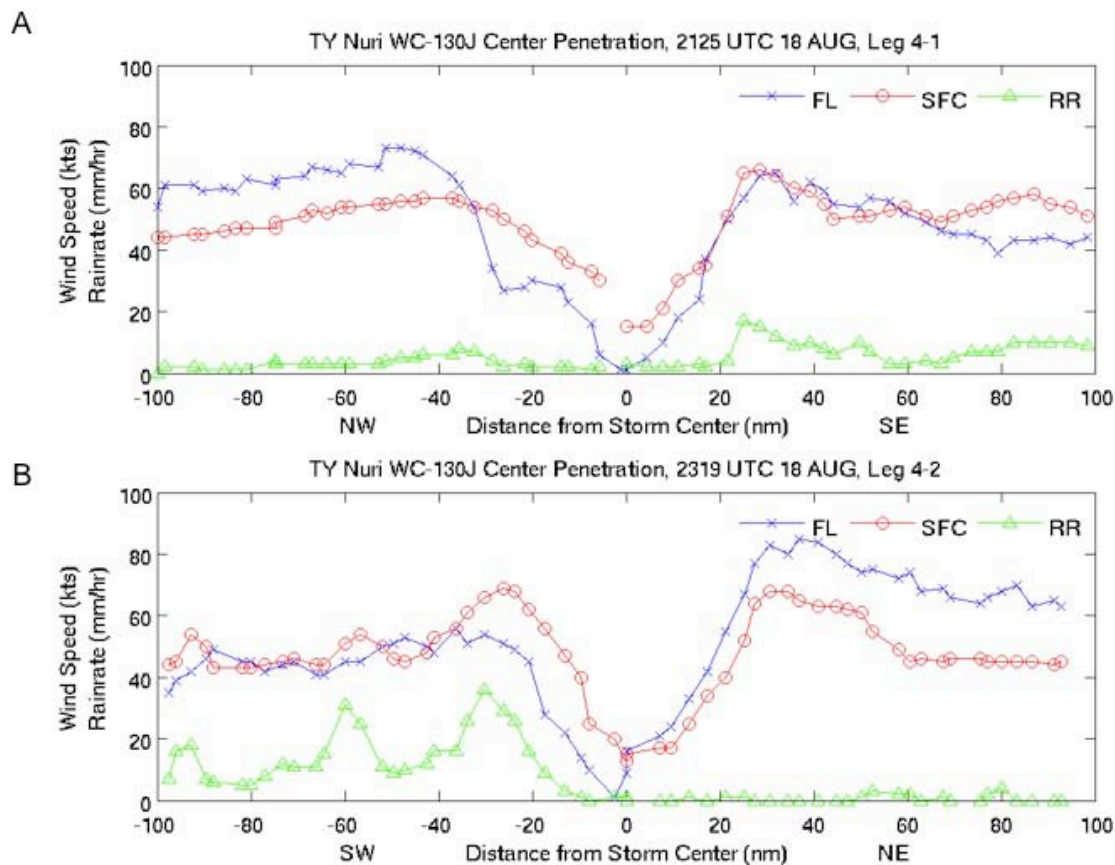


Figure 18. TY Nuri radial plots of winds and rainrates for WC-130J flight 0813W. Center penetrations occurred at 2125 UTC 18 Aug for leg 4-1 (SE to NW) and 2319 UTC 18 Aug for leg 4-2 (SW to NE). Observed SFMR surface winds (red O), flight-level winds (blue X), and rainrate (green triangle) are displayed along the 200 n mi transect. The small amount of missing data is due to aircraft maneuvering.

Table 8. TY Nuri observed and calculated parameters as defined in Table 7 for WC-130J flight 0813W.

<u>Leg</u>	<u>Inbound</u>						<u>Outbound</u>					
	<u>Vmxf</u>	<u>Rmxf</u>	<u>Vmxs</u>	<u>Rmxs</u>	<u>Frmx</u>	<u>Rrmx</u>	<u>Vmxf</u>	<u>Rmxf</u>	<u>Vmxs</u>	<u>Rmxs</u>	<u>Frmx</u>	<u>Rrmx</u>
4-1	65	32	66	28	1.02	0.88	73	48	57	37	0.78	0.77
4-2	54	30	69	26	1.28	0.87	85	37	68	31	0.80	0.84

Note the strong correlation between the magnitudes of the rainrate and the surface winds at -30, -60, and -90 n mi (Figure 18b) along leg 4-2 and at 25 n mi along leg 4-1 (Figure 18a). These variations correspond to crossing the significant rainbands that are visible in the satellite imagery (Figure 17). In each of the three legs, the slant reduction factor is greater than 1.0, which reflects the influence of the outer wind maxima associated with the rainbands.

The SFMR wind speed observations correlate well ( $r = 0.87$ ) with the GPS dropwindsondes, with a RMSE of  $2.26 \text{ m s}^{-1}$ . A slight positive bias exists below  $20 \text{ m s}^{-1}$  and a slight negative bias exists above  $20 \text{ m s}^{-1}$  (Figure 19a).

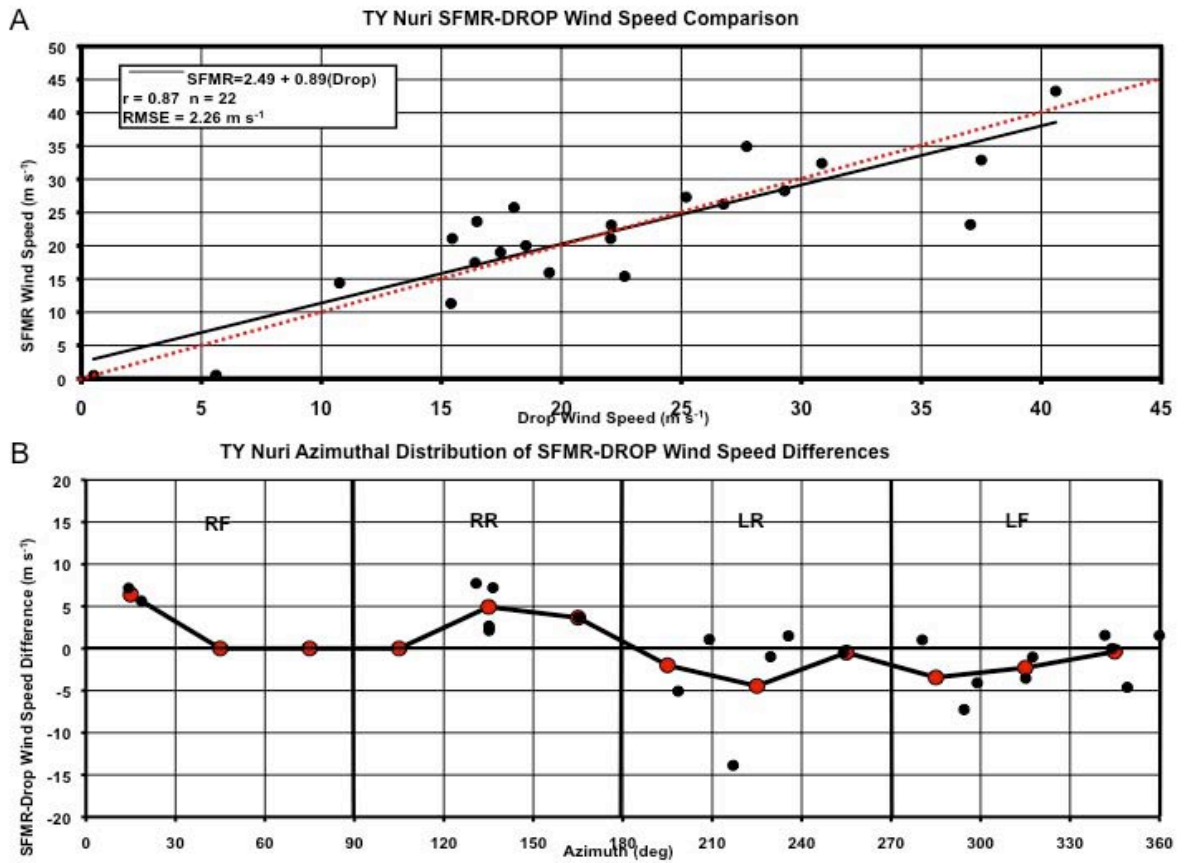


Figure 19. (a) SFMR wind speed ( $\text{m s}^{-1}$ ) versus GPS dropwindsonde wind speed ( $\text{m s}^{-1}$ ) for TY Nuri. The black line indicates SFMR-dropwindsonde best fit ( $\text{SFMR} = 2.49 + 0.89(\text{Drop})$ ,  $\text{RMSE} = 2.26 \text{ m s}^{-1}$ ), and the red-dotted line indicates the neutral fit. (b) Azimuthal distribution of SFMR-drop wind speed differences by storm quadrant relative to the storm heading. Wind speed ( $\text{m s}^{-1}$ ) differences are on the vertical axis, azimuthal variation (deg.) is on the horizontal axis, and the red dots indicate averages over  $30^\circ$  azimuthal slices.

Uhlhorn and Black (2003) explained that an azimuthal pattern of SFMR and dropwindsonde wind speed differences may exist due to non-wind sources of surface roughness (e.g., foam on the sea surface). A negative bias on SFMR-dropwindsonde wind speed differences occurs in the right-rear (RR) quadrant (relative to storm heading) where swell and wind move in the same direction, which leads to less foam and thus a smaller SFMR wind speed estimate. Opposite conditions may exist in the left-front (LF) quadrant where swells may propagate against the wind. However, these biases are not evident in the differences between SFMR and dropwindsonde data in Nuri (Figure 19b). However, the data sample is very small. This potential bias will be examined more fully in other storms. During the entire flight period, Typhoon Nuri had a mean (standard deviation)  $F_{rmx}$  of 0.97 ( $\pm 0.23$ ) and a mean (standard deviation)  $R_{rmx}$  of 0.84 ( $\pm 0.05$ ).

## **2. TY Sinlaku**

Four TY Sinlaku flights are available that contain eight radial legs. In addition to the SFMR surface winds and flight-level winds, 97 GPS dropwindsonde (0-150 m layer-averaged) observations were obtained throughout all the flights.

An “alpha” pattern (flight 0133W) was flown on 9 September to map the structural features and to coincide with satellite overpasses of TS 15W (Figure 20). During this first flight, a radial distribution of SFMR surface winds and flight-level winds (Figure 21) identify a broad center. Because of the broad center, the relative wind maxima along each radial leg are not well defined as is typical of a mature TC. Furthermore, the asymmetrical distribution of flight-level and surface winds across the center indicates that the TC structure may have been offset from the vertical.



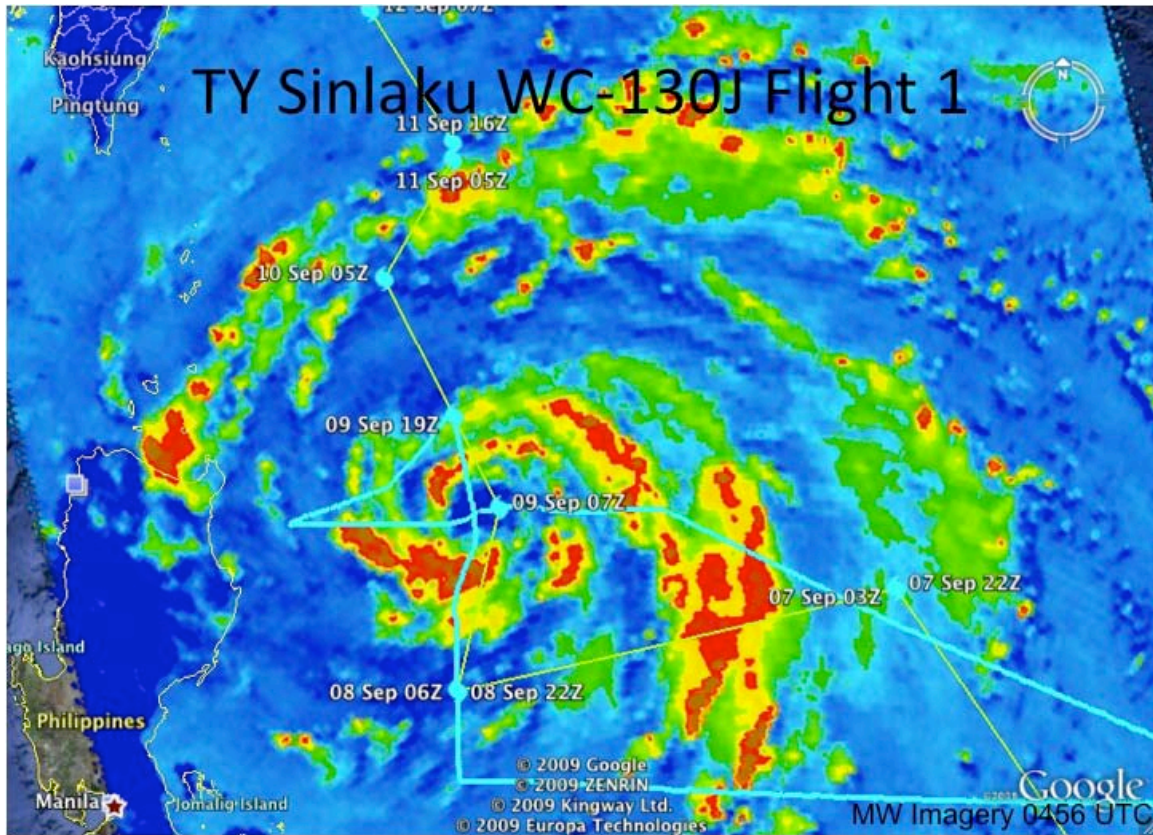


Figure 20. As in Figure 17, except for TY Sinlaku WC-130J 0133W flight track and 0456 UTC 9 Sep enhanced MW imagery. Center penetrations occurred at 0504 UTC 9 Sep for leg 1-1 (S to N) and 0638 UTC 9 Sep for leg 1-2 (W to E).

On the north side of flight 1-1 (Figure 21a) and on the west side of flight 1-2 (Figure 21b) the higher surface wind compared to flight-level wind indicates that the low-level wind maximum was not directly under the flight-level center. Therefore, the slant reduction factor ( $F_{rmx}$ ) on the inbound leg 1-2 and outbound leg 1-1 are considerably larger than 1.0 and the slope of the radius of maximum winds ( $R_{rmx}$ ) on the outbound leg 1-1 is equal to 1.0 (Table 9). Comparison of this complex structure of Sinlaku with the values of  $F_{rmx}$  and  $R_{rmx}$  for a mature TC is then less valid.



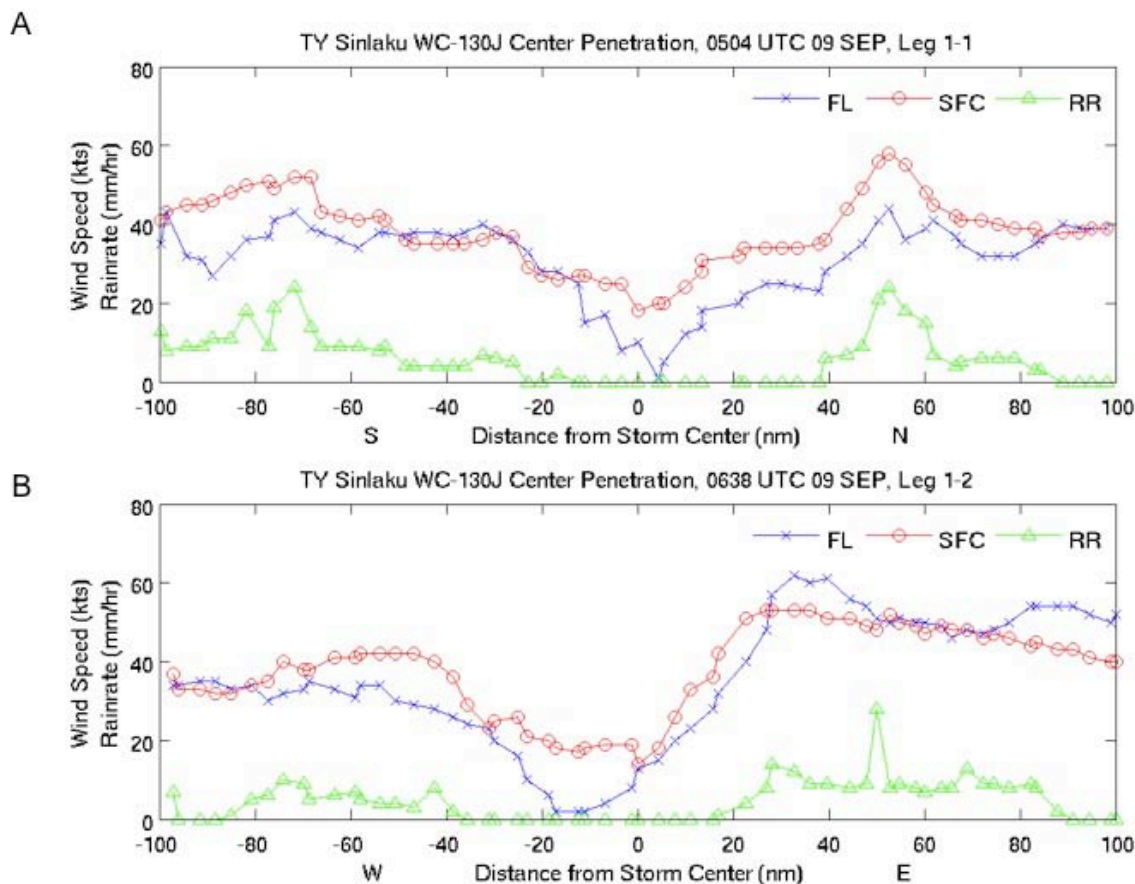


Figure 21. As in Figure 18, except for TY Sinlaku during WC-130J flight 0133W. Center penetrations occurred at 0504 UTC 9 Sep for leg 1-1 (S to N) and 0638 UTC 9 Sep for leg 1-2 (W to E).

Table 9. TY Sinlaku observed and calculated parameters as defined in Table 7 for WC-130J flight 0133W.

Leg	Inbound						Outbound					
	Vmxf	Rmxf	Vmxs	Rmxs	Frmx	Rrmx	Vmxf	Rmxf	Vmxs	Rmxs	Frmx	Rrmx
1-1	40	32	38	30	0.95	0.94	44	50	58	50	1.32	1.00
1-2	34	54	42	47	1.24	0.87	62	33	53	27	0.85	0.82

An “alpha” pattern (flight 0233W) was also flown on 10 September (Figure 22). The radial distribution of SFMR surface winds and flight-level winds (Figure 23) illustrate the intensification and contraction of the eyewall (maximum winds) compared to the previous flight (Figure 21). For this flight, the slant ratio reduction factor (Frmx) values between 0.85 and 0.90 and the relative slopes of maximum winds (Rrmx) of 0.76

to 0.84 on leg 2-1 (Table 10) are representative of values obtained by Powell et al. (2009) for a large sample of Atlantic hurricane data. On leg 2-2, the range of Rrmx values is somewhat larger (0.65 to 1.00).

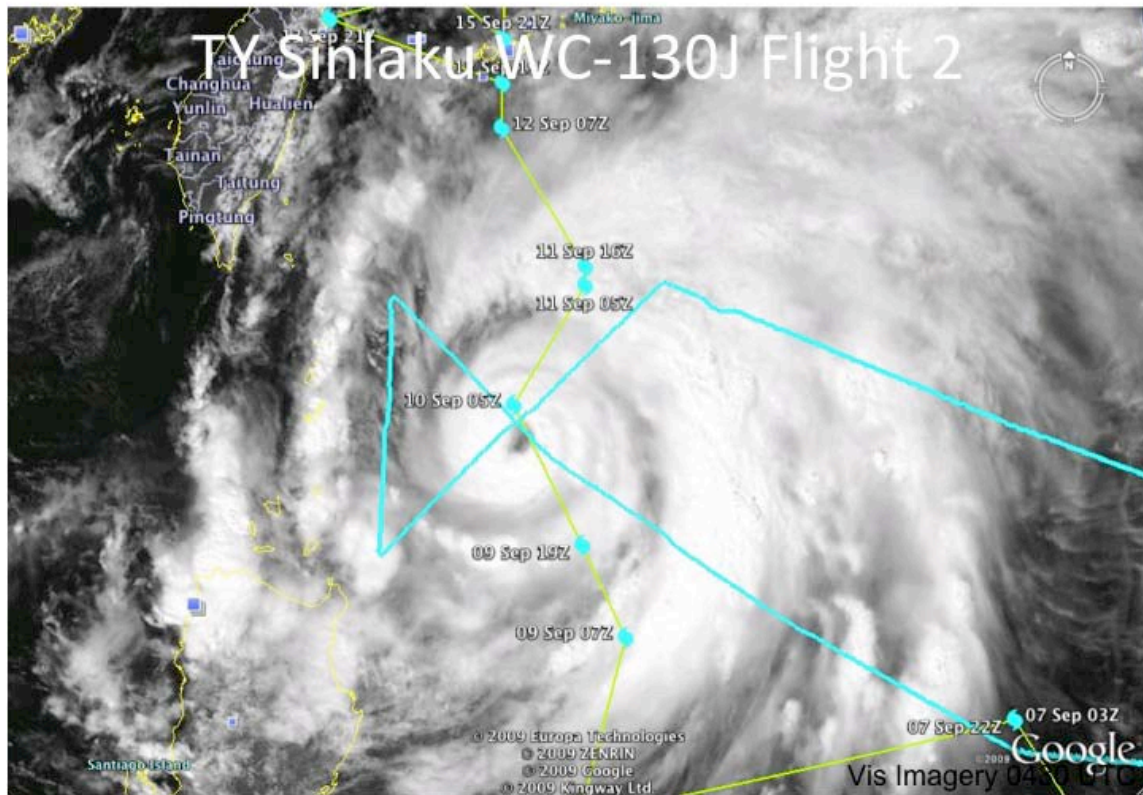


Figure 22. As in Figure 17, except for TY Sinlaku WC-130J 0233W flight track and 0430 UTC visible imagery. Center penetrations occurred at 0606 UTC 10 Sep for leg 2-1 (SE to NW) and 0753 UTC 10 Sep for leg 2-2 (SW to NE).

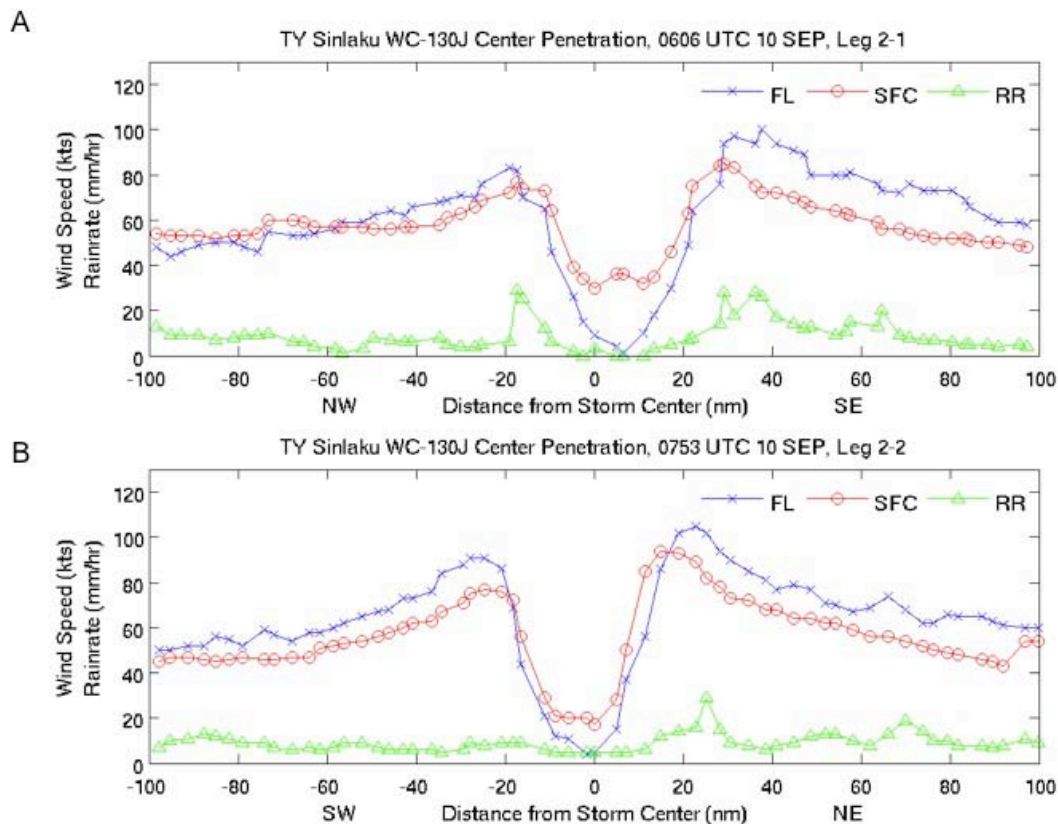


Figure 23. As in Figure 18, except for TY Sinlaku during WC-130J flight 0233W. Center penetrations occurred at 0606 UTC 10 Sep for leg 2-1 (SE to NW) and 0753 UTC 10 Sep for leg 2-2 (SW to NE).

Table 10. TY Sinlaku observed and calculated parameters as defined in Table 7 for WC-130J flight 0233W.

Leg	Inbound						Outbound					
	V <sub>mx</sub> f	R <sub>mx</sub> f	V <sub>mx</sub> s	R <sub>mx</sub> s	F <sub>rm</sub> x	R <sub>rm</sub> x	V <sub>mx</sub> f	R <sub>mx</sub> f	V <sub>mx</sub> s	R <sub>mx</sub> s	F <sub>rm</sub> x	R <sub>rm</sub> x
2-1	100	38	85	29	0.85	0.76	83	19	74	16	0.89	0.84
2-2	91	25	77	25	0.85	1.00	105	23	94	15	0.90	0.65

The third “alpha” pattern (flight 0433W) into TY Sinlaku was flown on 11 September (Figure 24). Although the maximum winds near the center had decreased (Figure 25) from the previous flight (Figure 23), the center remained well-defined. The slant reduction factor (F<sub>rm</sub>x) values ranging from 0.86 to 0.94 (Table 11) are quite consistent with the Atlantic values in Powell et al. (2009). Three of the ratios of maximum wind (R<sub>rm</sub>x) are 0.70 to 0.71, which are somewhat smaller than in Powell et

al. (2009). An interesting feature at this time (Figure 25) was that the winds did not decrease with radius outside the center as on the previous flight. Rather, secondary wind maxima that are as large or larger than the inner wind maxima are found around 90 n mi radius in all four quadrants. This secondary wind maxima is associated with a cloud band (Figure 24) and indicates a secondary eyewall has formed.

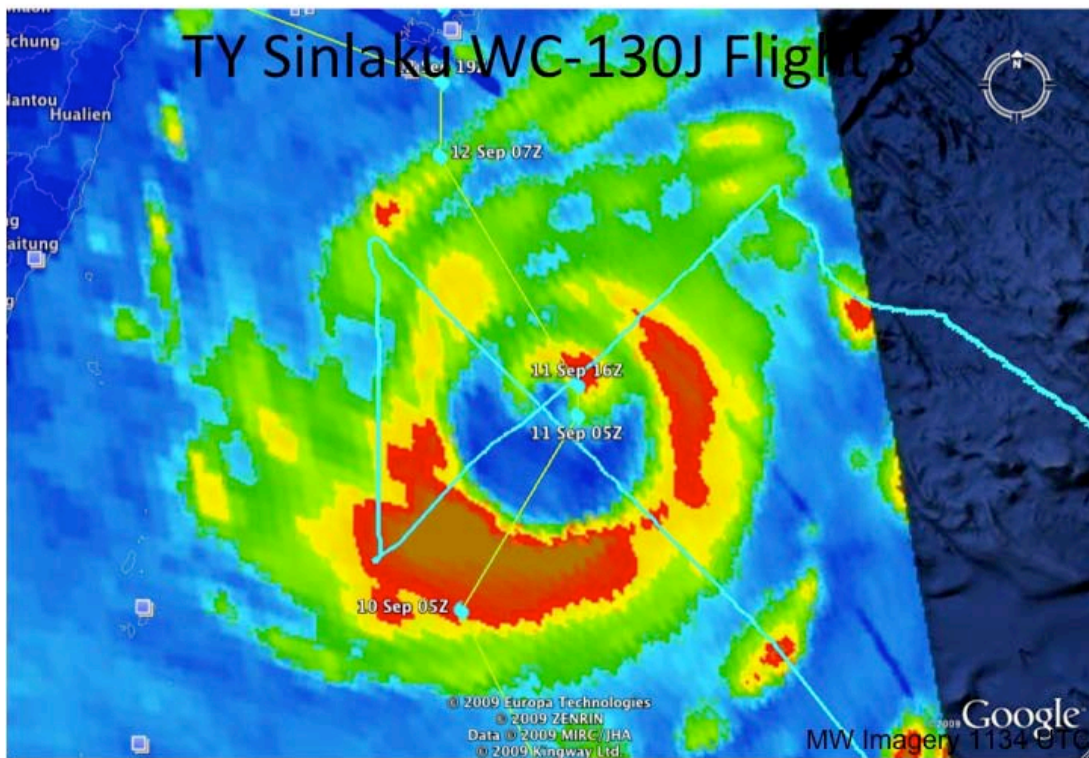


Figure 24. As in Figure 17, except for TY Sinlaku WC-130J 0433W flight track and 1134 UTC enhanced MW imagery. Center penetrations occurred at 1207 UTC 11 Sep for leg 3-1 (SE to NW) and 1331 UTC 11 Sep for leg 3-2 (SW to NE).



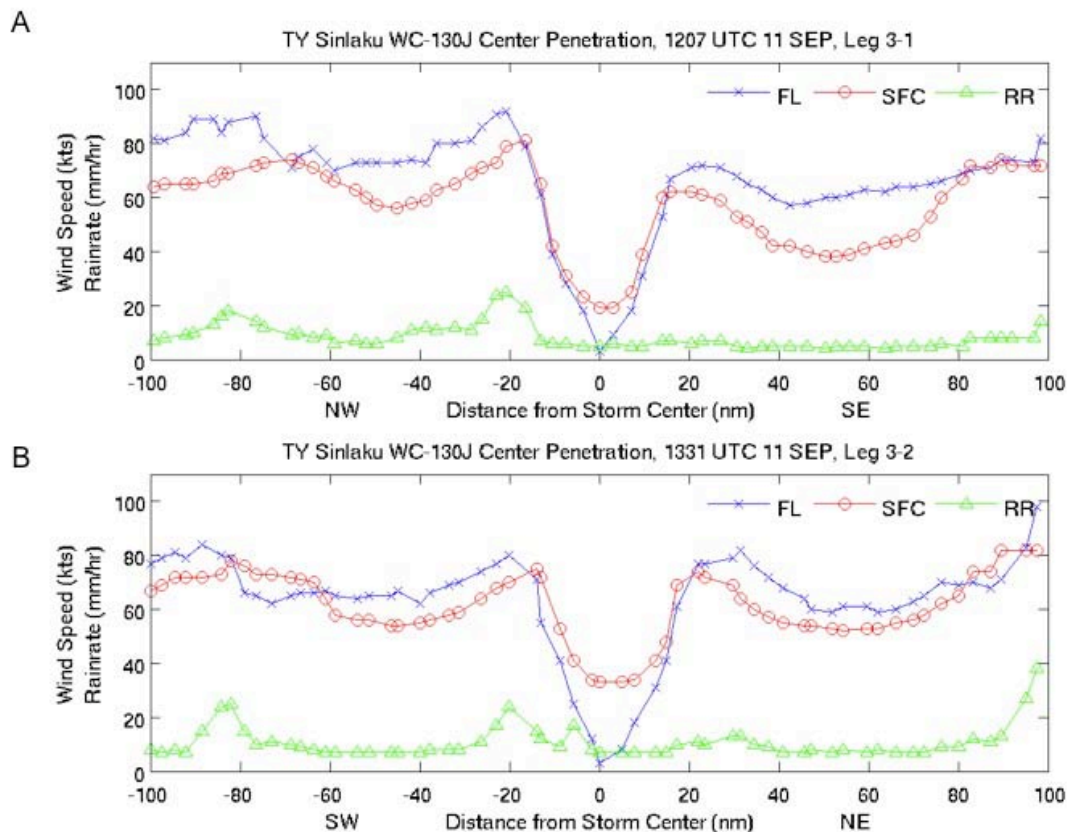


Figure 25. As in Figure 18, except for TY Sinlaku during WC-130J flight 0433W. Center penetrations occurred at 1207 UTC 11 Sep for leg 3-1 (SE to NW) and 1331 UTC 11 Sep for leg 3-2 (SW to NE).

Table 11. TY Sinlaku observed and calculated parameters as defined in Table 7 for WC-130J flight 0433W.

<u>Leg</u>	<b>Inbound</b>						<b>Outbound</b>					
	<u>V<sub>mx</sub>f</u>	<u>R<sub>mx</sub>f</u>	<u>V<sub>mx</sub>s</u>	<u>R<sub>mx</sub>s</u>	<u>F<sub>rm</sub>x</u>	<u>R<sub>rm</sub>x</u>	<u>V<sub>mx</sub>f</u>	<u>R<sub>mx</sub>f</u>	<u>V<sub>mx</sub>s</u>	<u>R<sub>mx</sub>s</u>	<u>F<sub>rm</sub>x</u>	<u>R<sub>rm</sub>x</u>
3-1	72	23	62	16	0.86	0.70	92	21	81	17	0.88	0.81
3-2	80	20	75	14	0.94	0.70	82	31	74	22	0.90	0.71

The final “alpha” pattern (flight 0533W) prior to recurvature of TY Sinlaku was flown on 12 September (Figure 26). As Sinlaku approached Taiwan (Figure 26), it was clear that the central region of the storm was quite broad (Figure 27). Although no intermediate flights are available to document the evolution, one interpretation is that the inner eye region on the previous day has dissipated and the secondary eyewall has become the primary eyewall. Except in the NW quadrant adjacent to Taiwan, the

previous secondary eyewall has contracted in the other three quadrants with an associated increase in maximum winds, as expected for a contracting eyewall. If this sequence is correct, this event would be termed an eyewall replacement cycle. However, the slant reduction factor values (Table 12) and slope of maximum winds have remained similar to the previous flights, and the slope of maximum winds has continued to be smaller than the values in Powell et al. (2009).

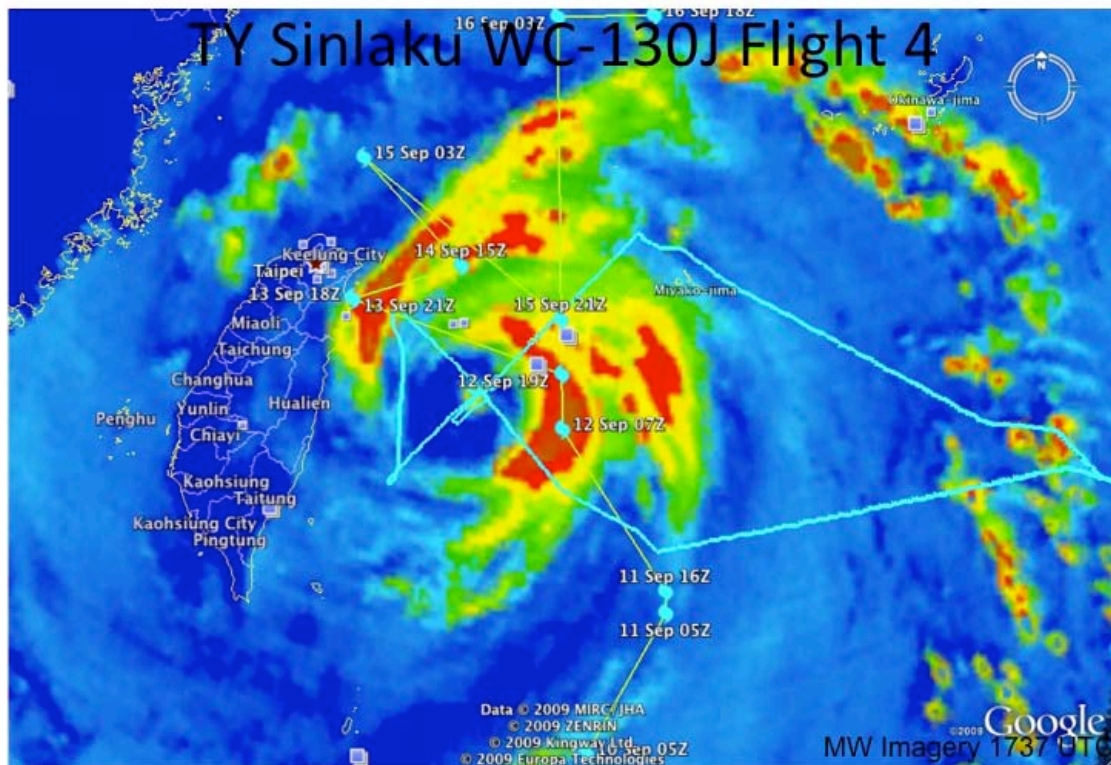


Figure 26. As in Figure 17, except for TY Sinlaku WC-130J 0533W flight track and 1737 UTC enhanced MW imagery. Center penetrations occurred at 1646 UTC 12 Sep for leg 4-1 (SE to NW) and 1813 UTC 12 Sep for leg 4-2 (SW to NE).

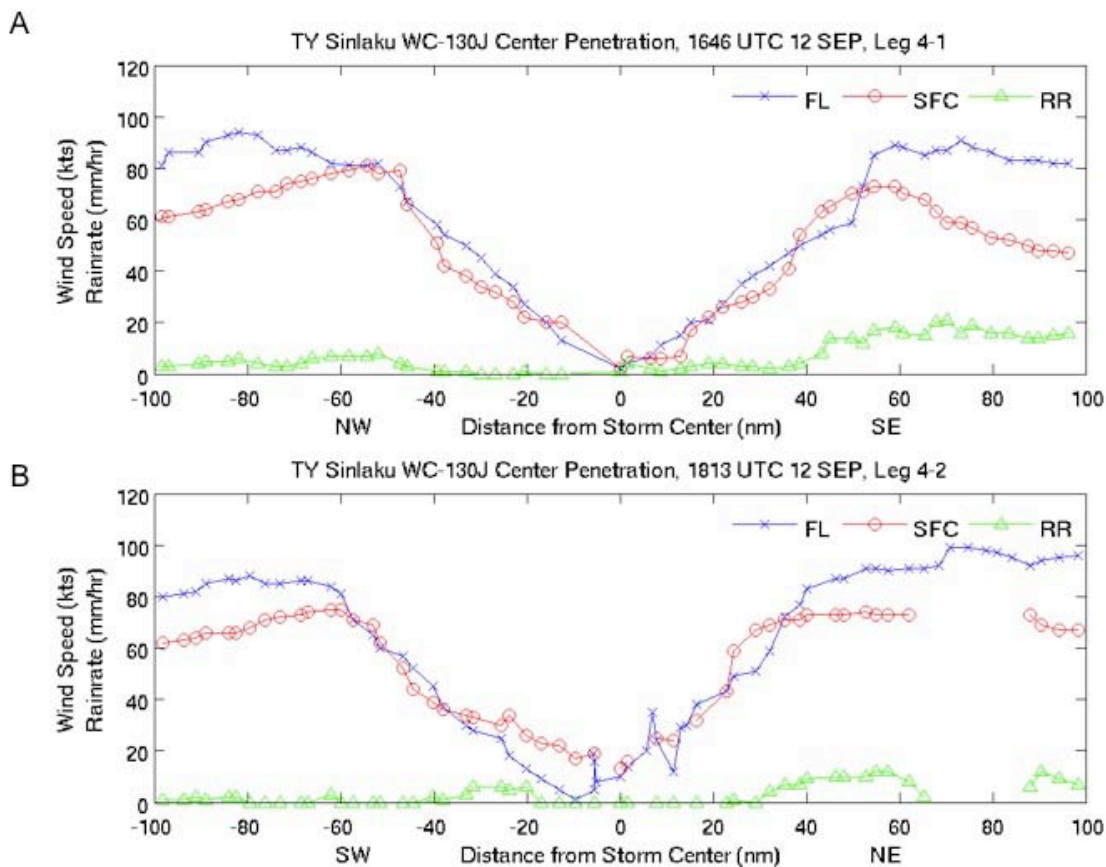


Figure 27. As in Figure 18, except for TY Sinlaku during WC-130J flight 0533W. Center penetrations occurred at 1646 UTC 12 Sep for leg 4-1 (SE to NW) and 1813 UTC 12 Sep for leg 4-2 (SW to NE).

Table 12. TY Sinlaku observed and calculated parameters as defined in Table 7 for WC-130J flight 0533W.

Leg	Inbound						Outbound					
	V <sub>mx</sub> f	R <sub>mx</sub> f	V <sub>mx</sub> s	R <sub>mx</sub> s	F <sub>rm</sub> x	R <sub>rm</sub> x	V <sub>mx</sub> f	R <sub>mx</sub> f	V <sub>mx</sub> s	R <sub>mx</sub> s	F <sub>rm</sub> x	R <sub>rm</sub> x
4-1	91	73	73	55	0.80	0.75	94	82	81	54	0.86	0.66
4-2	87	84	75	60	0.86	0.71	87	46	67	29	0.77	0.63

Throughout the flights into TY Sinlaku, the SFMR wind speed observations correlate well ( $r = 0.88$ ) to the GPS dropwindsondes, with a RMSE of  $2.33 \text{ m s}^{-1}$  (Figure 28a). As was the case for Nuri (Figure 19), a slight positive bias exists below  $35 \text{ m s}^{-1}$  and a slight negative bias is found above  $35 \text{ m s}^{-1}$ . In this Sinlaku case, the azimuthal variations of the SFMR and dropwindsonde differences do indicate a foam-related bias as

found in Uhlhorn and Black (2003), such that a positive bias occurs in the right-front and left-front (RF, LF) storm quadrants (Figure 28b) and a near-zero to slightly negative bias is found in the right-rear (RR) quadrant. Combining observations from the four flights, TY Sinlaku had a mean (standard deviation) Frmx of  $0.92 (\pm 0.15)$  and a mean (standard deviation) Rrmx of  $0.78 (\pm 0.12)$ . These Frmx values are slightly larger than have been found in a large sample of Atlantic hurricanes (Powell et al. 2009). If the first flight when Sinlaku was still a TS is removed, the mean (standard deviation) Frmx is  $0.86 (\pm 0.04)$  and the mean (standard deviation) Rrmx is  $0.74 (\pm 0.1)$ , which are more similar to the Atlantic data.

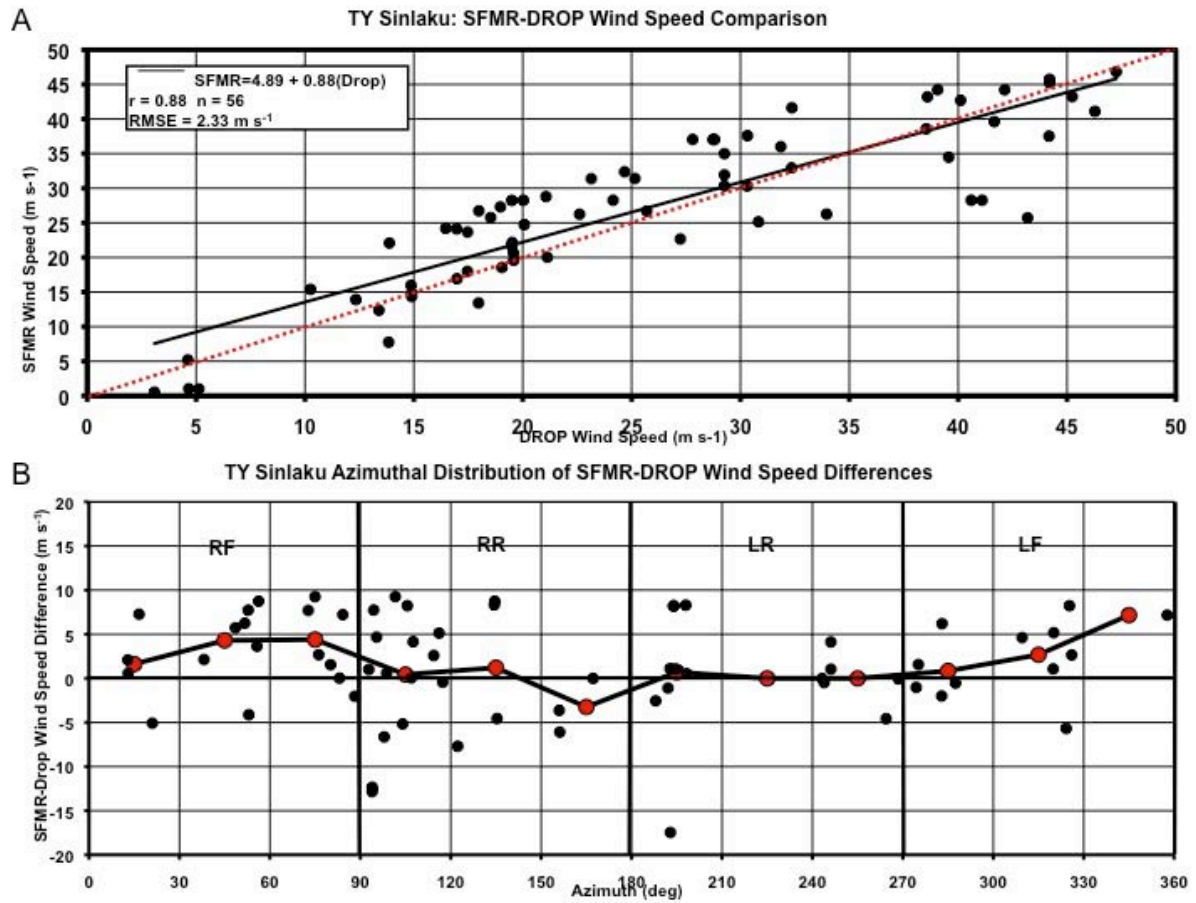


Figure 28. As in Figure 19, except for TY Sinlaku SFMR-dropwindsonde wind speed comparisons. The SFMR-dropwindsonde winds best fit curve ( $\text{SFMR} = 4.89 + 0.88(\text{Drop})$  with a  $\text{RMSE} = 2.33 \text{ m s}^{-1}$ ).



### 3. STY Jangmi

Three STY Jangmi flights are available that contain eight radial legs. In addition to the SFMR surface winds and flight-level winds, 100 GPS dropwindsonde (0-150 m layer-averaged) observations were obtained throughout the three flights.

An “alpha/butterfly” pattern (flight 0247W) was flown in Jangmi on 24-25 September to map the structure/intensity changes as it intensified to TY strength and to coincide with satellite overpasses of TS 17W (Figure 29).

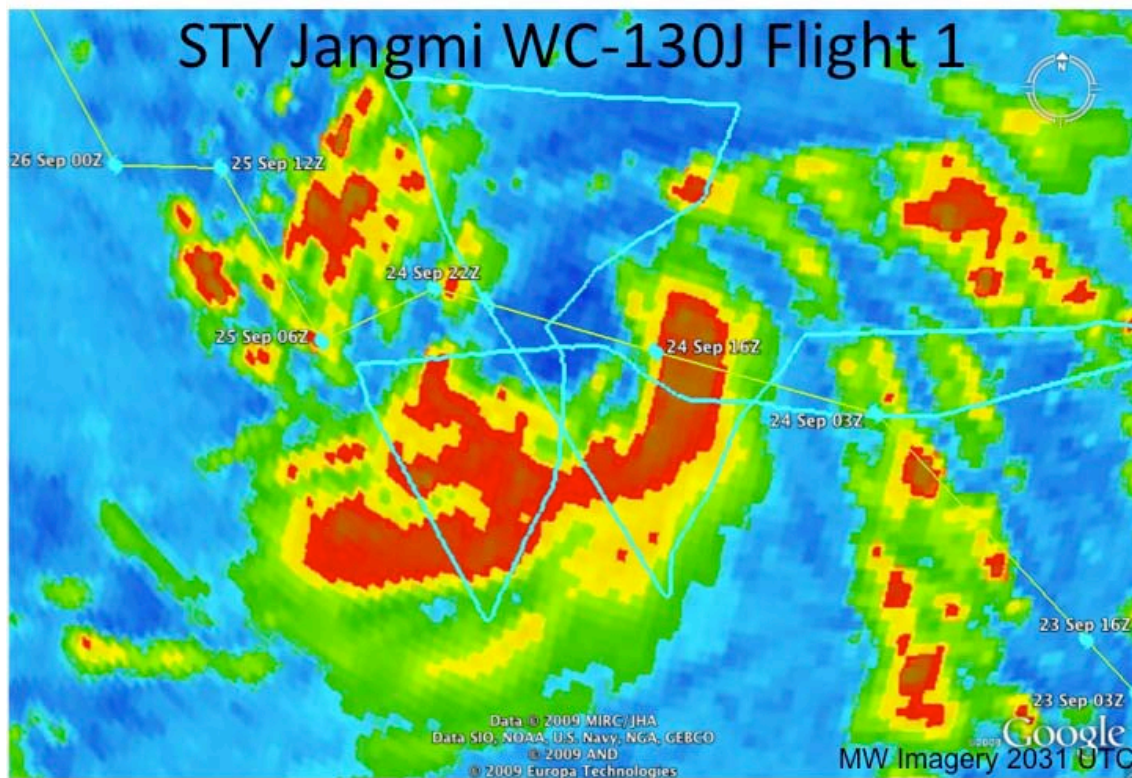


Figure 29. As in Figure 17, except for STY Jangmi WC-130J 0247W flight track and 2031 UTC enhanced MW imagery. Center penetrations occurred at 1946 UTC 24 Sep for leg 1-1 (E to W), 2146 UTC 24 Sep for leg 1-2 (SW to NE), and 2353 UTC 24 Sep for leg 1-3 (NW to SE).

In the radial distribution of observed SFMR surface winds and flight-level winds (Figure 30), a very broad center with only slightly stronger winds in the eastern quadrants is depicted. Because of the broad center, the relative wind maxima along each radial leg are not well defined as typical of a mature TC. Furthermore, the distribution of surface

winds to flight-level winds indicates that the low-level center is not directly under the flight-level center. Therefore, the slant reduction factors are generally large with values between 0.85 to 2.0 (Table 13). Large variations in the slope of the radius of maximum winds are also calculated with values ranging from 0.38 to 1.09 (Table 13).

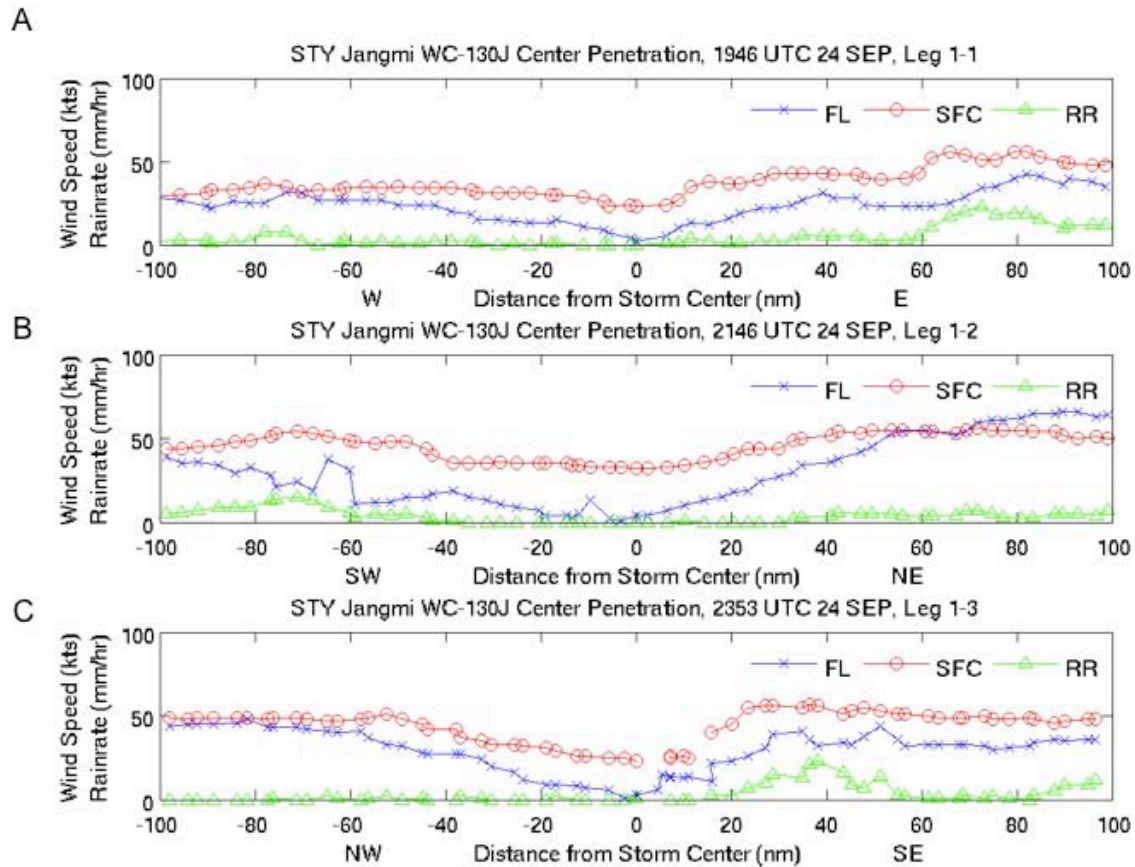


Figure 30. As in Figure 18, except for STY Jangmi during WC-130J flight 0247W. Center penetrations occurred at 1946 UTC 24 Sep for leg 1-1 (E to W), 2146 UTC 24 Sep for leg 1-2 (SW to NE), and 2353 UTC 24 Sep for leg 1-3 (NW to SE).

Table 13. STY Jangmi observed and calculated parameters as defined in Table 7 for WC-130J flight 0247W.

Leg	Inbound						Outbound					
	V <sub>mxf</sub>	R <sub>mxf</sub>	V <sub>mxs</sub>	R <sub>mxs</sub>	F <sub>rmx</sub>	R <sub>rmx</sub>	V <sub>mxf</sub>	R <sub>mxf</sub>	V <sub>mxs</sub>	R <sub>mxs</sub>	F <sub>rmx</sub>	R <sub>rmx</sub>
1-1	31	39	38	15	1.23	0.38	15	17	30	17	2.00	1.00
1-2	38	65	54	71	1.42	1.09	66	90	56	72	0.85	0.80
1-3	48	82	51	52	1.06	0.63	44	51	57	36	1.30	0.71

The second “alpha” pattern (flight 0447W) was flown on 25-26 September (Figure 31). The radial distribution of observed SFMR surface winds and flight-level winds (Figure 32) reveal a broad but more mature TC with a better defined center. The maximum winds are observed in the NE quadrant, but this maximum is broad rather than having a well-defined peak wind. The asymmetries in the relative values of flight-level winds and surface winds indicate that there is still some offset between the surface and flight-level center. While the inbound legs 2-1 and 2-2 have slant reduction factors that are equal to or larger than 1.0, the outbound leg 2-1 has a value of only 0.62 (Table 14). As the center became well defined, the slope of the radius of maximum winds became similar to those found by Powell et al. (2009) for the Atlantic hurricane data, although the range of values from 0.68 to 1.0 is quite large (Table 14).

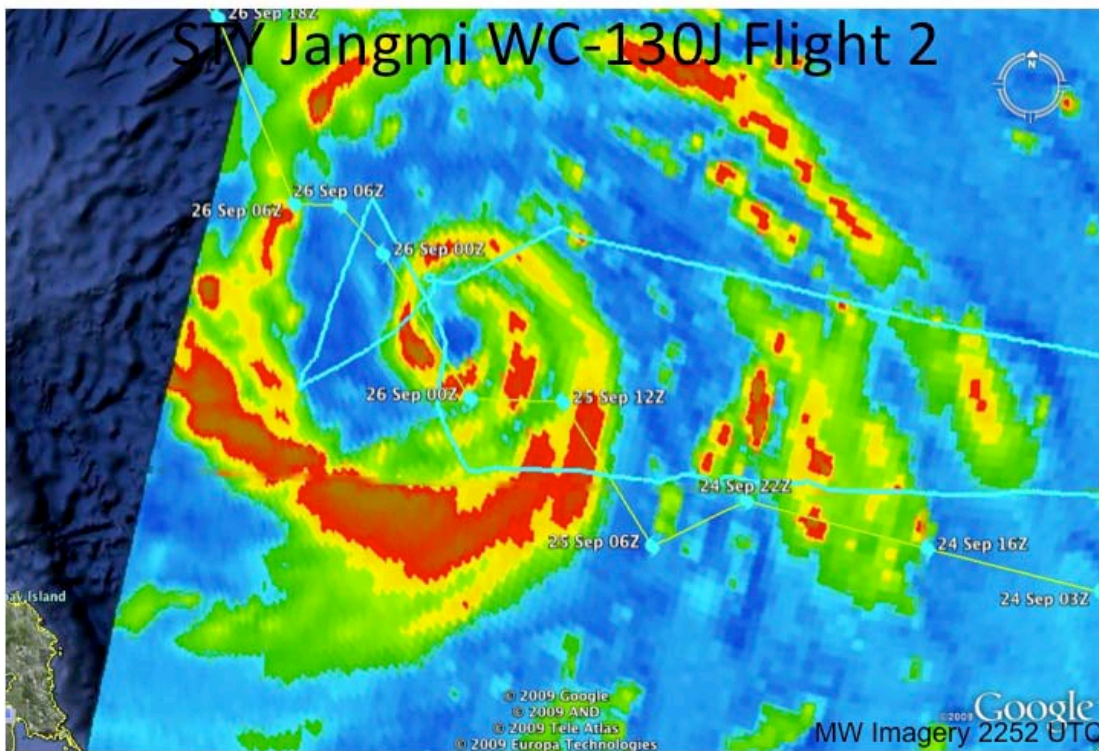


Figure 31. As in Figure 17, except for STY Jangmi WC-130J 0447W flight track and 2252 UTC enhanced MW imagery. Center penetrations occurred at 2345 UTC 25 Sep for leg 2-1 (SE to NW) and 0113 UTC 26 Sep for leg 2-2 (SW to NE).



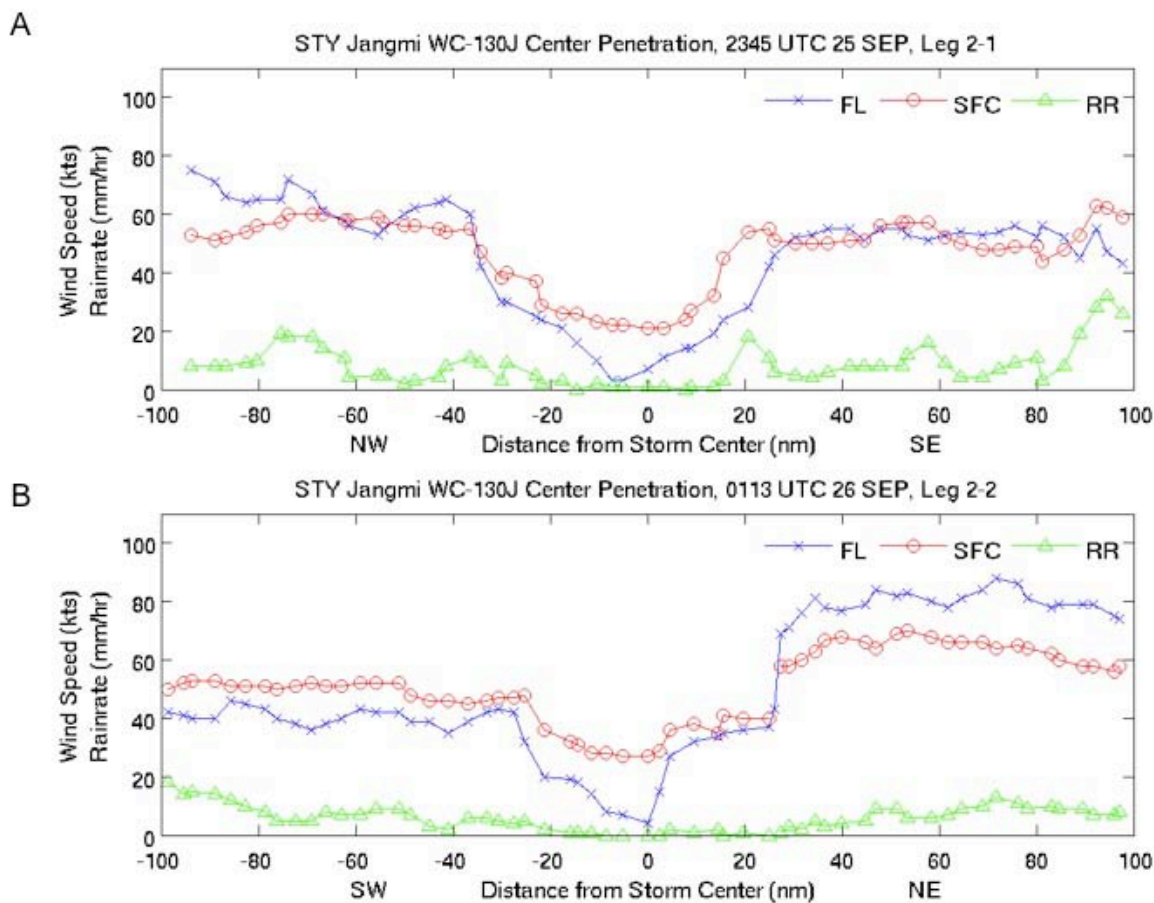


Figure 32. As in Figure 18, except for STY Jangmi during WC-130J flight 0447W. Center penetrations occurred at 2345 UTC 25 Sep for leg 2-1 (SE to NW) and 0113 UTC 26 Sep for leg 2-2 (SW to NE).

Table 14. STY Jangmi observed and calculated parameters as defined in Table 7 for WC-130J flight 0447W.

Leg	Inbound						Outbound					
	<u>Vmxf</u>	<u>Rmxf</u>	<u>Vmxs</u>	<u>Rmxs</u>	<u>Frmx</u>	<u>Rrmx</u>	<u>Vmxf</u>	<u>Rmxf</u>	<u>Vmxs</u>	<u>Rmxs</u>	<u>Frmx</u>	<u>Rrmx</u>
2-1	55	37	55	25	1.00	0.68	65	41	40	29	0.62	0.71
2-2	43	31	48	25	1.12	0.81	69	28	58	28	0.84	1.00

The final “alpha/butterfly” pattern (flight 0747W) was flown in STY Jangmi on 27 September (Figure 33). During this flight, three radial legs were flown through the center (Figure 33), except two separate center penetrations occurred along leg 3-3 (Figure 34 and Figure 35). However, only the maximum values of the entire flight leg were used

for ratio calculations of leg 3-3. In all of the radial distributions of observed SFMR surface winds and flight-level winds, a very well defined center is observed as Jangmi was at STY intensity at this time. Both the slant reduction factors and the slopes of the radius of maximum winds (Table 15) are consistent with Powell et al. (2009), which indicates these factors are more applicable to the strong TCs than the TS stage.

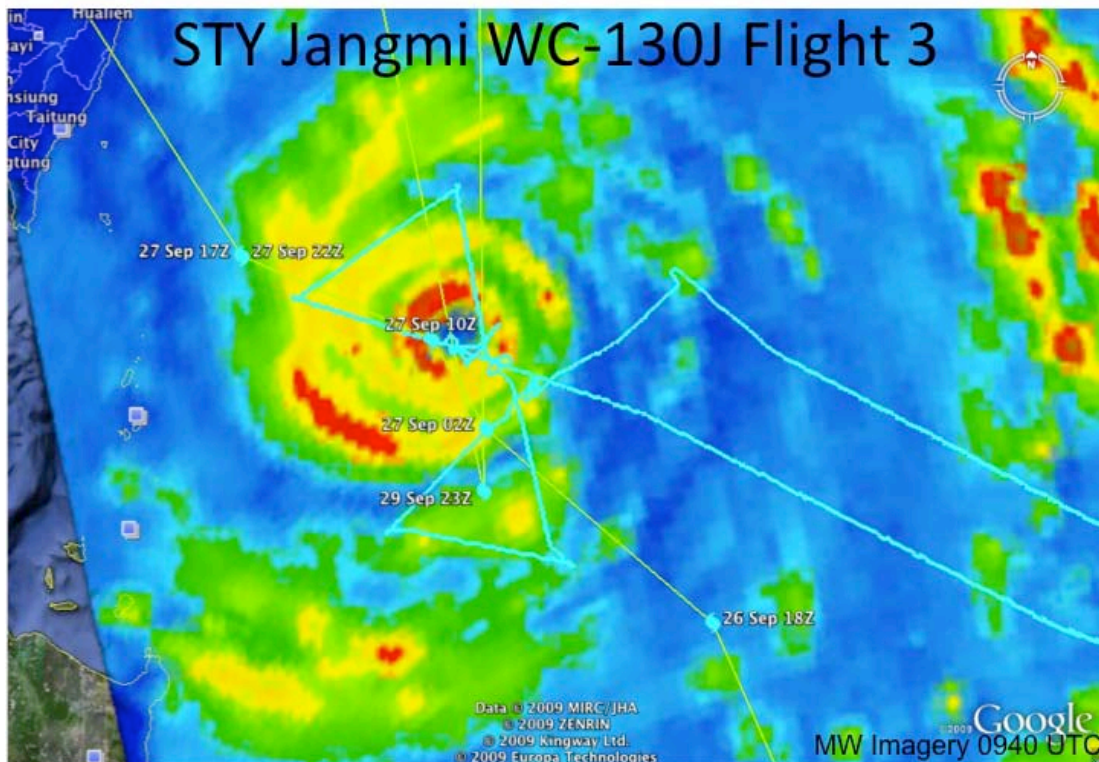


Figure 33. As in Figure 17, except for STY Jangmi WC-130J 0747W flight track and 0940 UTC enhanced MW imagery. Center penetrations occurred at 0621 UTC 27 Sep for leg 3-1 (NE to SW), 0755 UTC 27 Sep for leg 3-2 (SE to NW), 0924 UTC 27 Sep for leg 3-3a (SW to NE), and 0944 UTC 27 Sep for leg 3-3b (SW to NE).

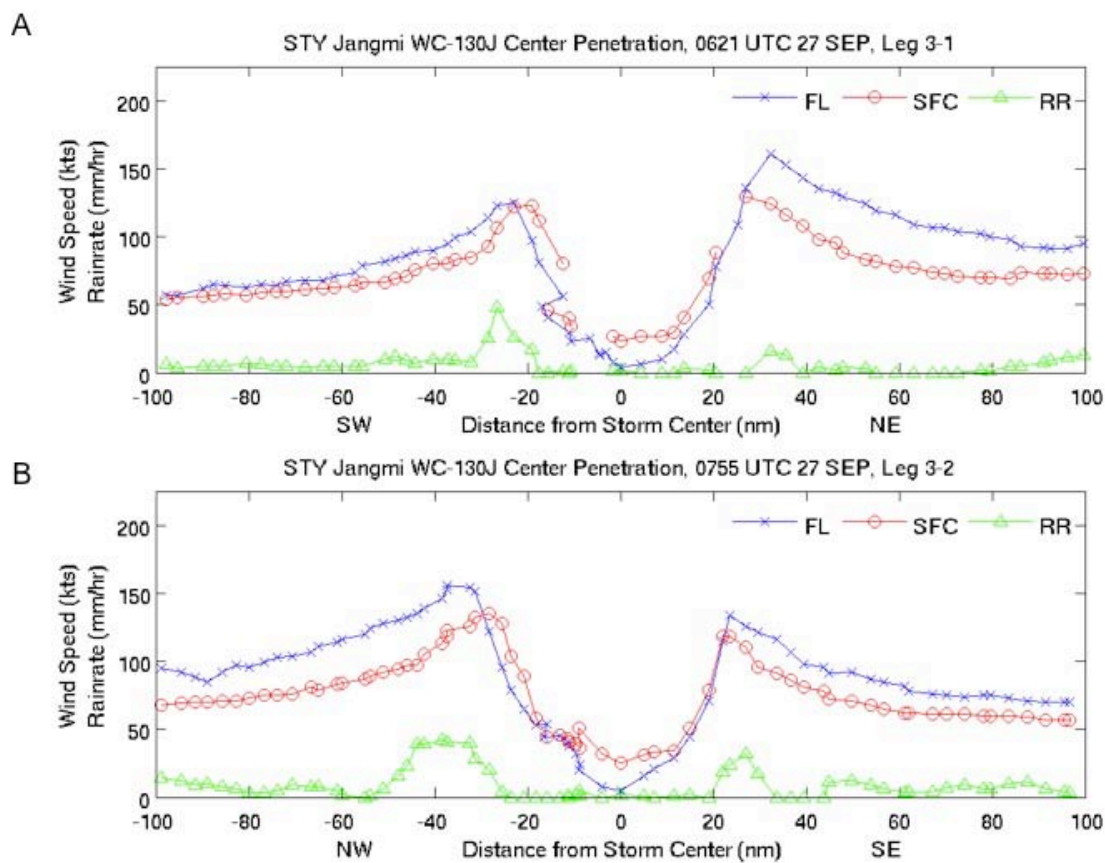


Figure 34. As in Figure 18, except for STY Jangmi during WC-130J flight 0747W. Center penetrations occurred at 0621 UTC 27 Sep for leg 3-1 (NE to SW) and 0755 UTC 27 Sep for leg 3-2 (SE to NW).

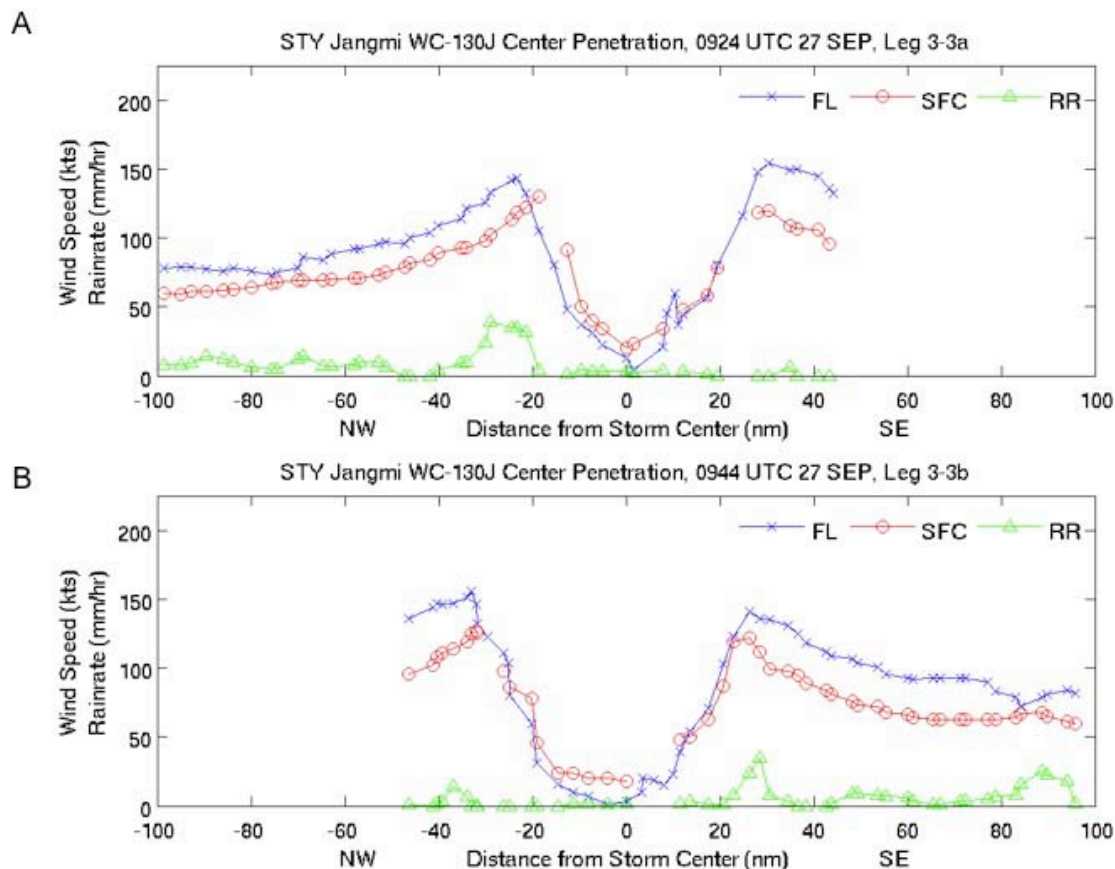


Figure 35. As in Figure 18, except for STY Jangmi during WC-130J flight 0747W. Center penetrations occurred at 0924 UTC 27 Sep for leg 3-3a (SW to NE), and 0944 UTC 27 Sep for leg 3-3b (SW to NE).

Table 15. STY Jangmi observed and calculated parameters as defined in Table 7 for WC-130J flight 0747W.

Leg	Inbound						Outbound					
	Vmxf	Rmxf	Vmxs	Rmxs	Frmx	Rrmx	Vmxf	Rmxf	Vmxs	Rmxs	Frmx	Rrmx
3-1	161	32	129	27	0.80	0.84	125	23	123	19	0.98	0.83
3-2	134	24	118	22	0.88	0.92	156	37	135	28	0.87	0.76
3-3	143	23	130	19	0.91	0.83	141	18	122	18	0.87	1.00

The SFMR wind speed observations correlate well ( $r = 0.89$ ) with the GPS dropwindsondes (Figure 36a), with a RMSE of  $2.48 \text{ m s}^{-1}$ . A slight positive bias exists with increasing wind speed to a value of  $4 \text{ m s}^{-1}$  (Figure 36b). The azimuthal distribution of SFMR and dropwindsonde wind speed differences (Figure 36b) has a weak signal of

positive bias in the front quadrants and negative bias in the rear quadrants as suggested by Uhlhorn and Black (2003). As found in the Sinlaku case, the spread in the azimuthal distribution is large.

During the three flights in STY Jangmi, the mean (standard deviation) Frmx was  $1.05 (\pm 0.33)$  and the mean (standard deviation) Rrmx was  $0.81 (\pm 0.17)$ . These Frmx values are larger than found in Atlantic hurricanes (Powell et al. 2009). If the first flight when the center was ill-defined is removed, the mean (standard deviation) Frmx is  $0.89 (\pm 0.13)$  and the mean (standard deviation) Rrmx is  $0.84 (\pm 0.11)$ , which are similar to the Atlantic values of Powell et al. (2009).

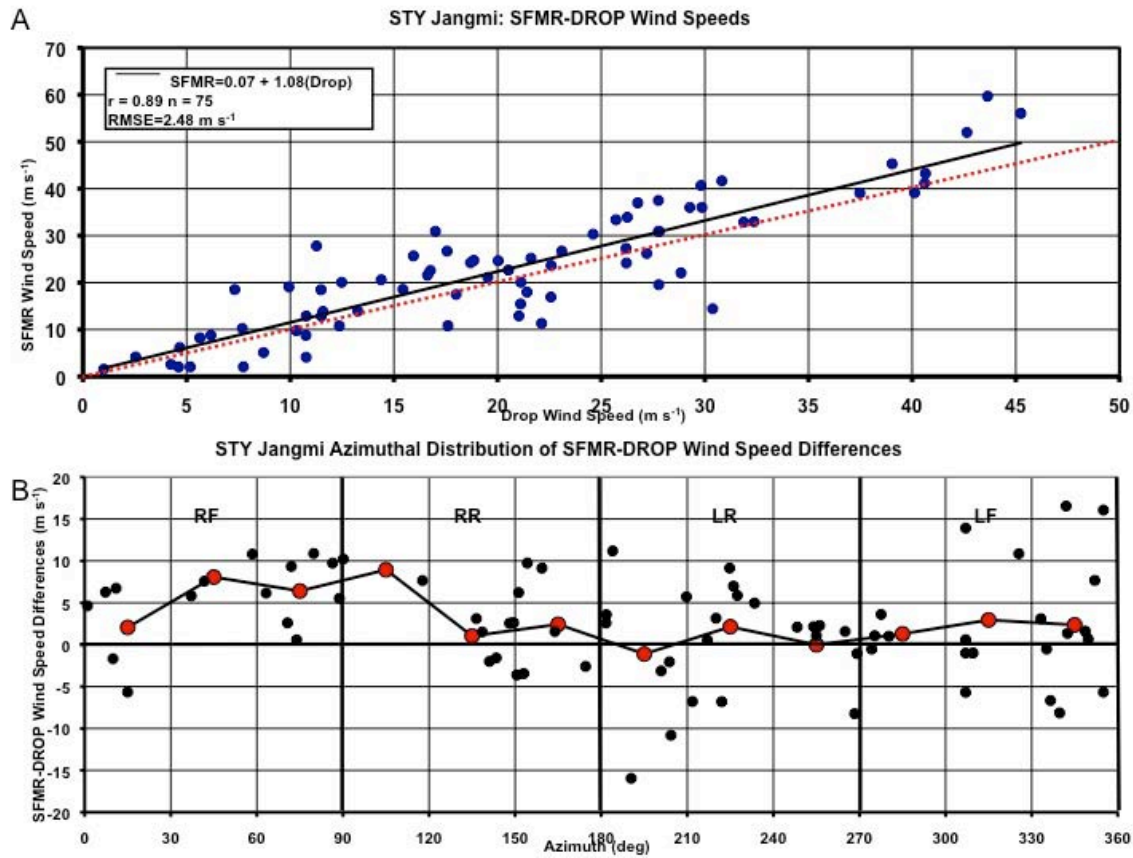


Figure 36. As in Figure 19, except for STY Jangmi SFMR-dropwindsonde wind speed comparisons. The SFMR-dropwindsonde best fit curve is  $(\text{SFMR} = 0.07 + 1.08(\text{Drop}), \text{RMSE} = 2.48 \text{ m s}^{-1})$ .



#### 4. Summary

This study has examined eight WC-130J flights in three TCs that contained 18 radial legs with a total of 221 GPS (0-150 m layer-averaged) dropwindsonde observations. During each leg, the SFMR surface winds and flight-level winds have been compared. The combined SFMR and dropwindsonde wind speed observations are highly correlated ( $r = 0.88$ ) with a RMSE of  $2.58 \text{ m s}^{-1}$  (Figure 37a). A slight positive bias of  $1.7 \text{ m s}^{-1}$  (Figure 37c) of the SFMR wind speed exists with a standard deviation of  $5.9 \text{ m s}^{-1}$  (Figure 37c). In the combined data set, the azimuthal distribution of wind speed differences exhibits a slight pattern of positive SFMR bias in the front quadrants and negative bias in the rear quadrants (Figure 37 b). While the variability in the data contributes to a weak signal in the distribution of the averages in each  $30^\circ$  azimuthal slice, large individual negative differences occur in the left-rear (LR) quadrant and large positive differences occur in the left-front (LF) quadrant as defined by Uhlhorn and Black (2003) and Powell et al. (2009). Furthermore, the average difference in each  $30^\circ$  azimuthal slice may be shifted in the positive direction due to the  $1.7 \text{ m s}^{-1}$  bias (Figure 37c).

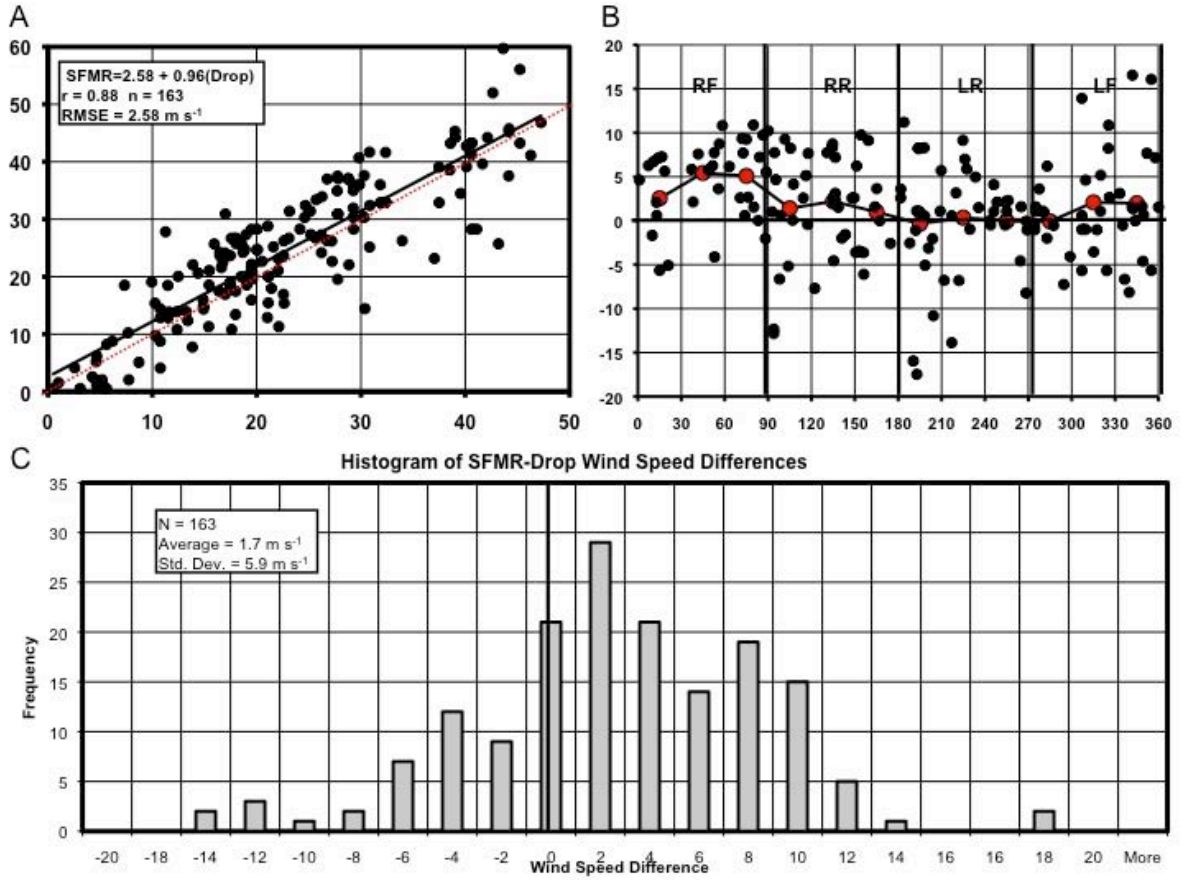


Figure 37. (a) SFMR-dropwindsonde comparison with the best fit ( $SFMR = 2.58 + 0.96(Drop)$ ,  $RMSE = 2.58 \text{ m s}^{-1}$ ) defined by the black line. (b) Azimuthal distribution of SFMR-dropwindsonde wind speed differences. (c) Bin-averaged histogram of SFMR-dropwindsonde wind speed differences (mean of  $1.7 \text{ m s}^{-1}$  and standard deviation of  $5.9 \text{ m s}^{-1}$ ).

The three storm systems had a combined mean (standard deviation)  $F_{rmx}$  of  $0.98 (\pm 0.25)$  (Figure 38a) and a combined mean (standard deviation)  $R_{rmx}$  of  $0.80 (\pm 0.14)$  (Figure 38b), which indicates that on average, the surface wind maxima were similar to, but were located radially inward of, the flight-level wind maximum. However, a number of the slant reduction factors greater than 1.0 were for the TS stage. The three storm systems had a combined median  $F_{rmx}$  of 0.89 and a combined median  $R_{rmx}$  of 0.81, which are closer to the mean values found in mature Atlantic hurricanes (Powell et al. 2009). Combined values of  $F_{rmx}$  were found to be negatively correlated with  $R_{mx}$  (Figure 38c). Therefore, instances of small radius of maximum winds were associated

with less slope between flight-level and surface wind maxima. Combined values of Frmx were found to be positively correlated with Rrmx (Figure 38d).

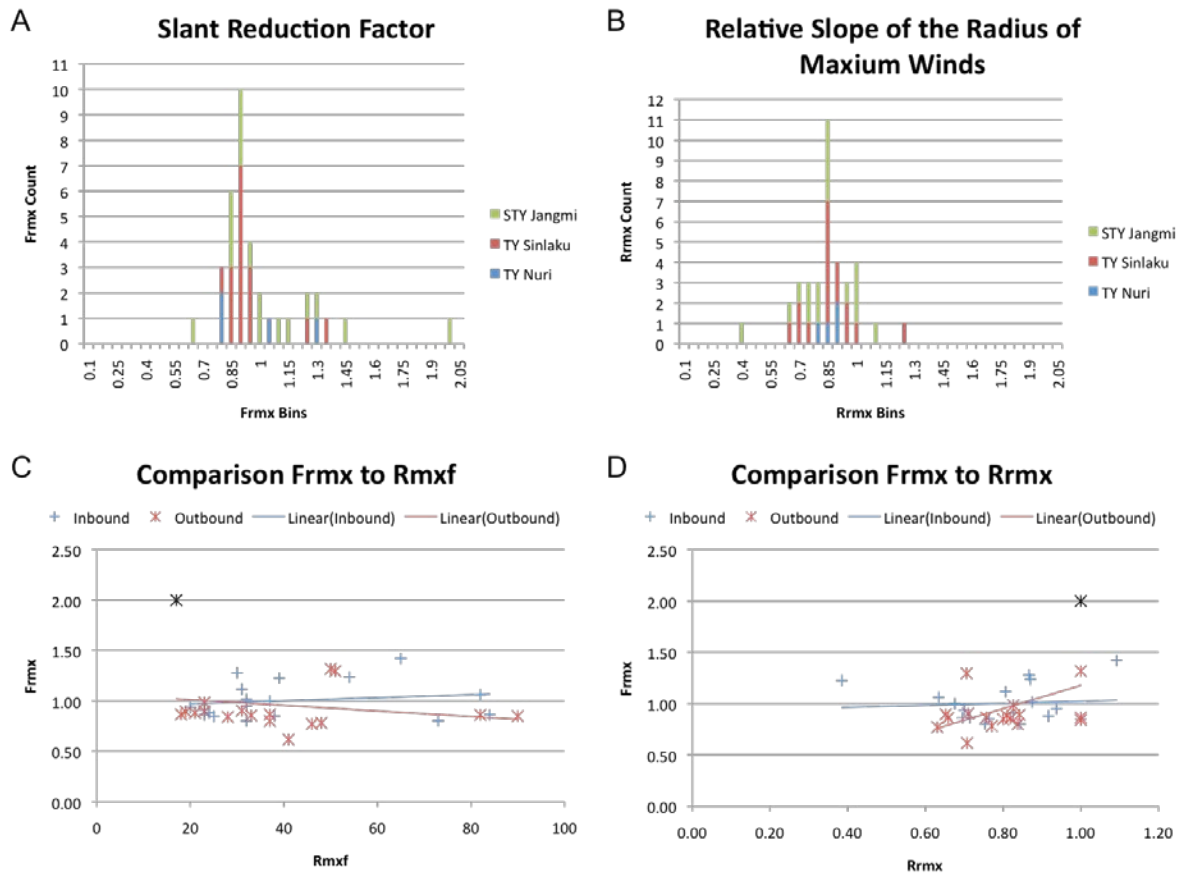


Figure 38. (a) Bin-averaged slant reduction factor (Frmx) by storm (STY Jangmi in green, TY Sinlaku in red, TY Nuri in blue). (b) As in (a), except for bin-averaged relative slope of the radius of maximum winds (Rrmx) by storm. (c) Comparison of Frmx to Rmx with least-squares fit lines (inbound track in blue, outbound track in red, black represents significant outlier from TS Jangmi leg 1-1). (d) As in (c) except for comparison of Frmx to Rrmx.

These distributions match well to the recent studies conducted in the Atlantic (Powell et al. 2009, Uhlhorn et al. 2007), who found the mean hurricane Frmx is 0.83 ( $\pm 0.09$ ) and Rrmx is 0.88 ( $\pm 0.16$ ). However, the three systems in this study varied in intensity from TS to STY, and most of the initial flight legs were flown into broad-disorganized systems (formation missions vice pure intensity missions). Removal of the first flight in TY Sinlaku and the first flight in STY Jangmi adjust the combined calculations of Frmx to 0.89 ( $\pm 0.12$ ) and Rrmx to 0.79 ( $\pm 0.11$ ). This adjusted slant

reduction factor is significantly closer to the median values from all flights and to that observed in the Atlantic hurricanes by Powell et al. (2009).

## B. SURFACE WIND FIELD

Ensuring the accuracy of surface wind field analyses of TCs is invaluable for forecasting the future development of tropical storm systems. Through an enhanced understanding of how the surface wind fields develop, strengthen, and mature, forecast model accuracy can be improved in conjunction with providing leadership with more complete risk management criteria. This study of WNP TC surface wind fields utilizes H\*Wind to analyze wind distribution data from eight observation platforms, including rare WNP aircraft in situ data.

In this section, the sensitivity of the H\*Wind analyses to various combinations of the eight observation systems, and to adjustments in the weighting factors for satellite data and ECMWF data are examined. Observation systems are combined in various subsets (Table 16) to identify the impacts of each system on WNP typhoon surface wind field distribution.

Table 16. Observation system combinations examined in this study.

<u>Name</u>	<u>Systems</u>
SAT	All available satellite systems
AC	All available aircraft systems
ACSAT	All available aircraft and satellite systems
SAT1	All available satellite systems weighted 1.00
ACSAT1	All available aircraft and satellite systems weighted 1.00
SATE1	All available satellite systems plus ECMWF (weighted 1.00)
ACSATE1	All available aircraft and satellite systems plus ECMWF (weighted 1.00)
ACE1	All available aircraft systems plus ECMWF (weighted 1.00)
ALL	All available systems
ALLE1	All available systems plus ECMWF (weighted 1.00)
ALLE2	All available systems plus ECMWF (weighted 0.25)
ALLE5	All available systems plus ECMWF (weighted 0.05)
ACE2	All available aircraft systems plus ECMWF (weighted 0.25)
SATE2	All available satellite systems plus ECMWF (weighted 0.25)
ACSATE2	All available aircraft and satellite systems plus ECMWF (weighted 0.25)

To examine the various analyses, the mean speed error (kt), mean direction error (deg.), RMS speed error (kt), and RMS direction error (deg.) are calculated from differences between H\*Wind analyzed values and all observations in each respective combination defined in Table 16. Finally, each analysis set is compared to the corresponding dropwindsondes to produce a RMSE value (i.e., "RMSE to drops") that is specific to the observation system(s) during the time-period. Therefore, the RMSE to dropwindsondes will be the assumed "ground-truth" and will provide a baseline for establishing observation system impact to WNP TC surface wind field distribution.

From the H\*Wind analysis sensitivity tests, three areas for further study developed. Each of the three separate findings are diagnosed below using distinct combinations of 12-hour data centered on Nuri flight four (0000 UTC 19 September), Sinlaku flight three (1200 UTC 11 September), Sinlaku flight four (1800 UTC 12 September), Jangmi flight two (0000 UTC 26 September), and Jangmi flight three (0600 UTC 27 September). A summary of findings concludes this section.

## **1. Data Distribution and Weighting**

Adjusting the weighting factors for observation types is one way to control the H\*Wind analyses. In H\*Wind, ASCAT (AS), QuickSCAT high-resolution (QH), and Windsat (WS) winds are nominally weighted at 0.25 but the gridded fields are only weighted at 0.05. To investigate the sensitivity of H\*Wind to each observation type, surface analyses were performed with varying weights for satellite observations and ECMWF fields. One concern with using polar-orbiting satellites for tropical observations is the satellite swath coverage specific to each storm center. Due to the large swath "blanks" near the equator, satellite coverage is often limited or partial near tropical systems. This bias has been examined by Brennan et al. (2009), who discuss the importance of good satellite coverage and resolution for NHC tropical forecasting.

To assess the impact of data coverage, Sinlaku flight three and flight four were chosen because Sinlaku flight three has better satellite coverage (Figure 39c) around the center of the storm than Sinlaku flight four (Figure 39d). For each case, a 12-hour observation window is used that is centered at 1200 UTC 11 September for Sinlaku flight

three and at 1800 UTC 12 September for Sinlaku flight four. Although satellite observations that were not flagged as rain contaminated exist in Sinlaku flight four (grey color in Figure 39d), they were not used in the H\*Wind analysis (Figure 39b) because they seemed to misrepresent the circulation relative to the location of the best track center.

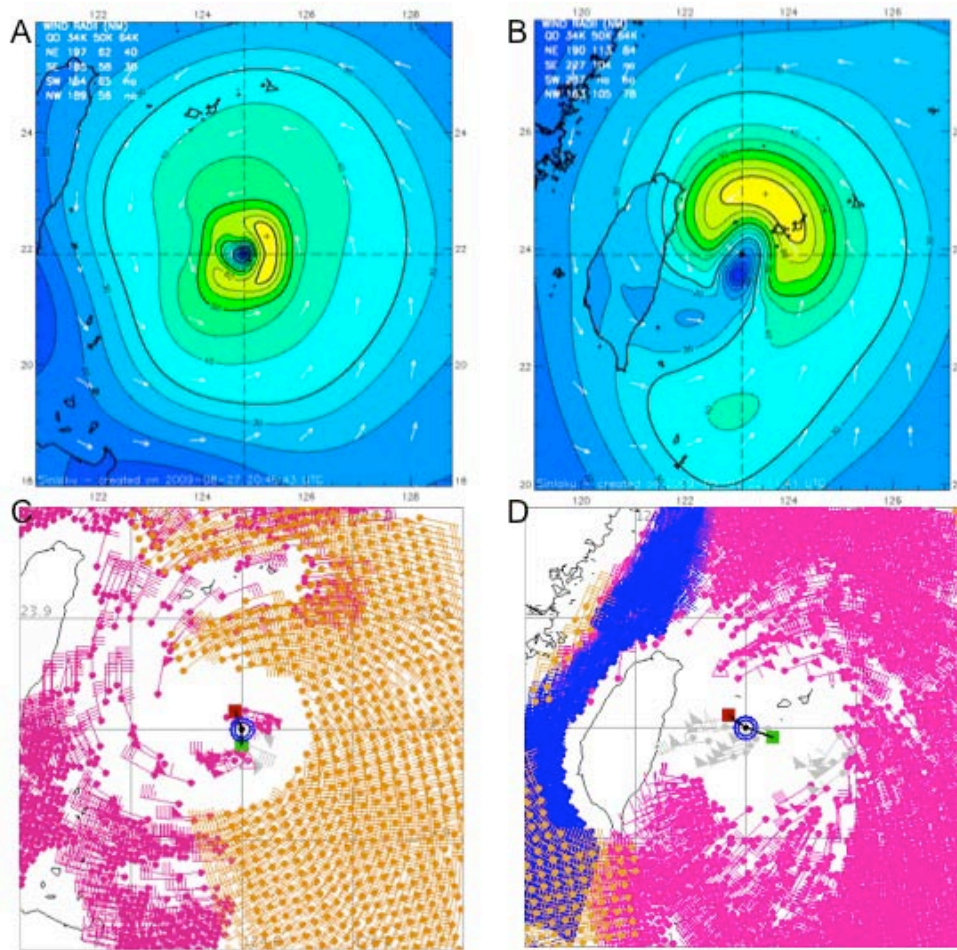


Figure 39. (a) H\*Wind 8 deg. lat. by 8 deg. lon. wind speed (kt) analysis of SAT (as defined in Table 16 for TY Sinlaku flight three. (b) As in (a) except for TY Sinlaku flight four. (c) H\*Wind observation distribution of SAT including QH (magenta), AS (tan), and WS (blue). (d) As in (c), except for flight four for comparison.

The first comparisons are to examine the impact of scatterometer data distribution relative to aircraft observations and gridded analysis fields from the ECMWF. Analyses constructed using only satellite observations weighted at 1.00 (SAT1) show only slightly

improved changes from satellite analyses weighted at 0.25 (SAT) (Figure 40a). By increasing the SAT weight from 0.25 to 1.00: During Sinlaku flight three the speed RMSE relative to all observations decreased by 0.24 kt, the speed RMSE relative to the dropwindsondes increased by 0.04 kt, and the direction RMSE decreased by 0.54 deg. (SAT in Figure 40a). During Sinlaku flight four the speed RMSE decreased by 0.74 kt, the speed RMSE (to dropwindsondes) increased by 0.19 kt, and the direction RMSE decreased by 1.38 deg. (SAT1 in Figure 40a). When only satellite data are input in H\*Wind, the RMSE values with respect to the dropwindsondes are relatively large and do not vary with increasing weight. This is expected since the scatterometer observations do not cover the center region of the TC where the aircraft observations are concentrated. This impact is noticeable as the large asymmetry in the analysis for flight four (Figure 39 b, d) where the satellite observation coverage relative to the center is better than in flight three (Figure 39 a, c).

When combined with aircraft observations (ACSAT and ACSAT1), the RMSE values for both flights using all observations increase dramatically as the aircraft observations have provided detailed information in the center portion of the TC where the scatterometer observations were not present. Several changes occur when the SAT weight is increased from 0.25 (ACSAT) to 1.00 (ACSAT1). During Sinlaku flight three, the speed RMSE relative to all observations decreased by 0.79 kt, the speed RMSE relative to the dropwindsondes decreased by 0.04 kt, and the direction RMSE decreased by 0.27 deg. (ACSAT in Figure 40a). During Sinlaku flight four, the speed RMSE decreased by 1.07 kt, the speed RMSE (to dropwindsondes) increased by 0.22 kt, and the direction RMSE decreased by 1.35 deg (ACSAT1 in Figure 40 a). Increasing the weight of satellite data does still reduce the RMSE to all observations. Combined aircraft and satellite observations result in a significant drop of the RMSE to the dropwindsondes. However, increasing the weight of satellite data from 0.25 (ACSAT in Figure 40a) to 1.0 (ACSAT1 in Figure 40a) does not significantly change the RMSE to the dropwindsondes. These sensitivity analyses demonstrate that highly-weighted satellite observations with good coverage around the center (flight three) have less statistical error than highly-weighted, but limited, satellite coverage (flight four).



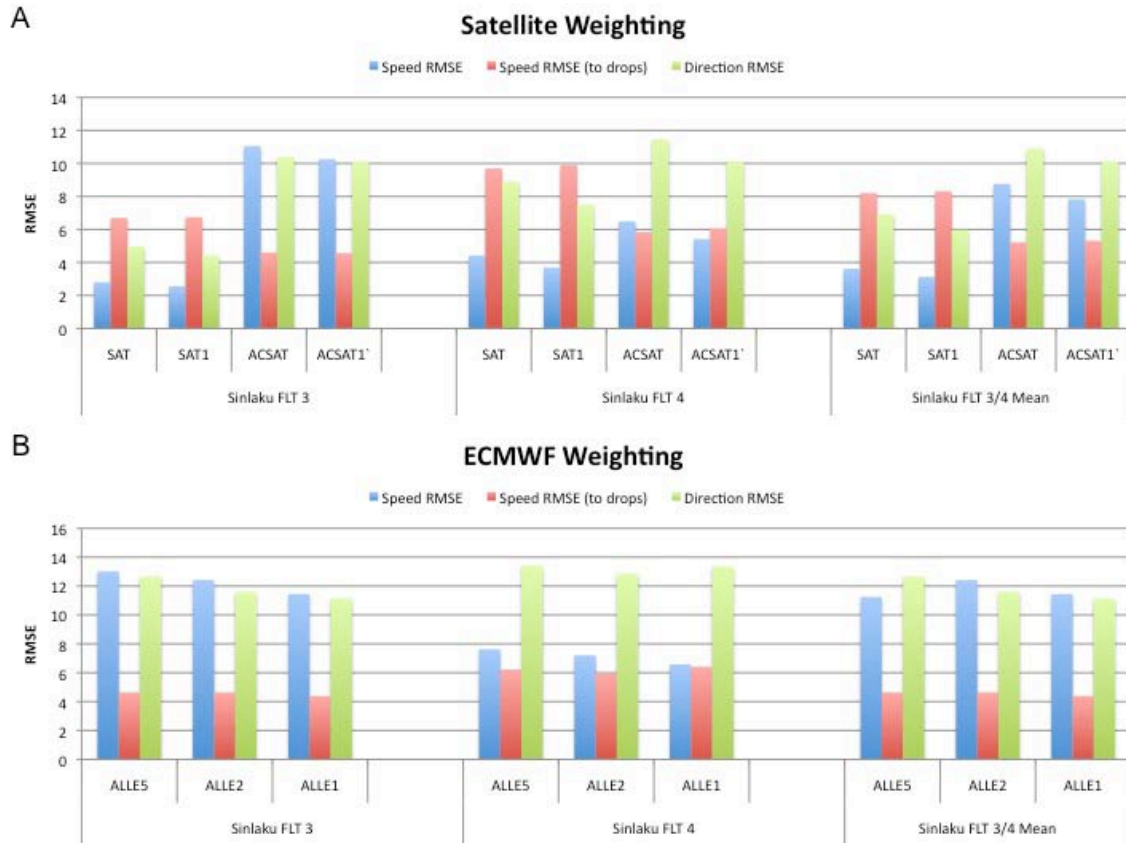


Figure 40. H\*Wind analyzed wind speed (kt) RMSE (blue), direction (deg.) RMSE (green), and wind speed (kt) RMSE to dropwindsondes (red). Observation system categories are located along the x-axis for Sinlaku flight 3, Sinlaku flight 4, and the average of both flights. (a) Satellite weighting chart for SAT, SAT1, ACSAT, and ACSAT1. (b) ECMWF weighting chart for ALLE5, ALLE2, and ALLE1.

Often, the distributions of satellite and aircraft observations are highly asymmetrical about the storm center. Incorporation of a gridded analysis field from a model is one way to provide uniform data distribution. To examine this impact, the ECMWF gridded analyses are input into H\*Wind along with the aircraft and satellite observations defined above. The ECMWF gridded analyses fields were translated so that the ECMWF TC center is superposed on the TC best-track position. Statistical characteristics of analyses performed with ECMWF data weighted at 0.05, 0.25, and 1.00 identify impacts relative to the weight value (Figure 40b). Several changes are noted when the ECMWF weight is increased from 0.05 (ALLE5) to 1.00 (ALLE1). During Sinlaku flight three, the speed RMSE relative to all observations decreased by 1.57 kt, the



speed RMSE relative to the dropwindsondes decreased by 0.25 kt, and the direction RMSE decreased by 1.53 deg. (ACSAT in Figure 40b). During Sinlaku flight four, the speed RMSE decreased by 1.04 kt, the speed RMSE (to dropwindsondes) increased by 0.19 kt, and the direction RMSE decreased by 0.06 deg. (ACSAT1 in Figure 40b). Relative to all observations input to H\*Wind, the increased weight of the ECMWF analyses generally leads to decreased RMSE speed errors for both flights. However, no impact is found in the RMSE to dropwindsondes, which probably occur near the storm center. The impact of the ECMWF analysis on the distribution of analyzed winds near the storm center is examined more fully in section 2. However, these examples demonstrate that incorporating a background field and increasing its weight tends to decrease statistical differences to all observations, but not to aircraft observations.

To examine the impact of adjusting the satellite coverage variability more fully, an example is provided here of TY Sinlaku flight three centered at 1200 UTC 11 September. The analysis discussed above examined the accuracy of the H\*Wind analyses compared to flight four as an H\*Wind analysis was performed with good central SAT coverage (Figure 41d). To examine the sensitivity of scatterometer data coverage, central observations were "flagged" (removed from the analysis) within H\*Wind (Figure 41e), and then a 150 n mi box of SAT observations were flagged (Figure 41f).

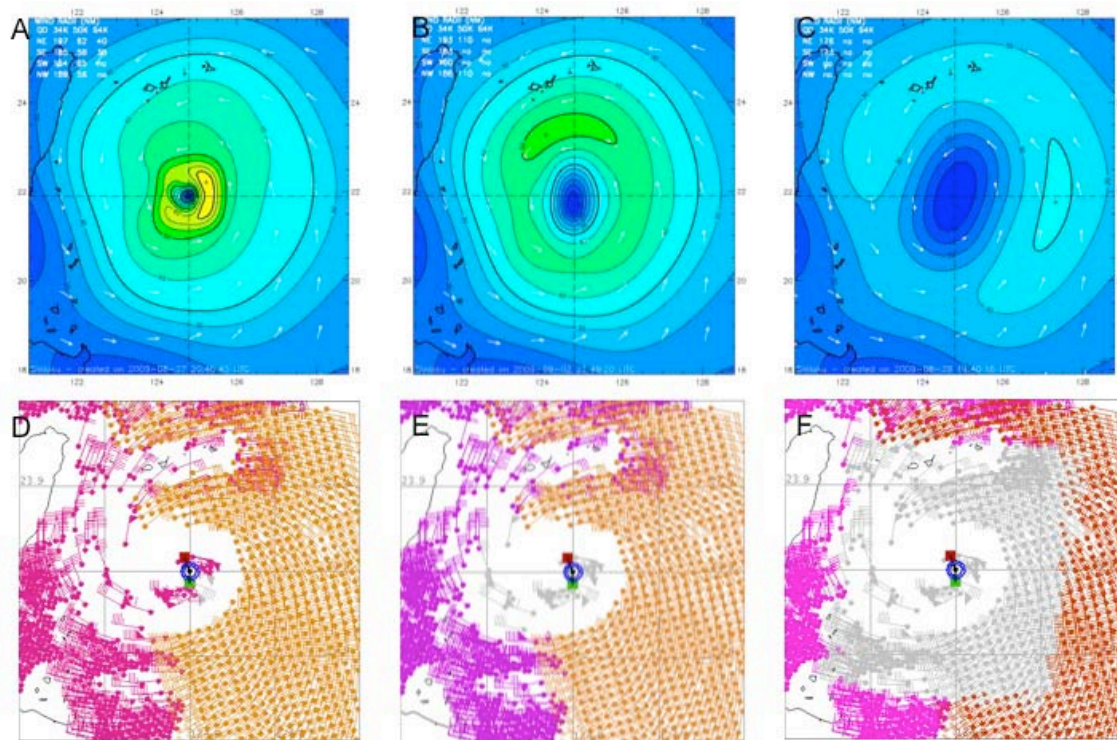


Figure 41. (a) H\*Wind 8 deg. lat. by 8 deg. lon. wind speed (kt) analysis graphical display of the SAT (as defined in Table 16). (b) As in (a) except with central observations removed. (c) As in (a) except with a 150 n mi box removed. (d) H\*Wind observation distribution of SAT including QH (magenta), AS (tan), and WS (blue). (e) As in (c) except with central observations flagged (all observation types) for comparison. (f) As in (c) except with a 150 n mi box flagged (all observation types) for comparison.

The analyzed maximum wind speed for the analysis with good central SAT coverage is 68 kt located 33 n mi NE from the center (Figure 41a). The analyzed maximum wind speed for the analysis with the central SAT coverage removed is 52 kt located 92 n mi NW from the center (Figure 41 b). The analyzed maximum wind speed for the analysis with the central SAT coverage box removed is 35 kt located 150 n mi SE from the center (Figure 41c). The difference field (Figure 42) demonstrates that the relatively few observations near the storm center have a significant impact on analyzed intensity and that good central satellite coverage is vital for wind field analyses of WNP TCs where aircraft observations are not operationally available.

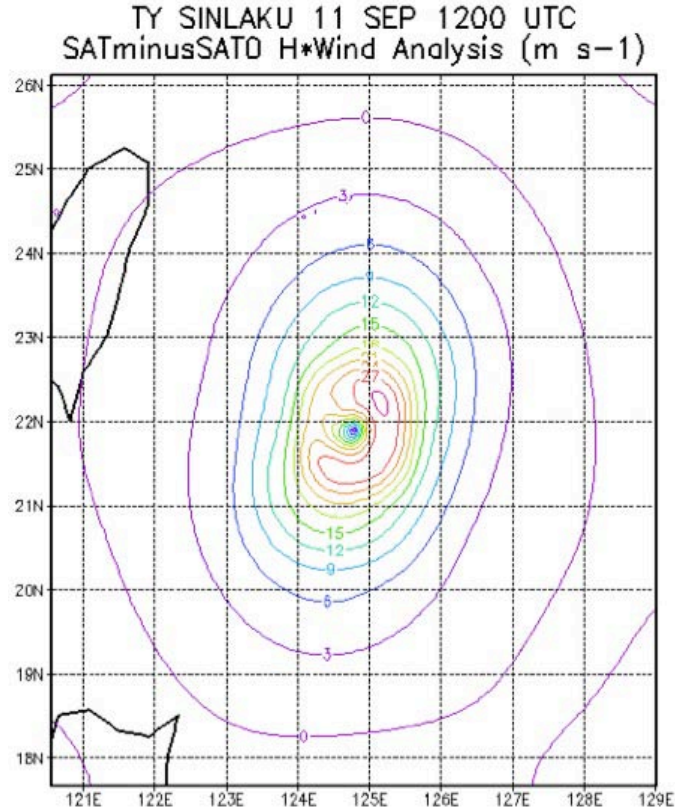


Figure 42. Wind speed ( $\text{m s}^{-1}$ ) difference field from subtracting the SAT analysis without the center box region (Figure 41 c) from the SAT analysis (Figure 41 a).

## 2. ECMWF and Aircraft

Aircraft observations add essential in situ data to TC analyses. When available, they provide good temporal and spatial coverage over the central core region of the TC. As shown in the previous section, ingestion of aircraft observations with satellite data into H\*Wind provides valuable TC surface wind field detail. The incorporation of only a 12-hour ECMWF analysis at 1200 UTC 11 September into H\*Wind defines a maximum wind speed of 60 kt located 44 n mi NW from the center (Figure 43a). The H\*Wind analysis of just an aircraft (AC) data set (same center parameters) provides a maximum wind speed of 111 kt located 46 n mi NE from the center (Figure 43b).

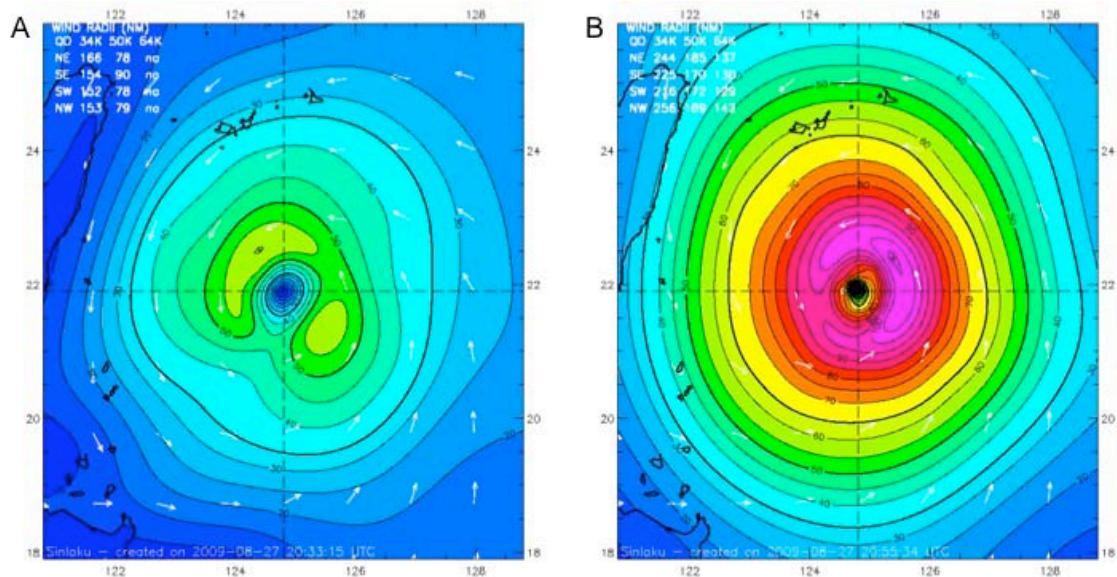
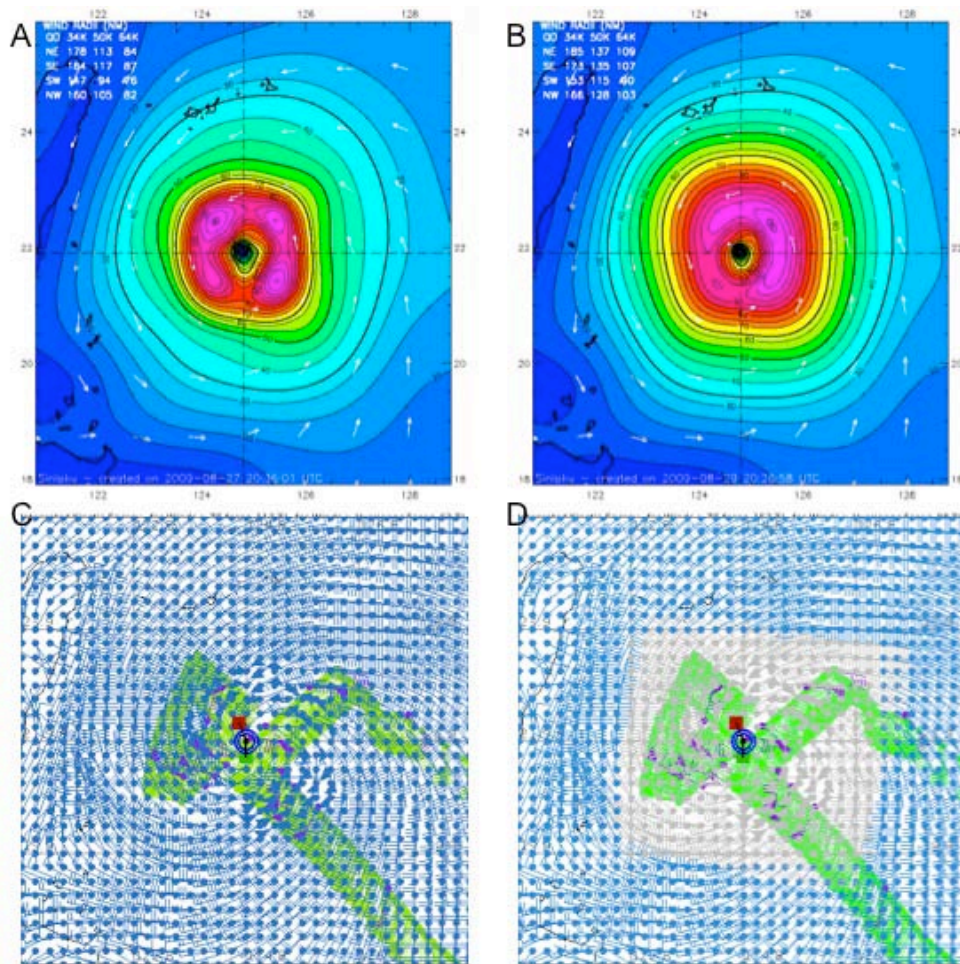


Figure 43. (a) H\*Wind 8 deg. lat. by 8 deg. lon. wind speed (kt) analysis display of ECMWF data. (b) As in (a), except AC (as defined in Table 16).

When the two data sets are combined (AC plus EC1), an interesting multi-lobe feature develops around the center in the H\*Wind analysis (Figure 44 a). This multi-lobe feature appears to be a byproduct of the H\*Wind analysis that combines the linear “alpha” pattern with significantly larger wind speeds (111 kt max) from the aircraft observations with the gridded and smaller ECMWF wind speeds (60 kt max) (Powell personal communication). To illustrate this further, a box of ECMWF winds immediately surrounding the aircraft data was removed (flagged within H\*Wind) for the same analysis as above (Figure 44 c, d). The analysis of the aircraft data and ECMWF data, with the specified ECMWF data flagged, does not have the multi-lobe anomaly (Figure 44 b). By subtracting the “flagged” analysis (Figure 44b) from the “un-flagged” analysis (Figure 44 a), a difference field is created (Figure 45) that identifies the multi-lobe characteristic. This difference field shows the unique structural differences between the H\*Wind analyses, and therefore the importance of understanding how H\*Wind handles different data sets.





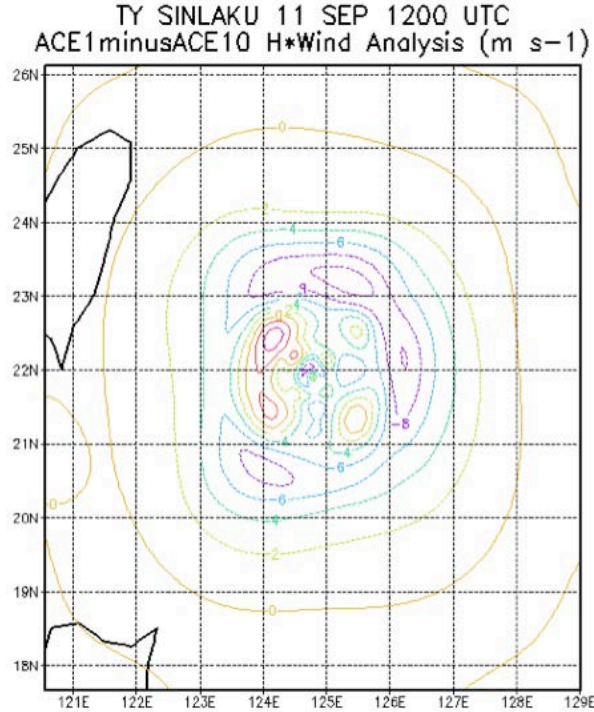


Figure 45. Wind speed ( $\text{m s}^{-1}$ ) difference field from subtracting the ACE1 analyses without the center region (Figure 44 b) from the ACE1 analysis (Figure 44 a).

### 3. Aircraft and Satellite

Aircraft and satellite observations contribute value to the TC analysis in unique ways. Satellite observations contribute repetitive, large-coverage data sets that are invaluable for remotely monitoring tropical activity. However, the previous sections have highlighted the importance of areal coverage relative to the center. Aircraft observations are critical for ensuring the accuracy of TC intensity estimates. In this study, five separate flight events were analyzed to study the relative impacts of aircraft and satellite observation data sets on the H\*Wind analyses. In each case, an H\*Wind analysis was conducted with aircraft observations alone (AC), satellite observations alone (SAT), and the combination of aircraft and satellite observations (ACSAT).

Several important characteristics are evident in the comparisons. The mean (standard deviation) wind speed RMSE to all observations for AC is  $12.15 (\pm 8.39)$  kt, SAT is  $3.43 (\pm 1.00)$  kt, and ACSAT is  $8.26 (\pm 3.17)$  kt (Figure 46 a). The mean wind direction RMSE for AC is  $19.72 (\pm 10.02)$  deg., SAT is  $8.83 (\pm 3.14)$  deg., and ACSAT

is 13.57 ( $\pm$  4.77) deg. (Figure 46b). When these H\*Wind analyses are compared to all data, the dominance of satellite data is clear as they have the smallest RMSE values (SAT in Figure 46 a, b). The RMSE of the aircraft analyses are largest (AC in Figure 46 a, b) due to the relatively high density and somewhat variable SFMR winds. Combined aircraft and satellite data (ACSAT) produce intermediate RMSE values.

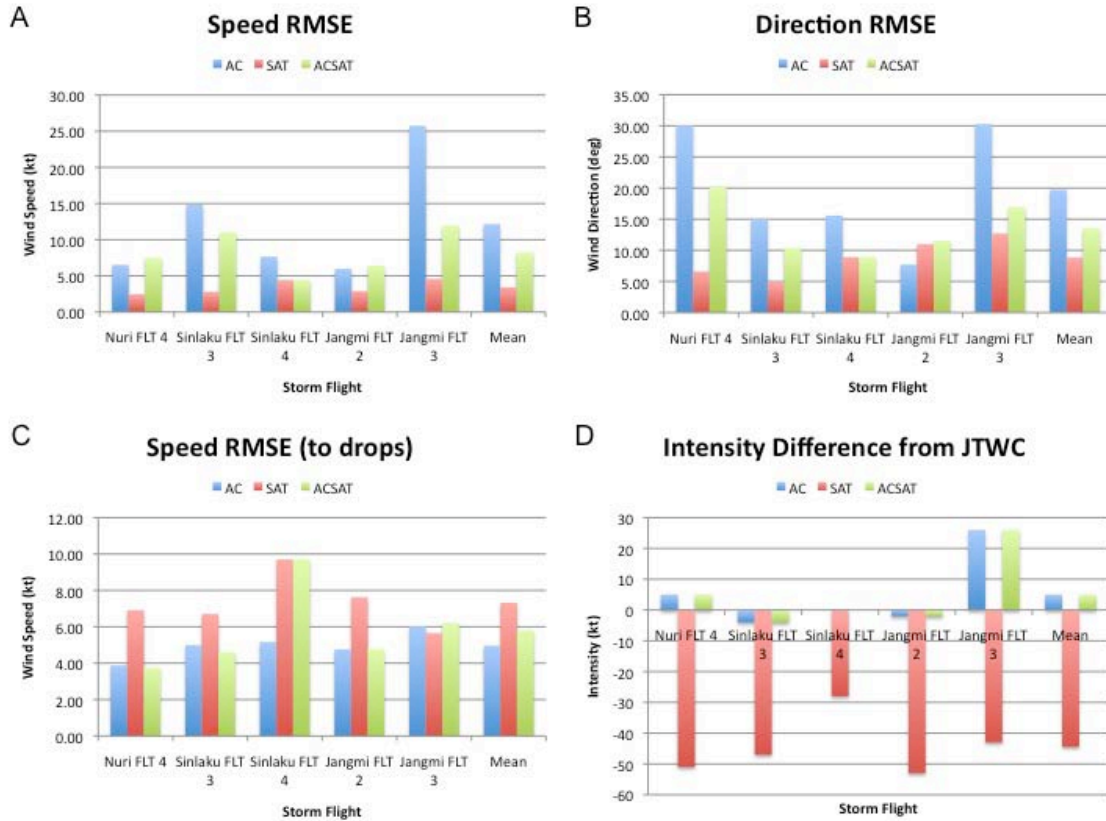


Figure 46. Aircraft and satellite comparison charts for the H\*Wind analyses in the AC RMSE (blue), SAT RMSE (red), and ACSAT RMSE (green). Observation system categories are located along the x-axis for Sinlaku flight 3, Sinlaku flight 4, Jangmi flight 2, Jangmi flight 3, and the average of all four flights. (a) Wind speed (kt) RMSE, (b) Wind direction (deg.) RMSE, (c) Wind speed (kt) RMSE to dropwindsondes, and (d) Intensity difference from JTWC best track.

In this study, comparisons of H\*Wind analysis values to dropwindsondes is assumed as a baseline for accuracy (Figure 46 c). The mean wind speed RMSE to dropwindsondes for AC is 4.96 ( $\pm$  0.77) kt, SAT is 7.32 ( $\pm$  1.51) kt, and ACSAT is 5.81 ( $\pm$  2.35) kt (Figure 46c). As expected, RMSE values for satellite-only analyses are large

when compared to the dropwindsonde observations. For several flights (i.e. Nuri flight four, Sinlaku flight three, and Jangmi flight two), the combined aircraft and satellite observations produced the lowest (3.75 kt, 4.60 kt, and 4.77 kt) RMSE values to the dropwindsondes. However, for flights into storms when the distribution of satellite coverage was poor relative to the center (i.e., Sinlaku flight four), the combined aircraft and satellite RMSE values were large (9.70 kt) and dominated by the influence of the satellite data. The H\*Wind analyses of only aircraft data (AC) has larger values of RMSE than only scatterometer observations (SAT) when compared to all observations. However, aircraft data has significantly less RMSE than SAT when directly compared to the dropwindsondes (Figure 46 a, b, c).

In addition, the mean intensity difference from the JTWC best-track for AC is 5.00 ( $\pm$  12.21) kt, SAT is -44.40 ( $\pm$  9.94) kt, and ACSAT is 5.00 ( $\pm$  12.21) kt (Figure 46d). Aircraft observations are significantly closer to the operational TC intensity estimates than satellite observations (Figure 46d). The H\*Wind analyses constructed using only satellite scatterometer data significantly underestimated the operational JTWC TC intensity. For the three Jangmi analyses, the operational TC intensity is much less than the aircraft maximum winds (Figure 46 d), which may be related to the large RMSE values associated with the aircraft observations (Figure 46a).



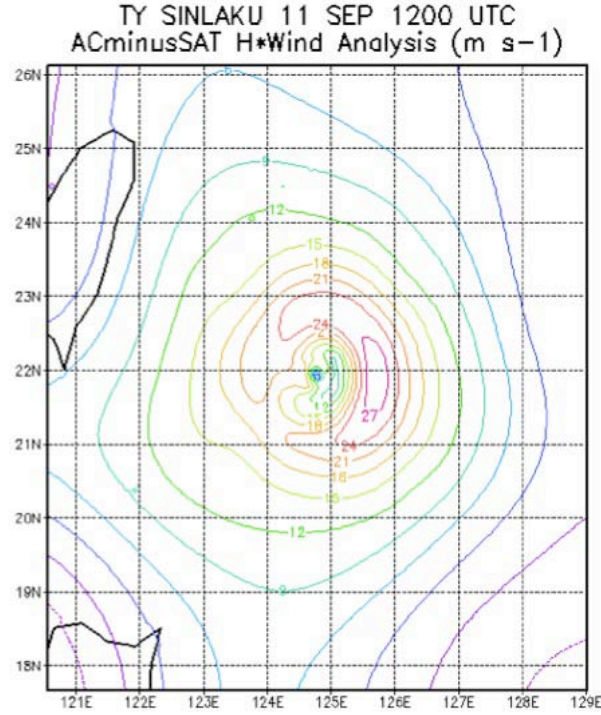


Figure 47. Wind speed ( $\text{m s}^{-1}$ ) difference field from subtracting the SAT analysis (Figure 46 a) from the AC analysis (Figure 46 b).

#### 4. Summary

Understanding how different observation types are incorporated into H\*Wind is essential for understanding the analyses of surface wind fields. Weighting, data coverage, and data types all change how accurate the H\*Wind analyses are relative to in situ observations. In this study, GPS dropwindsondes are assumed to be the “ground-truth.” Each analysis is compared to the GPS dropwindsondes to understand the associated accuracies of analyses based on each observation system. Furthermore, a byproduct of the H\*Wind analyses are the statistical error correlations between the analysis and all observation points, and these statistical error results are used to understand how the observation systems compare overall. The following two charts summarize the important aspects diagnosed above.

In the mean (Figure 48 a, b), the AC analysis has the highest speed RMSE ( $12.15 \pm 8.39$  kt) and direction RMSE ( $19.72 \pm 10.02$  deg.), which is expected due to the high density and variability in SFMR winds. The EC analyses had the lowest speed RMSE

( $2.55 \pm 0.89$  kt) and direction RMSE ( $5.63 \pm 1.50$  deg.) (Figure 48 a, b), which is expected due to the complete coverage of gridded values of winds in the ECMWF analyses. However, the EC analyses leads to the highest intensity differences ( $-48.40 \pm 23.45$  kt) from the JTWC best-track (Figure 49b). In the mean, the SAT analyses had the highest speed RMSE (to drops) ( $7.32 \pm 1.51$  kt) (Figure 49a) and the AC analyses had the lowest speed RMSE (to drops) ( $4.96 \pm 0.77$  kt) (Figure 49a). However, the AC and ALLE2 analyses had the lowest intensity differences ( $5.00 \pm 12.21$  kt) from the JTWC best-track (Figure 49b). In this study, aircraft observations were invaluable for estimating WNP TC intensity.

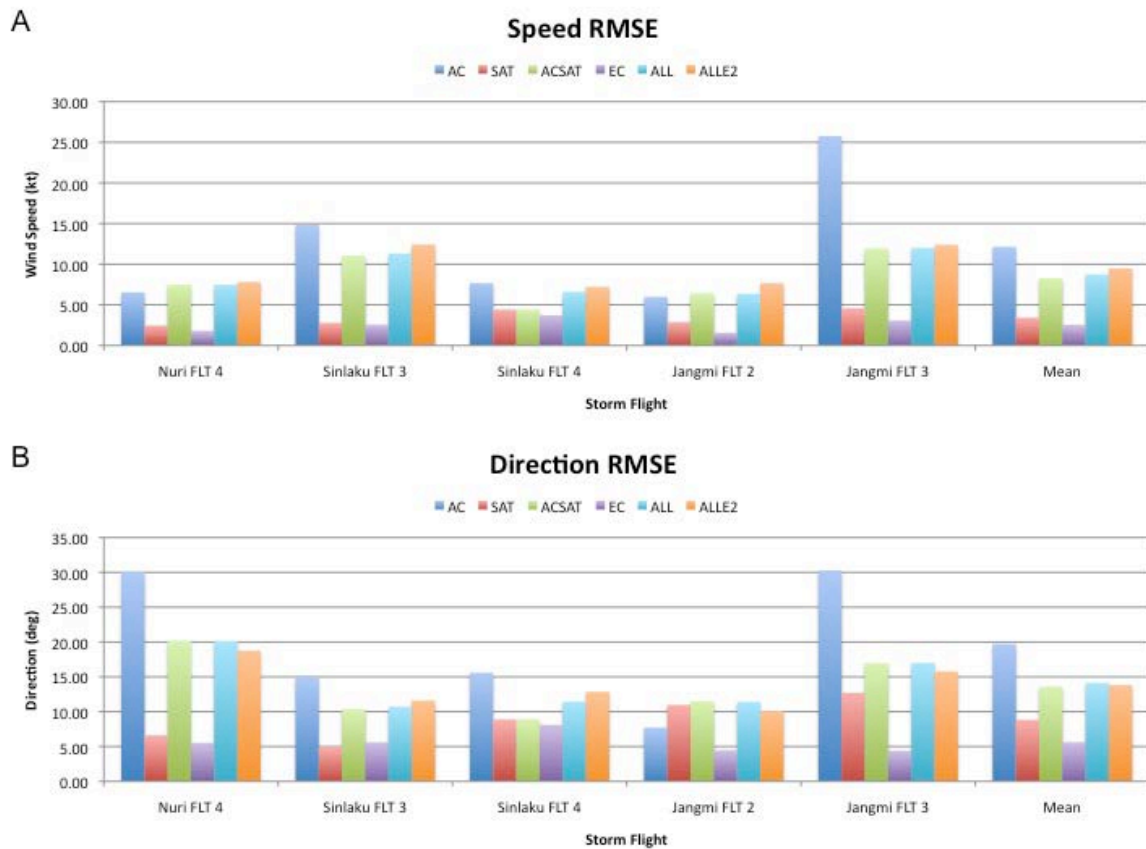
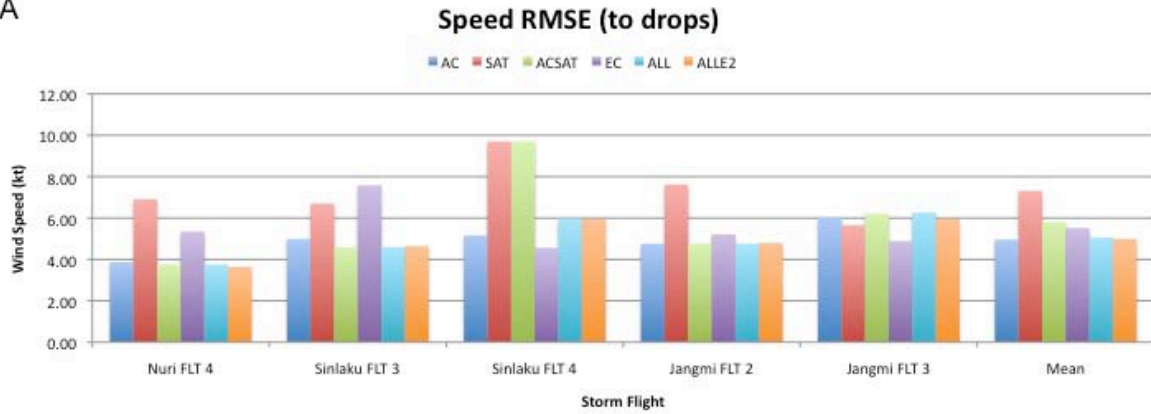


Figure 48. Summary comparisons of H\*Wind analyses of the AC RMSE (blue), SAT RMSE (red), ACSAT RMSE (green), EC RMSE (purple), ALL RMSE (cyan), and ALLE2 RMSE (orange). Observation system categories (defined in Table 16) are displayed along the x-axis for Sinlaku flight 3, Sinlaku flight 4, Jangmi flight 3, Jangmi flight 2, Jangmi flight 3, and the average of all four flights. (a) Wind speed (kt) RMSE relative to all of the observations. (b) Wind direction (deg.) RMSE relative to all of the observations.

A



B

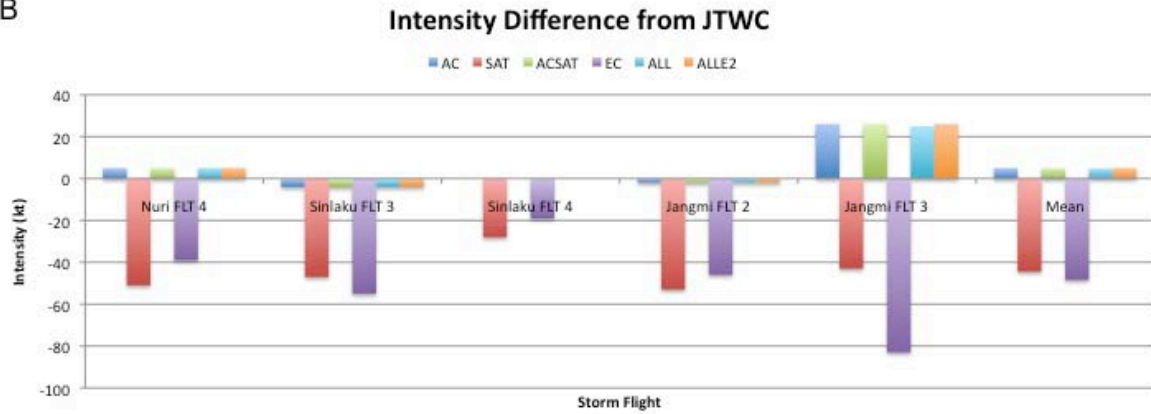


Figure 49. As in Figure 48, except for (a) Wind speed (kt) RMSE relative to the dropwindsondes and (b) Intensity differences from the JTWC best track.

## **IV. CONCLUSIONS**

### **A. SUMMARY**

Tropical cyclones are immense weather phenomena that impact the global environment, and therefore are of intense scientific interest to operators, forecasters, modelers, and researchers. Military operations occur worldwide, often in remote and harsh environments. Operators and planners require high-tech, reliable, and timely meteorology and oceanography forecasts to ensure mission success. Increasing understanding and the ability to forecast TC formation, intensification, and structure change will enhance tropical risk management (mitigate disastrous consequences) across the globe.

The focus of this study is to assess the impact of surface wind analyses of aircraft observations co-located with remotely sensed observations in the WNP during the T-PARC/TCS08 field experiments (late July through early October 2008). The HRD H\*Wind surface wind analysis system is used with the aircraft observations collected during T-PARC/TCS08, JTWC best-track, storm, and satellite data. This is the first time in almost two decades that such a densely co-located observation data set (including satellite, aircraft, and driftsondes) was available for the WNP.

During the middle of the 2008 typhoon season, T-PARC/TCS08 scientists monitored and tracked multiple circulations labeled as TCSs that later became TCs. Three storms selected for this study are Nuri, Sinlaku, and Jangmi. Eight observation systems were selected for this study: ASCAT, ASOS, GPS dropwindsondes, METAR, ship observation, SFMR, QuickSCAT, and WindSat. The HRD H\*Wind surface wind analysis system was utilized to systematically analyze the observation sets. The H\*Wind analyses with and without the inclusion of the ECMWF gridded analysis with different weighting values demonstrate the influence of a gridded analysis as compared to various observation sets. Comparisons with the U.S. Air Force 53<sup>rd</sup> Weather Reconnaissance Squadron WC-130J GPS dropwindsondes and SFMR surface winds are used as the

“ground-truth” for assessing the accuracy of surface wind estimates. Finally, ratios of the maximum flight-level and surface winds are calculated to identify the slant reduction factor and eyewall slope characteristics.

Eight WC-130J flights from three TCs that contained 18 radial legs are examined. During each leg, SFMR surface winds and flight-level winds are available, and a total of 221 GPS (0-150 m layer-averaged) dropwindsonde observations were obtained. This overall sample of SFMR and dropwindsonde wind speed observations are highly correlated ( $r = 0.88$ ) with a RMSE of  $2.58 \text{ m s}^{-1}$ , and a slight positive bias of the SFMR wind speed exists at all wind speeds. The azimuthal distribution of wind speed differences exhibits a slight pattern of positive SFMR bias in the front quadrants and negative bias in the rear quadrants. While the summation of the variability within  $30^\circ$  azimuthal slices contributes to a weak signal in the azimuthal distribution, it is clear that the individual large negative differences occur in the left-rear (LR) quadrant and large positive differences occur in the left-front (LF) quadrant as was found in a large sample of Atlantic hurricanes by Uhlhorn and Black (2003) and Powell et al. (2009). Furthermore, the average difference in each  $30^\circ$  azimuthal slice may be shifted in the positive direction due to the  $1.7 \text{ m s}^{-1}$  bias.

The three storm systems had a combined mean slant reduction factor ( $F_{rmx}$ ) of  $0.98 (\pm 0.25)$  and a combined mean relative slope of maximum winds ( $R_{rmx}$ ) of  $0.80 (\pm 0.14)$  which indicates the majority of the surface wind maxima were slightly smaller, but located radially inward of, the flight-level wind maximum. The three storm systems had a combined median  $F_{rmx}$  of 0.89 and a combined median  $R_{rmx}$  of 0.81, which are closer to the mean values found in mature Atlantic hurricanes (Powell et al. 2009). These distributions match well to the recent studies conducted in the Atlantic (Powell et al. 2009, Uhlhorn et al. 2007). Removal of the first flight into TY Sinlaku and the first flight into STY Jangmi adjust the combined calculations of  $F_{rmx}$  to  $0.89 (\pm 0.12)$  and  $R_{rmx}$  to  $0.79 (\pm 0.11)$ . The adjusted slant reduction factor is significantly closer to that observed in the Atlantic hurricanes by Powell et al. (2009). Combined values of  $F_{rmx}$  were found to be negatively correlated with  $R_{mx}$  - - therefore instances of small radius of maximum

winds were associated with less slope between flight-level and surface wind maxima. Combined values of Frmx were found to be positively correlated with Rrmx.

This study of WNP TC surface wind fields utilize H\*Wind to analyze wind distribution data from eight observation platforms, including rare WNP aircraft in situ data. By comparing and contrasting the eight observation systems, and by adjusting the weighting factors for satellite data and ECMWF data, this study has demonstrated the sensitivity of the H\*Wind analyses to each data set. Observation systems are also combined together in various subsets to show the impacts of each system archetype on WNP TC surface wind field distribution. While a multitude of analysis options is available in H\*Wind, only the standard settings have been used to isolate the impact of specific data sources.

In the mean, satellite observations produced the largest speed RMSE relative to the dropwindsonde 150-m average ( $7.32 \pm 1.51$  kt) and aircraft observations had the smallest speed RMSE (to dropwindsondes) ( $4.96 \pm 0.77$  kt). In the mean, ECMWF analyses had the highest intensity differences ( $-48.40 \pm 23.45$  kt) from the JTWC best-track intensities. Analyses that included the WC130-J SFMR and GPS dropwindsondes had the smallest intensity differences ( $5.00 \pm 12.21$  kt) relative to the JTWC best-track intensity.

Forecasters rely heavily on numerical analyses (global and regional) that combine rare in situ observations (ship, buoys, rawindsondes, aircraft) with remotely sensed observations (weather satellites and radar). Due to the relatively data-sparse in situ observation coverage over the remote oceanic regions, weather satellites remain the most effective tropical observation tool for this area. In this study, aircraft observations from T-PARC/TCS08 were invaluable for estimating WNP TC intensity. Increasing the amount of in situ aircraft observations in the WNP will enhance tropical cyclone understanding and ensure accurate, timely forecasts are delivered to customers for mission success and safety.

## **B. RECOMMENDATIONS**

Tropical cyclone research is an intense ongoing science that has acquired even greater importance in this era of global climate change. Increased study of TC formation and intensification using aircraft data in the WNP is recommended to further enhance the forecast ability of both numerical models and human forecasters. It is shown in this study that aircraft data significantly improve the surface wind analysis and structure characterization. The H\*Wind analysis tool can be used to analyze multiple observation data sets and systematically produce analysis products. The H\*Wind tool would provide even more research value with increased automation, documentation, and archive capability. Whereas only three storm systems were examined in this study, analyses of the remaining T-PARC/TCS08 systems (especially the non-developing cases) are recommended to provide further valuable insight into TC development and intensification.



## LIST OF REFERENCES

- Brennan, M. J., C. C. Hennon, and R. D. Knabb, 2009: The operational use of QuickSCAT ocean surface vector winds at the National Hurricane Center. *Wea. Forecasting*, **24**, 621–645.
- European Centre for Medium-Range Weather Forecasts, cited 2009: ECMWF Web site. Retrieved 1 Aug 2009. [Available online at <http://www.ecmwf.int/>]
- Elsberry, R. L., and P. A. Harr, 2008: Tropical Cyclone Structure (TCS08) field experiment: Science basis, observational platforms, and strategy. *Asian Pacific Journal Atmospheric Science*, **44**, 209–231.
- European Space Agency, cited 2009: ESA ASCAT Web site. Retrieved 1 Aug 2009. [Available online at <http://www.esa.int/esaME/ascats.html>]
- Franklin, J. L., M. L. Black, and K. Valde, 2003: GPS dropwindsonde wind profiles in hurricanes and their operational implications. *Wea. Forecasting*, **18**, 32–44.
- Gray, W. M., 1979: Hurricanes: Their formation, structure and likely role in the tropical circulation. *Meteorology over the Tropical Oceans*, 155–218.
- Hock, T. F., and J. L. Franklin, 1999: The NCAR GPS dropwindsonde. *Bull. Amer. Meteor. Soc.*, **80**, 407–420.
- HRD, 2009a: NOAA HRD Surface Wind Analysis Web site. Retrieved 1 Aug 2009. [Available online at [http://www.aoml.noaa.gov/hrd/data\\_sub/wind.html](http://www.aoml.noaa.gov/hrd/data_sub/wind.html)]
- \_\_\_\_\_, 2009b: NOAA HRD SFMR Web site. Retrieved 1 Aug 2009. [Available online at <http://www.aoml.noaa.gov/hrd/project2005/sfmr.html>]
- Joint Typhoon Warning Center, cited 2009a: 2008 Annual Tropical Cyclone Report. Retrieved 1 Sep 2009. [Available online at [http://metocph.nmci.navy.mil/jtwc/atcr/atcr\\_archive.html](http://metocph.nmci.navy.mil/jtwc/atcr/atcr_archive.html)]
- \_\_\_\_\_, 2009b: Collaboration Site Retrieved 1 Sep 2009. [Available online at (password protected) <https://pzal.nmci.navy.mil/cgi-bin/collab.cgi>]
- Kepert, J. D., 2001: The dynamics of boundary layer jets within the tropical cyclone core. Part I: Linear theory. *J. Atmos. Sci.*, **58**, 2469–2484.

- Navy Research Laboratory, cited 2009a: NRL WindSat Web site. Retrieved 1 Aug 2009. [Available online at <http://www.nrl.navy.mil/WindSat/index.php>]
- \_\_\_\_\_, 2009b: NRL Monterey Tropical Cyclone Homepage Retrieved 1 Aug 2009. [Available online at [http://www.nrlmry.navy.mil/tc-bin/tc\\_home2.cgi](http://www.nrlmry.navy.mil/tc-bin/tc_home2.cgi)]
- National Weather Service, cited 2009: NWS Automated Observing System. Retrieved 1 Aug 2009. [Available online at <http://www.nws.noaa.gov/asos/>]
- Powell, M. D., S. H. Houston, L. R. Amat, and N. Morisseau-Leroy, 1998: The HRD real-time hurricane wind analysis system. *J. Wind Engineer. and Indust. Aerodyn.*, **77 and 78**, 53–64.
- \_\_\_\_\_, E. W. Uhlhorn, and J. D. Kepert, 2009: Estimating maximum surface winds from hurricane reconnaissance measurements. *Wea. Forecasting*, **24**, 868–883.
- Uhlhorn, E. W., P. G. Black, J. Carswell, J. L. Franklin, A. S. Goldstein, and M. Goodberlet, 2007: Hurricane surface wind measurements from an operational Stepped Frequency Microwave Radiometer. *Mon. Wea. Rev.*, **135**, 3070–3085.
- \_\_\_\_\_, and P. G. Black, 2003: Verification of remotely sensed sea surface winds in hurricanes. *J. Atmos. Oceanic Technol.*, **20**, 99–116.

## INITIAL DISTRIBUTION LIST

1. Defense Technical Information Center  
Ft. Belvoir, Virginia
2. Dudley Knox Library  
Naval Postgraduate School  
Monterey, California
3. Mr. Jeff Hawkins  
Naval Research Laboratory  
Monterey, California
4. Dr. Pete Black  
Naval Research Laboratory  
Monterey, California
5. Professor Patrick Harr  
Naval Postgraduate School  
Monterey, California
6. Professor Russell Elsberry  
Naval Postgraduate School  
Monterey, California
7. Professor Michael Montgomery  
Naval Postgraduate School  
Monterey, California
8. Director, Joint Typhoon Warning Center  
Pearl Harbor, Hawaii
9. Director, Hurricane Research Division  
Miami, Florida